Semi-Solid Forging of Steels: New insights into material behaviour evolution and industrialisation

GORKA PLATA REDONDO

Mondragon Goi Eskola Politeknikoa

Mechanical and Manufacturing department

October 4, 2018

A dissertation submitted
in fulfilment of the requirements for the degree of
Doctor by Mondragon Unibertsitatea

Semi-Solid Forging of Steels: New insights into material behaviour evolution and industrialisation

GORKA PLATA REDONDO

Supervised by Zigor Azpilgain and Jokin Lozares

Mechanical and Manufacturing Department
Mondragon Goi Eskola Politeknikoa
Mondragon Unibertsitatea

Statement of originality

I hereby declare that the research recorded in this thesis and the thesis itself were developed entirely by myself at the Mechanical and Manufacturing Department at the University of Mondragon. Some results come from the 4 months stay at the University of Warwick funded by the Basque Government.

Abstract

European trends of reduction of emissions and the zero environmental impact together with the globalisation are showing a huge impact on the actual steel-making and automotive steel components manufacturers. This is therefore driving the European market to higher strength-to-weight materials and more efficient fabrication processes to maintain the competitiveness. For this reason, the Semi-Solid Forging (SSF) of steels could be a real possibility for the industry to stay at the forefront of the market.

This technology has produced automotive steel components reducing the required raw material and energy consumption while attaining as forged mechanical properties. At the present time, the production limit of components via SSF can be as low as 50 components. The understanding of the manner the material evolves during the process (and the reason for the observed soft flow during forging) are still limited.

Considering the high potential of the process, this PhD has focused on trying to give an explanation to the material behaviour. At the same time, a considerable number of components have been manufactured to show the repeatability and durability of the utilised materials and equipment. The results of this investigation aim to bring the SSF closer to the industrial reality.

In terms of the material behaviour analysis, different hypotheses have been proposed and analysed. Both sulphur content and incipient melting has been characterised and no significant impact of these parameters has been seen on the semi-solid forgability of 42CrMo4. However, it has been suggested that other alloys may be more prone to incipient melting compared to the 42CrMo4. Adiabatic heating has shown that a significant temperature can be caused as a result of the high local strains/strain rates. It has not been distinguished whether this can cause liquid formation. However, local softening of the material is, indeed, likely. Further trials for adiabatic heating are needed in order to fully assess its role on the SSF process.

With regard to the component manufacturing, apart from medium carbon steels, Alloy 28 (a high Nickel steel) has also been trialled using this method. In this latter case, which is infamous for its poor forgability, the incipient melting may have enhanced the fluidity of the material enabling an even softer filling. In addition to that, a batch of 250 components has been successfully manufactured attaining the already confirmed cost saving and great mechanical properties apart from the desired repeatability of the process and the minor die degradation.

Resumen

Tanto la globalización como la tendencia europea de reducir a cero el impacto medioambiental, así como la reducción de las emisiones, ha generado un gran impacto tanto en las acerías como en los fabricantes de componentes para automoción. De manera que, para seguir siendo competitivos, la creación de materiales de mayor resistencia en relación con su peso y procesos de fabricación más eficientes parece vital. En este escenario, la Forja de aceros en estado Semi-Sólido (SSF) puede reivindicarse como una posibilidad real para mantener este tipo de industria al frente del mercado.

Esta tecnología ha sido capaz de producir componentes de automoción de acero ahorrando material y energía a la vez que se obtenían propiedades mecánicas similares a los componentes forjados. A pesar de ello, a día de hoy, la producción de estos componentes vía SSF no supera las 50 piezas. Además, la evolución del material durante el proceso y la causa de la facilidad observada del material para fluir es aún una incógnita.

Teniendo en cuenta el potencial del proceso, esta tesis se ha enfocado en intentar dar una explicación al comportamiento del material a la vez que se han fabricado un número considerable de componentes para demostrar la repetitividad y durabilidad de los materiales y equipamientos utilizados. Los resultados de la tesis, por tanto, están orientados a acercar el proceso de SSF a la industria.

En cuanto al análisis de comportamiento del material, se han propuesto y analizado diferentes hipótesis. Ni el azufre ni el fenómeno "incipient melting" parecen ser los responsables del ablandamiento observado durante la fabricación de componentes con el 42CrMo4. En cualquier caso, el "incipient melting" sí que parece mejorar la fluidez del material en algunas aleaciones y a ciertas condiciones. En cuanto a la hipótesis del calentamiento adiabático, a pesar de ver un incremento de temperatura significativo debido a altas y localizadas deformaciones y velocidades, no se sabe si se ha generado líquido. Por lo tanto, se necesitan más experimentos para para aceptar o descartar definitivamente su influencia.

En lo que a la fabricación de componentes se refiere, además de aceros de medio carbono, se ha podido deformar el acero inoxidable "Alloy 28" vía SSF. En este último caso, que es de hecho un acero bastante difícil de forjar, el "incipient melting" parece haber incrementado la fluidez del material durante el llenado. Además, se ha fabricado un lote de 250 componentes obteniendo un ahorro en el coste de producción y buenas propiedades mecánicas a parte de la repetitividad deseada del proceso, así como una mínima degradación de las huellas.

Laburpena

Globalizazioak zein emisioen murrizketa eta ingurumenarekiko erantzukizuna zerora murrizteko europar mugimenduak eragin handia izan du, bai altzairutegietan, baita automobilgintzarako konponenteak fabrikatzen dituzten industrietan ere. Hau honela izanik, lehiakortasuna ez galtzearren, erresistentzia handiagoko eta pisu gutxiagoko materialak sortu behar dira, eraldaketa-prozesuen hobekuntza edota prozesu berrien ikerkuntzarekin batera. Egoera honetan, altzairuen Forja Erdi-Solidoa (SSF) aukera erreal bat izan daiteke aipatutako industriak merkatuaren lehen lerroan mantentzeko.

Teknologia honen bidez, dagoeneko, automobilgintzarako piezak fabrikatu dira, materiala eta energia aurrezten eta, aldi berean, forja konbentzionaleko propietate mekanikoak mantenduz. Dena den, gaur egun, prozesu honen bidez produzitutako konponenteak 50 baino gutxiago dira. Honetaz gain, prozesuan zeharreko materialaren eboluzioa eta materialean antzemandako jario erraztasuna ezezagunak dira oraindik.

Prozesuaren potentziala kontuan izanik, ondorengo tesia materialaren portaerari azalpen bat ematera bideratu da, eta prozesuaren errepikakortasuna zein material eta ekipamenduen iraunkortasuna frogatzera zuzenduta dago, azken honetarako pieza kopuru adierazgarri baten produkzioa egingo delarik. Hortaz, tesiaren emaitzak SSF prozesua industria mundura gerturatzeko zuzenduta daude.

Materialaren portaerari dagokionez, hipotesi ezberdinak proposatu eta aztertu dira. Ez sufre elementuak ez "incipient melting" fenomenoak ez dirudite 42CrMo4 materialean antzemandako biguntzearen arduradunak. Dena den, "incipient melting"-a materiala deformatzeko gaitasuna hobetu dezakeela dirudi aleazioaren arabera. Beroketa adiabatikoaren hipotesiari dagokionez, nahiz eta materiala berotzeko gai den deformazio eta abiadura altu eta lokalizatuetan, lortutako emaitza ez da nahikoa likidoaren sorrera konfirmatzeko. Bere eragina guztiz baztertu edo egiaztatzeko saiakuntza gehiagoren beharra dago.

Konponenteen fabrikazioari dagokionez, karbono kantitate ertaineko altzairuez gain, "Alloy 28" bezalako altzairu herdoilgaitza deformatzeko gaitasuna egiaztatu egin da. Forjatzeko altzairu zaila den azken kasu honetan, "incipient melting" fenomenoak materialaren jariakortasuna hobetu egin du moldeak betetzeko garaian. Honetaz gain, 250 pieza sorta fabrikatu dira produkzio kostearen murrizketa eta propietate mekaniko onak lortuz. Emaitza hauek garrantzitsuak diren arren, antzemandako prozesuaren errepikakortasuna eta moldearen gutxieneko degradazioa azpimarratu beharra dago.

Agradecimientos

Siempre hay algo que agradecer de la misma manera que siempre hay alguien al que agradecer algo. Desde el camarero o camarera que te pone un café para arrancar el día como la persona que te da un beso para acabarlo. Siempre hay que dar gracias. Y más aún cuando llegas a este punto en el que, si bien es cierto que llegas gracias a mucho esfuerzo, has quemado etapas en las que mucha gente ha sido directa o indirectamente partícipe. Por lo tanto, pido perdón de antemano si en esta locura de últimos días se me ha olvidado mencionar a alguien.

Me remontaría a tiempos de antaño, cuando empecé en esto de la ingeniería, pero tampoco quiero aburriros más de lo que ya haré si seguís leyendo. Simplemente, permitidme dedicarle este momento a mi tío Imanol, él ya sabe por qué.

Sin saber muy bien cómo, me he convertido no solo en ese "puto ingeniero" que, a ti Aita, tantos buenos momentos te han dado. Vaya suerte la tuya, que te ha salido un hijo "puto ingeniero" y encima listillo. Pero tranquilo, he aprendido tu lección. La experiencia siempre tiene que ser escuchada, que no toda la sabiduría reside en los libros.

Nunca podré agradecer todo lo que me ayuda, aporta, instruye y me tranquiliza la mujer más fuerte y luchadora que jamás conoceré. Gracias Ama, por encima de los tuppers y botes de comida que, seguramente, han sido la razón principal de que hoy esté aquí, te doy las gracias por escucharme sin tener ni idea del tema y siempre saber qué decir y cómo tranquilizarme. Decirte que eres la mejor se queda corto, pero eso tú ya lo sabes.

La familia es lo primero dicen, y más si sois como yo de familiares. Bien es cierto que no paro quieto, pero sois mi oasis y bálsamo para cualquier herida. Una sonrisa vuestra, y más de los peques, vale más que todo el dinero del mundo. No puedo nombraros a todos porque me quedo sin páginas, pero gracias hermanos/as, cuñados/as y sobrinos/as. Esto, como no, es extensible para ti Primo. Pocas personas hay que me conozcan y me entiendan mejor que tú.

Durante este trayecto ha habido muchas idas y venidas, tanto personales como profesionales. Una de ellas, quizás la más dulce, eres tú Christel. Gracias por tu paciencia, por sacarme de quicio, por hacerme reír, por tu cariño, por tu apoyo incondicional y, como no, por acompañarme durante mi estancia en Inglaterra. Fue increíble. Y lo seguirá siendo.

Oreka mantentzea bizitzan zehar da guztion erronka. Guztiok ditugu horri aurre egiteko erreminta edo teknikak. Nire kasuan, Orekariak ditut. Nire superheroiak dira. Kafetxo bakar batekin nahikoa daukate nire irribarrea ateratzeko. Maite zaituztet.

Probablemente pocas personas sepan tan bien como ellos todo lo que he pasado. Lo mismo que ellos. Han sido mi confesionario diario y el apoyo más cercano. Gracias a mis compañeros de piso Ion y Javi, al igual que al "perro" de Richi. Habéis hecho (y aún hacéis) que este trayecto haya sido y sea increíble. No me olvidaré mencionar a Jone que, a pesar de estar poco tiempo, me has demostrado un cariño que siempre tendré presente.

Entre doctorandos nos entendemos, y eso se nota. Vuestro apoyo ha sido esencial, tanto dentro como fuera de la Uni. Quiero dar las gracias en primer lugar a Iker, Maialen digo… Maider, Estela, Leire, Mano, Txino, Badiola y Buru. Cada café, birra (botella de agua en mi caso), comida o cena han sido, de largo, lo mejor que me llevo de aquí. Pero es que, además, habéis sido siempre los primeros en echarme una mano. Mil gracias. No me olvido de aquellos con los que quizás menos tiempo o no tan asiduamente he tenido el placer de estar, Iván, Raquel, Chamorro, Arakama, Julen, Endika, Elena… gracias, porque hasta la más mínima conversación de pasillo cuenta.

Siendo honesto, nunca me había planteado hacer un doctorado. Quería lo típico, encontrar un trabajo cerca de casa y poco más. Pero desde que en el proyecto fin de grado, no sé si por azar o queriendo, me toco introducirme en el mundo del semi-sólido y la investigación, me pico el gusanillo. En este sentido, tengo que dar las gracias a Zigor Azpilgain por brindarme la oportunidad de hacer este doctorado.

El transcurso ha sido largo, pero emocionante. Y ahí el equipo es lo más importante. Gracias a Rafa, que, aunque estuviste poco tiempo, me encantó trabajar contigo y que te picase a ti también el gusanillo por el semi-sólido. Como no dar las gracias al "puto amo", al mago de la maquinaria. Milesker Garate zure laguntasunagatik, bai unibertsitatearen barruan, baita kanpoan ere.

Quiero aprovechar este momento para agradecer al que siempre he dicho que es y seguirá siendo mi oráculo científico, Iñaki Hurtado, mejor conocido como Professor. Me encanta esa sensación de ir con un problema y salir con mil posibles soluciones. De la misma manera que vas con una solución y sales con mil problemas. En cualquier caso, mil gracias, si no fuera por tu ayuda, nunca hubiera sacado tanto a relucir mi alma de físico.

I want also to sincerely thank Professor Claire Davis for giving me the chance to stay 4 months working in the University of Warwick. I need to thank the generous help of Morteza and Mo. However, I feel lucky that I met a friend, a colleague, someone that unconsciously made my stay in Warwick to be awesome. Thanks Carl for sharing your expertise with me, for those beers (cider for me) and for those golf lessons. You will always have a house here in the Basque Country.

Se que me estoy extendiendo, pero pocos leeréis esto. Además, me falta la persona más importante. Él ha sido, sigue y seguirá siendo mi compañero de batallas. Mi amigo. Mi valedor. Diría que hasta se ha convertido, en cierta manera, en mi hermano mayor. Gracias Jokin por absolutamente todo. Por cada café en el Urrin pensando locuras. Por cada "business trip" en hoteles de 10 estrellas. Por cada consejo. Por estar ahí siempre que lo he necesitado. Por cada "Egun on Bizkaia" para poner en marcha la maquinaría cada mañana. Por cada fin de semana comiendo comida china entre componente y componente. Hay mil cosas más que querría agradecerte, pero no hace falta que las mencione. Y solo se me ocurre una manera de compensártelo: hagamos del NSF una realidad.

Nomenclature

BCC: Body Centred Cubic

BDC: Bottom Dead Centre

CDF: Closed Die Forging

DSC: Differential Scanning Calorimetry

EDS: Electron Diffraction Scattering

FCC: Face Centred Cubic

HF: Hot Forging

HT-CLSM: High-Temperature Confocal Laser Scanning Microscope

MGEP: Mondragon University

PF: Precision Forging

SEM: Scanning Electron Microscope

SF: Stacking Fault

SFE: Stacking Fault Energy

SSF: Semi-Solid Forging

SSP: Semi-Solid Metal Processing

TDC: Top Dead Centre

Contents

Chapter 1

INTRODUCTION

"Many leaders of big organisations, I think, don't believe that change is possible. But if you look at history, things do change, and if your business is static, you're likely to have issues"

Larry Page

Summary

Today's globalisation is threating the competitiveness of the classical manufacturing processes of the European companies. This together with the low emission and zero environmental liability trend asks for a technological step forward in those processes or even in the development of new ones. Since 2002, the semi-solid manufacturing process using aluminium, steel and hybrid structures has been investigated in Mondragon University (MGEP). The last results that have taken advantage of this process to attain sound steel components enhanced its research interest. As a consequence, this PhD has been launched. Therefore, a brief motivation and the scope this thesis will cover is presented in this section.

1.1. Introduction

Nowadays, the worldwide trend of promoting the reduction of emissions and the goal of being zero environmental liability threats the traditional habits of many sectors. Regarding those sectors, many of them made their move in order to fulfil the new tendency. As an example, most brands inside the automotive industry are actually selling hybrid or completely electric cars.

This philosophy direction indeed seems a turnaround in how everything is being done. In the case of the steel market, the emissions must be reduced in the whole processing chain of the product. This means that not only the steel producers have to modify or optimise their way of steel making, but also the ones that will use this steel for different purposes will have to think about how to agree with this trend (transport, construction…).

Taking the automotive industry again as an example, in order to reduce the emissions, the light-weighting is the main focus. Consequently, the use of materials with higher-strength-to-weight ratio are increasing on car components. According to the analysis made by the Deutsche Industriebank in 2015 [1], the amount of aluminium utilised in light cars will greatly increase to the detriment of steel (Figure 1.1). This requires a reaction from the steel sector to overcome this possible scenario since around 900kg of steel are currently being used per vehicle [2].

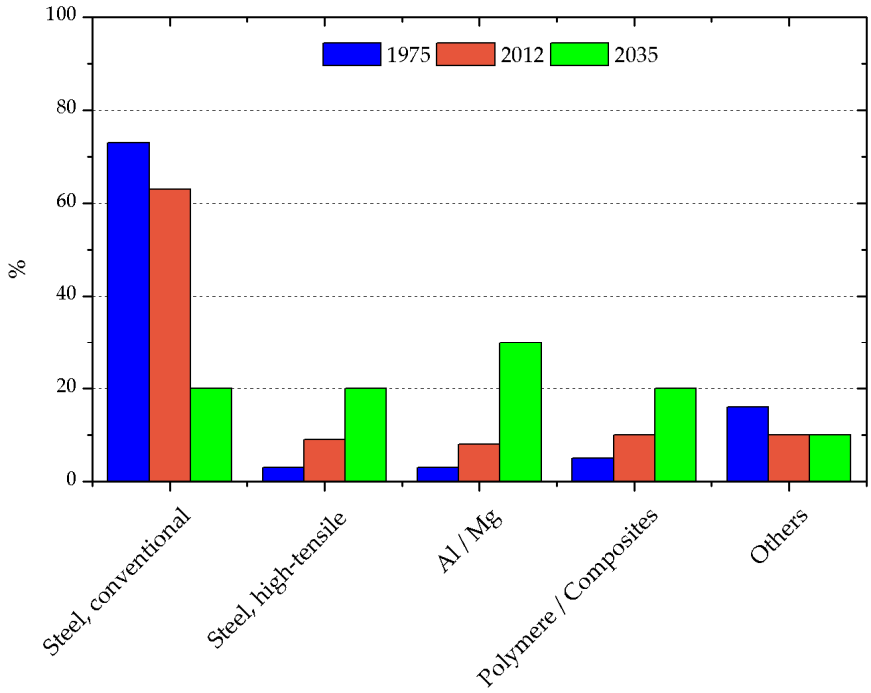

Figure 1.1 – Material split trend in light vehicles in % [1].

In the steel factories, new alloy designs are being developed to make them lighter or to improve their mechanical properties so as to need less material to fulfil the same requirements. However, this action must go hand in hand with the processes used to manufacture the components. In this aspect, the forging and casting industries, which are in turn the most used metal manufacturing processes in the automotive industry, must also be developed.

Last analysis about the foundry industry made by Dr. Heinz-Jürgen Büchner in 2018 [3] states how the process must be modified to reduce the specific weight of a cast part even if the automotive industry seem to grow. In the same fashion, the Forging Industry Association (FIA) strongly remarks the need of being more customer-focused, cost-effective, energy efficient and environmentally acceptable to remain competitive [4]. They define the reduction of the material waste and energy usage as well as the improvement of the forging technology as action priorities.

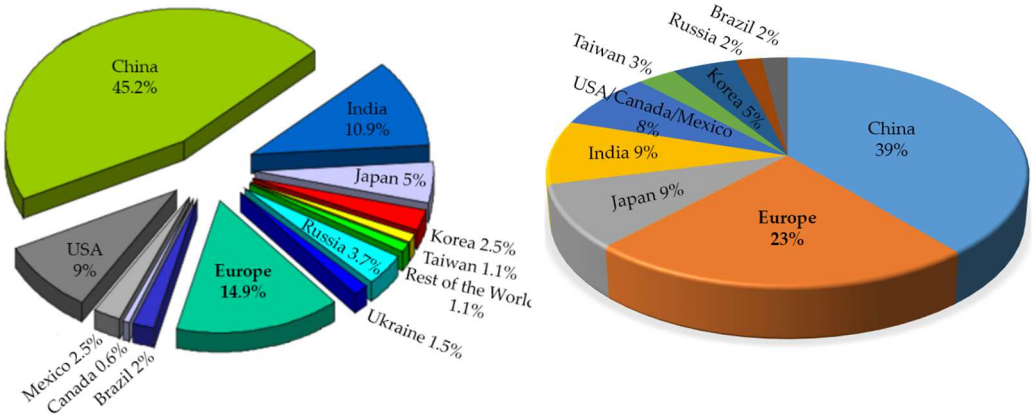

(a) **(b)**

Figure 1.2 – Schematic illustration of the total production of (a) castings and (b) forgings in 2016 divided by regions [5,6].

Europe is, behind China, the region that produces most castings and forgings in the world (Figure 1.2). According to the data of 2016, the 14.9% of the castings and the 23% of the forgings in the world were produced in Europe [5,6]. This means that any issue that generates a negative impact on those markets could imply a huge influence on the economy. Therefore, considering that Europe's labour costs are not competitive in comparison with other emerging economies, the efforts should be focused on getting stronger on those technologies or even developing new ones.

Moreover, moving forward on optimising the existing technologies or introducing new ones will of course impact on more markets than in automotive.

Oil and gas, aeronautic, shipping, agriculture and defence, among others, could also profit from any improvement performed in this area. This is a great reason for many European universities and research centres to investigate how to make such advance.

1.2. Motivation

Since 2002, researchers from Mondragon University (MGEP) have been investigating the Semi-Solid forming process (SSP). It is actually a process between forging and casting that uses a material in a condition where the solid and liquid coexist. As a consequence, the flowing capabilities are similar to a fully melted material while the mechanical properties of the final product are enhanced.

At that time, the main research focus was on light alloys. Due to their low melting point, those materials were easy to handle. The initial research topics were the development of different aluminium alloys to maximise their success when submitting to the SSP process and the components fabrication via this technology [7–9]. From then on, further research on different aluminium alloys were conducted [10,11].

However, the interest of using this technology with aluminium alloys decreased at the same time that it grew on hybrid components and high melting point alloys. Proof of that are the subsequent investigations and PhD works on hybrid [12] and steel [13] semi-solid forming.

The latter, indeed, was concluded with very interesting outcomes. It proved how, at certain conditions, steel automotive components could be successfully manufactured with this technology. In addition, it showed how the manufactured parts were capable of withstanding the OEM's requirements. However, the best of this process comes when observing its capability to drastically reduce the required raw material and energy consumption. These are really great results for a technology that was not obtaining such good outcomes for a long time.

Nevertheless, the reason why this technology works so well at those conditions is still unknown. This makes everything harder as it still means the need of continuing working under the trial-and-error methodology. Moreover, those results are not good enough for the industry to start considering a trial in their installations. Consequently, Universities and research centres have to continue developing these aspects before a company takes the leap. In an attempt to achieve further results and information about this process to continue with its development, this PhD has been launched.

1.3. Scope of the present thesis

Summing up the previous information, the objective of this PhD dissertation is twofold: first, to investigate and to try to shed light on why the steel is behaving as it does during the process enabling such great flow capabilities ("***O1***" in Figure 1.3). Second, to continue progressing on the components' manufacturing in order to bring the process closer to the industry ("***O2***" in Figure 1.3). These two goals will therefore help to increment the actual knowledge about the process and, consequently, to catch the interest of companies to start considering the viability of taking advantage of it. To attain these goals, this PhD work has been divided into the following sections:

1. Literature review: A brief history and summary of the most important knowledge about this technology is stated here. This section covers the information to understand the SSP from the material to the fabrication. Chapter 2 will be entirely devoted to explain those concepts.

2. Semi-solid forging (SSF) of steels: An overview of the actual SSF cell in MGEP will be given. All the different equipment the cell consists of and the manufacturing process itself are explained. In addition, the case of the fabrication of some steels are also assessed. Chapter 3 gathers all this information.

3. Softening phenomena: The analysis of three different hypothesis about the material behaviour is presented. The reason why these hypotheses agree with the observed material behaviour are justified with literature and further analysed in order to clarify the driving phenomena during the process. This is indeed the main objective of Chapter 4.

4. Microstructural evolution: How the microstructure has evolved during the process is assessed. An austenitic alloy has been subjected to the SSF process to observe the microstructure evolution. A complete analysis of the most interesting zones is described in Chapter 5.

5. Component mass production: The fabrication of a pre-series batch of 250 components is explained. All the aspects related to the manufacturing and component health are commented. Moreover, a mechanical and economic analysis has been as well performed. Chapter 6 contains all this information.

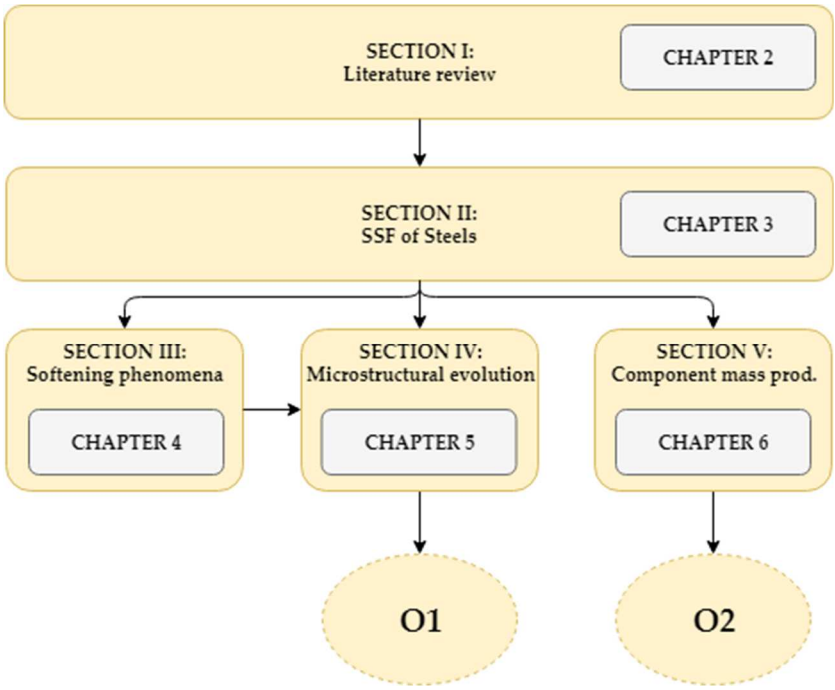

Figure 1.3 – Summarised structure of the present PhD dissertation.

As illustrated in Figure 1.3, the information in Chapter 2 is the base from the rest of sections are developed. Then, Chapter 3 gives a more detailed insight into the utilised equipment and the process itself. The information gathered in this section is, in turn, the main foundation for the subsequent work. In order to attain the objectives, sections III, IV and V have been established. The first objective is completely fulfilled after analysing the microstructure of a component in Chapter 5 and relating the observed results with the analysed phenomena in Chapter 4. The second objective is attained after the information acquired during the manufacturing of 250 components in Chapter 6.

Those analyses have been carried out by using different alloys. A schematic illustration of the utilised steel grades is shown in Figure 1.4. In Chapter 3, three different steel grades are tested: the two steel grades utilised for the conventional manufacturing of the components, 42CrMo4E and S48C, and the 44MnSiV6 microalloyed steel due to its capability to remove the postprocessing heat treatment.

In Chapter 4, the incipient melting phenomenon has been analysed on the 42CrMo4E steel grade as it has been previously proved the obtaining of sound components with as forged mechanical properties. Due to the same reason, the influence of Sulphur has been as well carried out with the same steel grade but with low (L), medium (E) and high (H) sulphur contents. Regarding the adiabatic heating, the Invar 36 austenitic steel that ensures no phase transformation from

working to room temperatures for a possible post-mortem analysis of the tested sample has been selected.

In the same fashion as in the previous chapter, the selected steel for Chapter 5 has been an austenitic alloy to attain post-mortem microstructural information. In this case, an Alloy 28 stainless steel has been utilised to this end. Lastly, in Chapter 6, the S48C steel grade is the utilised alloy for the 250 components manufacturing. This alloy is selected due to this steel grade is the utilised one in the conventional Hot Forging (HF) for the manufacturing of the selected geometry.

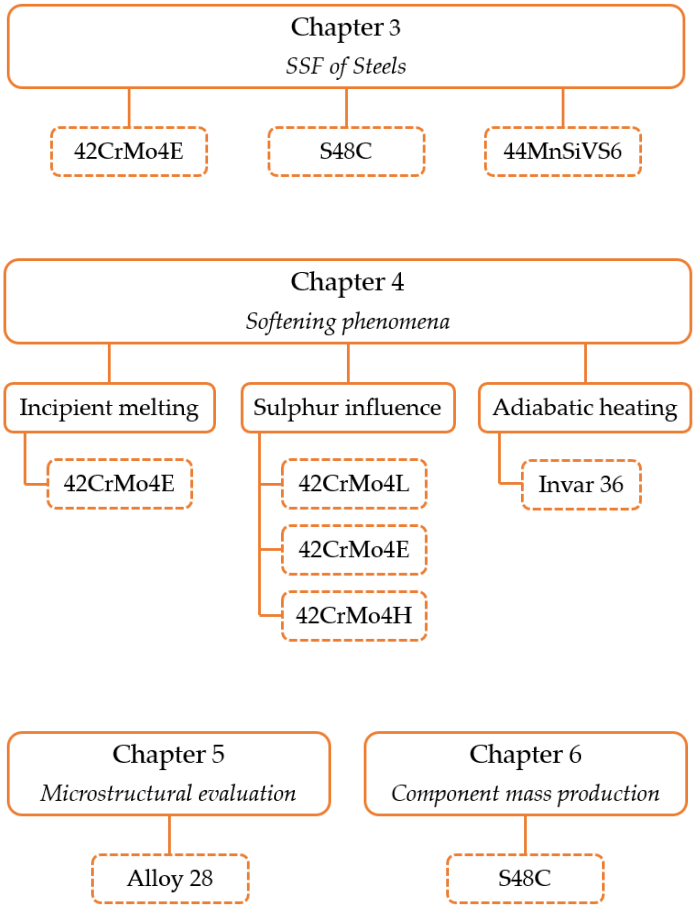

Figure 1.4 – Classification of the alloys utilised in each chapter.

Chapter 2

LITERATURE REVIEW

"To understand a science, it is necessary to know its history"

Auguste Comte

Summary

How can we know where we are if we do not understand where we come from? This is precisely the purpose of this chapter. It intends to give a brief overview of how everything has evolved until nowadays' situation. It focuses on the semi-solid metals since its special behaviour was discovered to the first components manufacturing by SSP. Recent studies on semi-solid metals from other fields are also summarised. In essence, this chapter will explain the starting point of the current PhD research.

This chapter will cover the discovery of the technology, its development and its industrialisation attempts. It will also go through the processes developed for high melting point alloys and how the microstructure deforms in the semi-solid state at high solid fractions. After critically analysing this literature review, a new research scenario will be suggested.

2.1. The beginnings of Semi-Solid Metal Forming

The SSP comes from the discovery of the thixotropic behaviour in metals by Spencer et al [14] in the early 70's at MIT. They accidentally found this phenomenon while performing viscosity experiments related to hot tearing in Sn-Pb alloys. They were the first observing the thixotropic behaviour in metals: the material flowed like liquid when sheared and it thickened again when allowed to stand enough time. In an attempt to take advantage of this specific behaviour, many patents were published by Alumax and ITT corporation [15]. As a consequence, the development of this technology was carried out under great secrecy and confidentiality, a fact that hindered its progress. Therefore, it was not until 1985 when this technology began to be investigated in Europe. Universities and research centres like the University of Sheffield, RWTH Aachen and the University of Liege, among others, were the head of the research in this field.

Main development and knowledge of the SSP processes was gained during years of investigation with low melting point alloys at high liquid contents [15], even some trials were carried out with stainless steels [16]. However, even if the components had less porosity and better properties, the high costs associated to the production of globular aluminium alloys compared with the die casting ones and the observed problems with repeatability during manufacturing stopped the development of this technology. In spite of this drawback, some electronic consumer goods and automotive components are still being manufactured by taking advantage of this technology [17]. As an example, Volvo is rheocasting aluminium components for trucks [18].

The interest in analysing this phenomenon in high melting point alloys began in 1990. A consortium based in Sheffield, where UK companies were involved, motivated the investigation. They are in fact the first in manufacturing a real component by SSP using steel at high solid fractions [19]. Since then, many researchers have tried to manufacture sound components by gaining advantage of this near-net-shape technique to bring it closer to industry without fortune [20,21].

2.2. Principles of thixotropy

As mentioned before, the thixotropic behaviour means a reduction of viscosity of the material when sheared and the recovery to its initial state after resting enough time. Its name comes from the Ancient Greek *"thíxis"* (touching) and

"tropé" (turning). The schematic illustration of Quaak et al [22] (Figure 2.1) explains the reason of having these flowing characteristics:

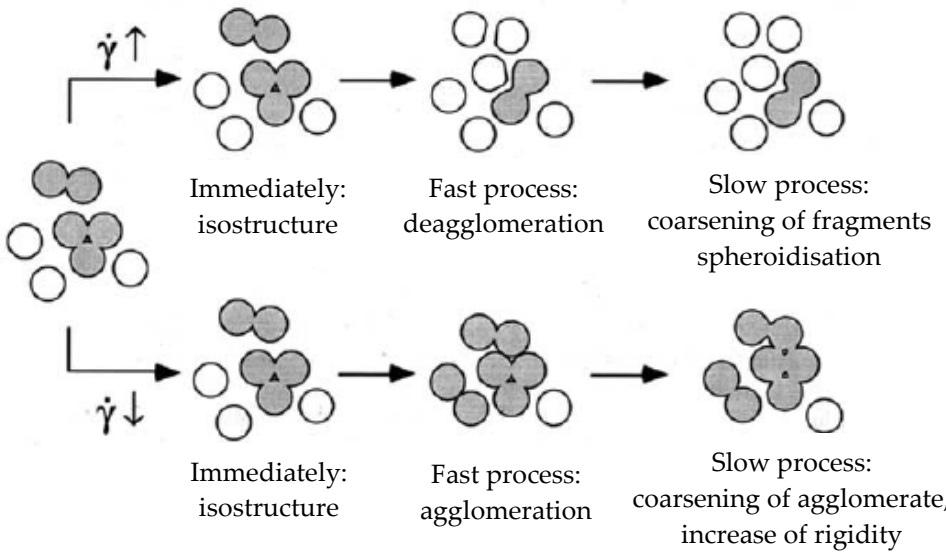

Figure 2.1 – Schematic model describing the fast and slow processes in a semi-solid material's structure after shear rate up and down jumps [22].

To flow thixotropically, the microstructure must consist of globular particles inside a liquid matrix. They are the responsible for creating the thixotropic phenomena thanks to the agglomeration/deagglomeration effect. When the material is at rest, the colliding particles create boundaries between each other building a 3-D solid network. Thus, even with high amounts of liquid (30-40%), the material is capable of holding its own weight without pouring. On the contrary, when shear is applied, the boundaries between particles break up letting the globules flow smoothly. Consequently, the viscosity is reduced enabling a liquid-like behaviour.

The main industrial advantage of this phenomenon is that complex geometries can be filled with an already existing certain amount of solid. In this way, the material has a lower amount of liquid to create porosity, hot tearing or cracking, a fact that influences directly the final component's properties. However, a globular microstructure is required for such purpose meaning that the material must be treated before manufacturing. In the following section, it is explained in more detail.

2.3. Semi-solid metal forming process types

There are two general processing types called *"Rheoprocesses"* and *"Thixoprocesses"*. As explained before, the material must be globular. The difference between them lies in the method to obtain the feedstock (Figure 2.2). In rheoprocesses, the material is melted and stirred during cooling to the desired solid fraction prior to the forming step. This stirring breaks the dendrite arms, enabling the creation of globules [23]. In the case of thixoprocesses, the material has been treated previously to obtain the desired globular microstructure. Different techniques to obtain the proper feedstock are listed in [24]. In this process, the treated material is directly heated to the working temperature before forming it.

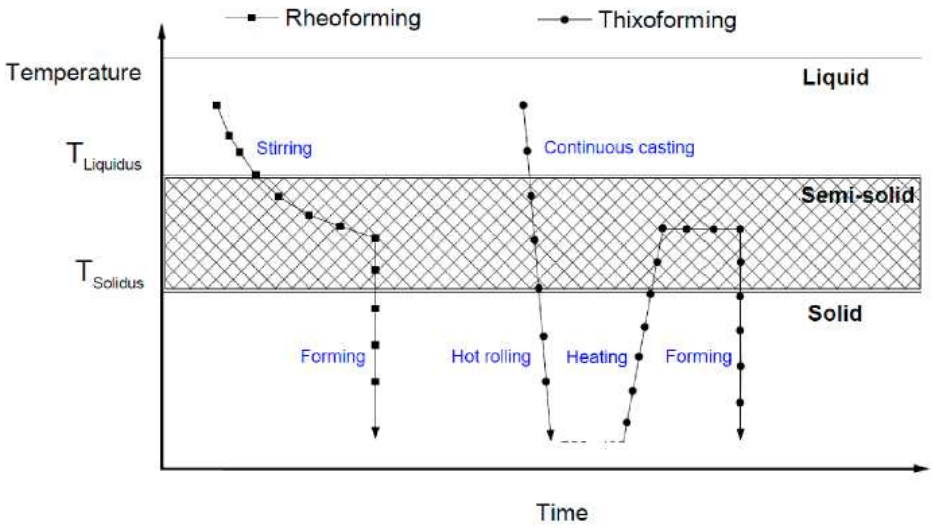

Figure 2.2 – Schematic illustration of different SSP fabrication methods cycles [25]**.**

The rheoprocesses need a specific equipment to cool and stir at the same time, which means an increase in the cost of the required facilities. In the same fashion, both the equipment to treat the material or directly the supplied treated material also means an increase in the cost of thixoprocesses.

So as for the forming step, the way the mould filling will be needs to be set. The component's geometrical complexity defines which set up may be used. For casting components, higher amounts of liquid would be needed. The contrary happens for forging like components. This information makes easier the selection of the set up that best fits the filling necessities (Figure 2.3).

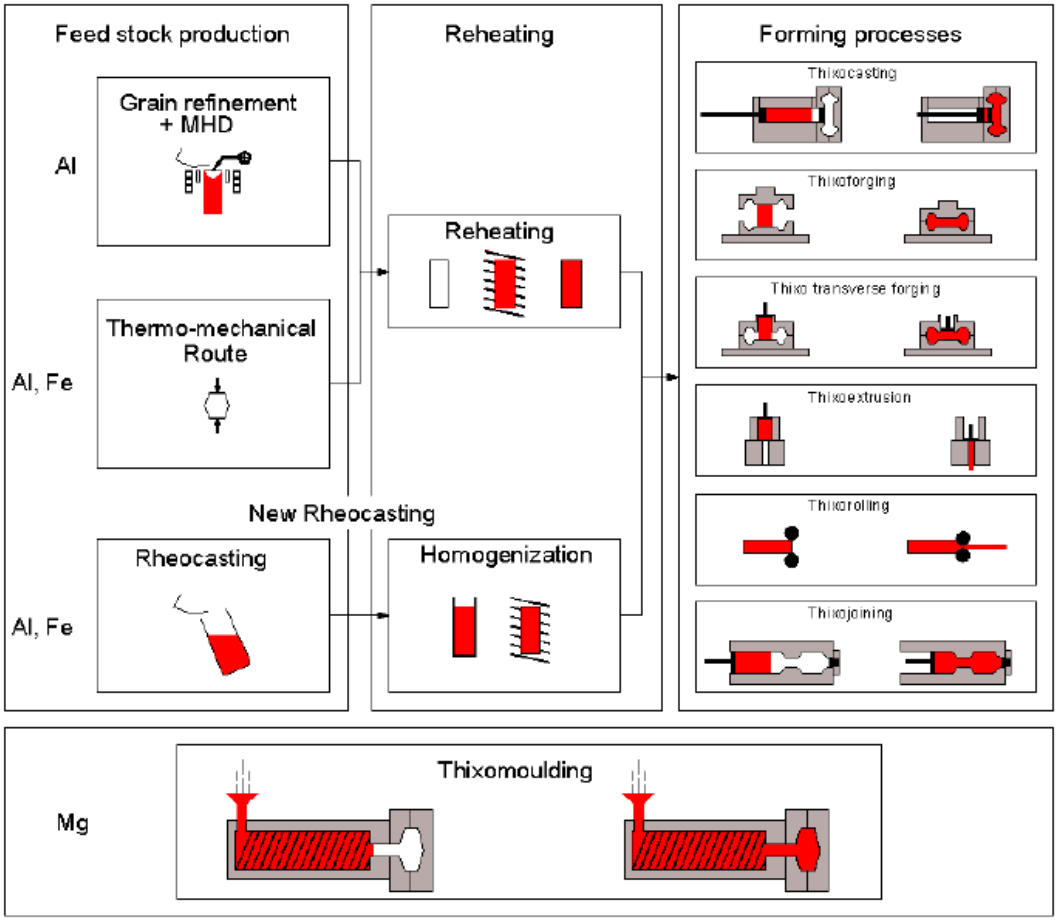

Figure 2.3 – Schematic illustration of different set ups for SSF [26]**.**

The limiting solid fraction that defines when to use a solid or liquid like equipment is different for each material. However, it is commonly between 40-50% of solid fraction. Below this percentage, casting processing setups are used whereas above it, forging, extrusion or rolling processing setups are usually selected.

Focusing more deeply on high solid fraction processes similar to that of a forging or extrusion, the amount of solid the material should have may be between 60% and 90%. This hypothesis comes from the observed limitations for high solid fraction processing [27]. On the one hand, below the 60% solid fraction the material may not be able of supporting its own weight without deforming itself. Moreover, the high liquid content could mean excessive porosity due to turbulent mould filling [28,29]. On the other hand, at solid fractions higher than 95%, the material stops behaving like a *"lump of clay"* to start behaving as a solid [30]. Therefore, solid fractions above 90% are avoided.

2.4. Component manufacturing with high melting point alloys

The first thixoforming process using high melting point alloys was carried out by Young and co-workers at MIT in 1979 [45]. They used two different grades of stainless steel (304 and 440C) to thixocast 300 hammers for M16 type rifle components. However, it was not until the 90´s when the first steel SSF component was manufactured using high solid fractions in Sheffield by Kapranos et al [19]. They fabricated some toothed cog wheels of 1.3kg using the M2 tool steel (Figure 2.4). From then on, several components have been manufactured [20,21] but excessive tooling damage and no competitive properties were achieved.

Figure 2.4 – SSF M2 tool steel toothed cog wheels [19].

Recently, last investigations carried out in MGEP [11,46–48] and ENSAM [49,50] show the capacity of SSF sound components fulfilling the OEM's mechanical requirements and manufacturing several thousand parts without no visible tooling damage. In the former case, they used medium carbon alloys at temperatures below the theoretical solidus measured by Differential Scanning Calorimetry (DSC) to manufacture an automotive spindle (Figure 2.5). Besides, near-net-shape advantages were also attained as the component was manufactured in a single step with a 400t press, in comparison to the 3 steps and 2500t press required in the forging industry. In addition, 20% of raw material saving was attained.

Figure 2.5 – SSF (left) and HF (right) components [46].

Moreover, in the last work carried out in MGEP [47], a commercially available 42CrMo4 medium carbon steel grade was used. This material was neither specifically designed for SSP, nor treated specially for the globular microstructure obtaining. In addition, the recorded temperature at the end of heating was 1360°C. After the handling step from the oven to the press, this temperature might have been reduced in the surface. Hence, the component was successfully manufactured presumably with a high temperature inhomogeneity and well below the theoretical solidus temperature measured by DSC. This opens a new stage in the research of this process as the material is not supposed to have liquid at these conditions, which has been the main argument to explain the observed ease of the material to flow.

2.5. Semi-solid behaviour: another point of view

Looking at those last results, it seems that the conventional knowledge about the semi-solid material behaviour at high solid fractions is not properly understood. In addition, many models have been tried to develop without excessive success [31]. As it has a higher content of solid, it is hard to ensure that the material will only have the effect of thixotropy. However, analysing the interaction between solids and solid and liquid is essential to understand and model how the material flow or evolves. As mentioned before, most of the state of the art about microstructure behaviour during SSP is based on the evolution of a globular microstructure in a liquid matrix when sheared. Consequently, a wide literature research about the semi-solid state at high solid fractions from another point of view has been carried out.

It has been found an extensive work on the development of mechanical behaviour in the microstructural evolution during solidification. As stated in the work of Gourlay and Dahle [32], the material starts transmitting shear and compressive strains at the so-called coherency point (around 15% solid fraction for highly branched dendrites and 50% for globules). At higher solid fractions, when the material starts forming solid-solid interfaces, tensile strains start being transmitted. This state is known as partially cohesive visco-plastic porous media saturated with liquid. The rheology at those conditions is widely studied as it seems to be critical in the formation of casting defects. This has motivated many investigations. A summary of the most interesting results regarding the microstructural evolution in the semi-solid state at high solid fractions can be found in the following lines.

2.5.1. Particle motion

Gourlay and Dahle [32] were one of the first in "in situ" observing the microstructural evolution at particle scale of semi-solid metals at high solid fractions during shearing. They observed similar rheology between partially solidified alloys with solid fractions slightly above the coherency point and cohesionless granular material such as dense sand. This conclusion was obtained after analysing particle motion of two hypoeutectic alloys, Al-7Si-0.3Mg and Mg-9Al-0.7Zn. Both consist of a mixture of liquid and primary solid (L+Al and L+Mg respectively) from 0 to 50% solid fraction.

During their trials at solid fractions between the coherency point and the 50%, they observed grain rearrangement phenomena which lead to liquid-filled channel or fissure creation in semi-solid metals. This rearrangement is known as dilation (Reynolds' dilatancy [33]) and can be defined as the creation of interstitial space due to particle motion (Figure 2.6). The liquid-filled fissure is known as a shear band, a region with a localised shear strain and where the solid fraction content is decreased due to dilation (Figure 2.7). Hence, this rearrangement of particles also causes local solid packing [34]. This, therefore, leads to a highly inhomogeneous and localised deformation in shear bands. This phenomenon was also detected in globular Fe-C alloys at solid fractions between 40 and 55% [35], during compression test of dendritic Al-15Cu alloy at around 70% solid fraction [36] and in globular Al-Cu alloys during high solid fraction compression tests [37].

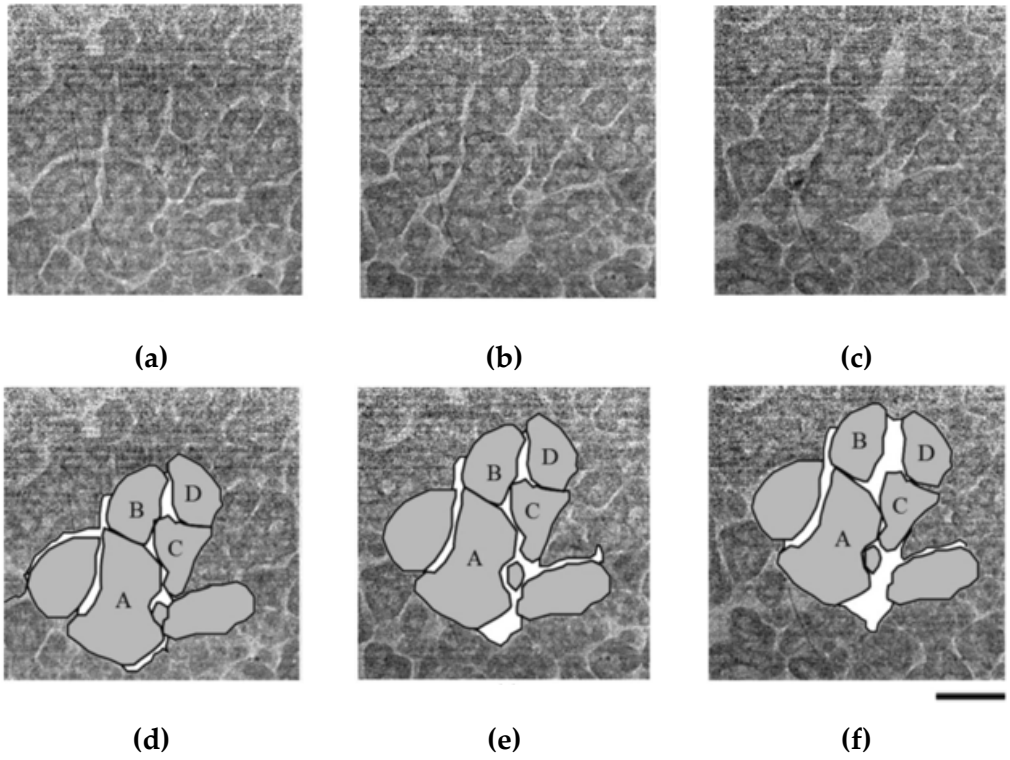

Figure 2.6 – (a-c) In situ microstructure of the semi-solid metal during shear tests at three different depths. (d-f) The dilation of the solid particle assembly, where liquid regions between solid particles are defined as white [38]. Scale bar: 300 μm.

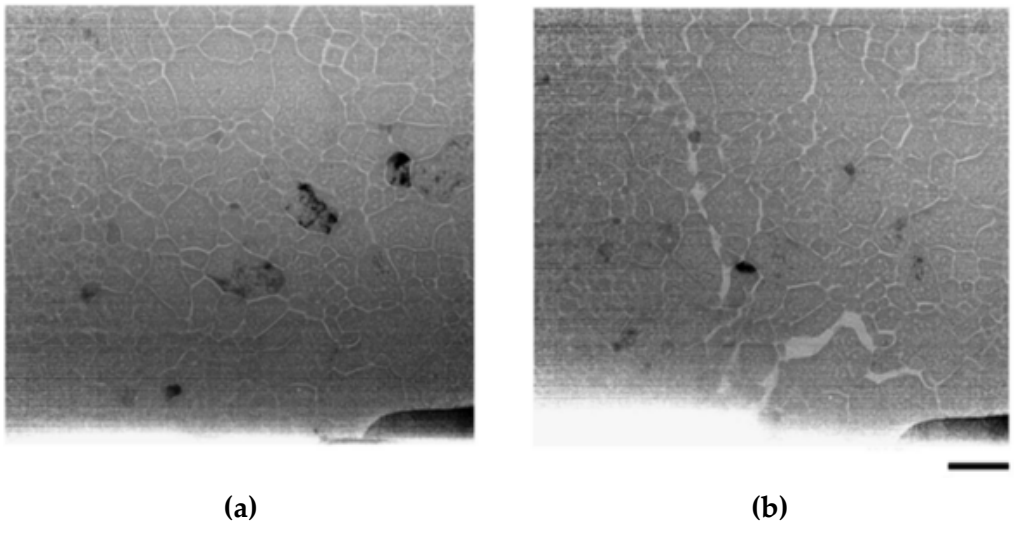

Figure 2.7 – Microstructures before (a) and after (b) the shear test. In the right microstructure the created shear band can be observed [38]. Scale bar: 500 μm.

With regard to steel at high solid fractions, Nagira et al [38] observed the same phenomena in Fe-2C steel at 85 and 90% solid fractions, and in Fe-0.45C-0.8Mn-0.3Si at around 93% during shear tests at $10^{-1}s^{-1}$ shear rate. They noticed that

particle rotation has the most important role in shear-induced dilation. Therefore, as the motion of particles (translation and rotation) decreases by increasing solid fraction, wider shear bands are created at lower solid contents. In this case, the resulting shear band at 85% solid fraction was 10 times the mean particle diameter, whereas it was 1 time for 90%.

Nevertheless, Cai et al [39] observed a sponge-like compressive behaviour during upward extrusion of Al-15Cu dendritic alloy at around 73% of solid fraction. They observed that the strain was mostly accommodated by inter and intra-grain compaction of dendrites with only a small amount of dilation (granular behaviour). As shown in Figure 2.8, the extruded area was almost uniquely liquid (liquid segregation). The remaining liquid volume in the downer compressed zone was around 15% (85% solid). However, this sponge-like behaviour is not detected during extrusion of the same material with globular structure [40], where a granular flow is observed (Figure 2.9).

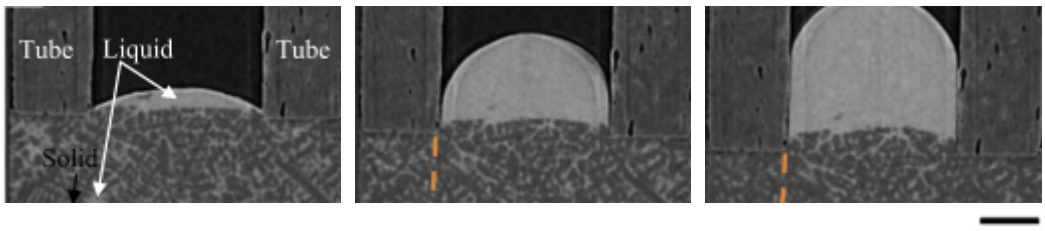

Figure 2.8 – In situ longitudinal slices during extrusion of equiaxed Al-15Cu alloy at 73% solid fraction at (a) 0 μm, (b) 162 μm and (c) 324 μm extrusion ram positions [39]. Scale bar: 500 μm.

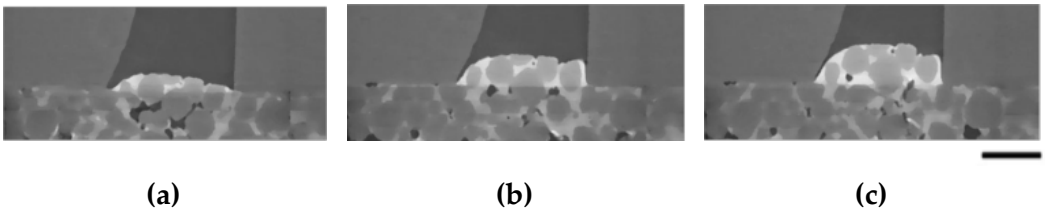

Figure 2.9 – In situ longitudinal slices during extrusion of globular Al-15Cu alloy at 73% solid fraction at (a) 0.5 mm, (b) 0.85 mm and (c) 1.02 mm extrusion ram positions [40]. Scale bar: 1 mm.

2.5.2. Defect creation

Gourlay and Dahle [32] noticed localised bands of porosity due to solidification shrinkage as the solidification of such zones are not adequately compensated. In addition, localised bands of positive macrosegregation are also observed due to the high amount of liquid fraction. Both defects are created at solid fractions between the coherency point and the fraction where crack propagation begins. This range depends on microstructural parameters and deformation conditions. In the case of the dendritic aluminium alloy, this range was observed to be between 20 and 35% of solid fraction. This phenomenon happens until higher solid fractions in globular and more compact dendrites microstructures as they exhibit a macroplastic response (without cracking) at solid fractions higher than 50%.

At high solid fractions cracking is observed (Figure 2.10) [37]. According to Nagira et al [38], when the solid fraction increases, the permeability for liquid flow around the solid particles generally decreases. Moreover, at relatively high shear rates it seems to be difficult for liquid to flow through the expanding spaces due to dilation, which means a decrease in the liquid pressure. When this pressure decrease happens, cracking is expected to form.

The work of Kareh et al [41] analyses three-dimensionally the pore behaviour during compression of globular Al-15Cu alloy at 64% and 93% of solid fraction. They observed a reduction of porosity during compression in the first case as a consequence of particle rearrangement, moving grains closer to each other and, thus, closing pores (Figure 2.10 (a-c)). In contrast, the pores grow during the test at 93% (Figure 2.10 (j-l)). This was observed to be caused by shear-induced dilation (cracks creation). In samples of 64% solid fraction, two types of pores were observed: tortuous and round. It was observed that tortuous pores maintain a near-constant volume during deformation whereas the round ones disappear or decrease in diameter. This diameter reduction was found to be correlated to the α-Al grain configuration and the grain packing density around the pore.

Cai et al [36] analysed the same Al-15Cu alloy at solid fractions around 70% but with dendritic microstructure. They observed three stages in void evolution during compression tests. In the first stage, the pore shrinks as a result of grain rearrangement and the subsequent liquid feeding, caused by compressive strain. In the second stage, new pores are created and existing ones increase their dimension along dendritic boundaries. Lastly, voids rapidly grow and coalesce leading to cracks.

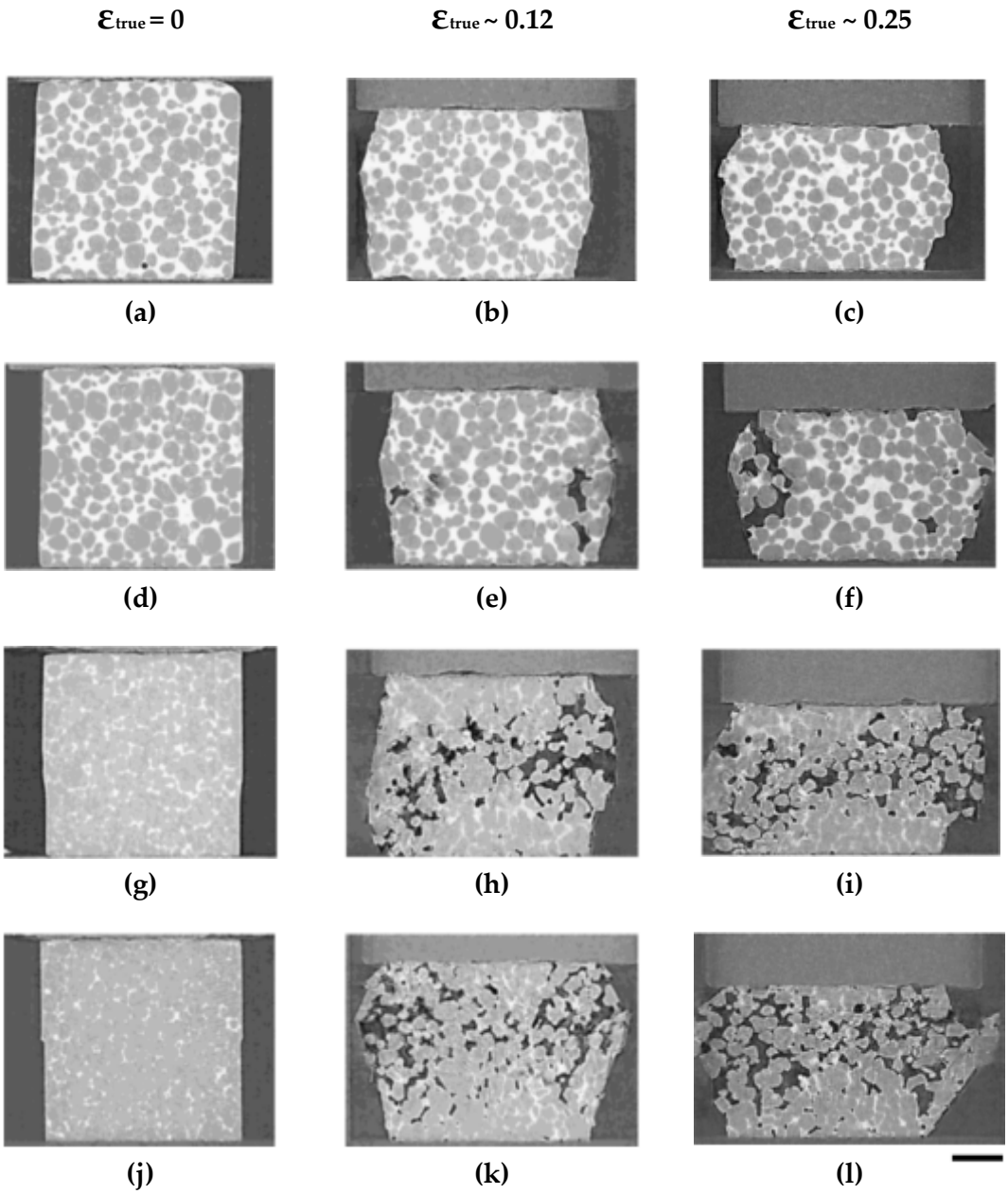

Figure 2.10 – In situ X-ray tomography images during uniaxial compression at (a-c) 64%, (d-f) 73%, (g-i) 86% and (j-l) 93% solid fractions. Scale bar: 1 mm [37].

2.5.3. Particle deformation

2.5.3.1. Dendritic particles

As indicated in the work of Cai et al [36], during compression of Al-15Cu alloy with 70% of solid fraction, the dendrites are sheared by their neighbours through a direct-shear mechanism. This shear force is high enough to create a bending moment capable of deforming the dendrite arms and, ultimately, of breaking off

portions of these grains. They ordered the predominant particle deformation mechanisms by appearing frequency: dilation, grain deformation and dendrite fragmentation.

They also observed a local remelting of solid grains due to thermal solute convection, an effect that is usually noticed in dendritic solidification during solute freckles creation [42,43]. There, around the created dendritic arms, the concentration of lower melting point alloying elements in the liquid phase increases. This leads to a decrease in the local equilibrium melting temperature enabling a localised grain remelting. In this case, not the freckle creation but the grain dilation causes the required local increase of Cu liquid concentration around dendrites enabling the grain remelting. Therefore, this leads to an increase in the liquid volume in localised dilated regions.

2.5.3.2. Globular particles

According to the works of Gourlay et al [34] and Nagira et al [38], sample deformation has been shown during shear tests without discernible deformation of individual particles at medium (around 50%) and high (up to 93%) solid fractions respectively. They found that the globules translate and rotate as a quasi-discrete body under forces acting at globule-globule contacts similar to granular materials as water-saturated sand.

The same conclusion was obtained by Kareh et al [40] during in situ extrusion experiments with a globular Al-15Cu alloy at 73% solid fraction. The globules translate and rotate, even contacting between them. When two globules touch each other, they roll off one another and end up the experiment losing their contact (Figure 2.11). This was found to happen thanks to a continuous liquid film separating the globules.

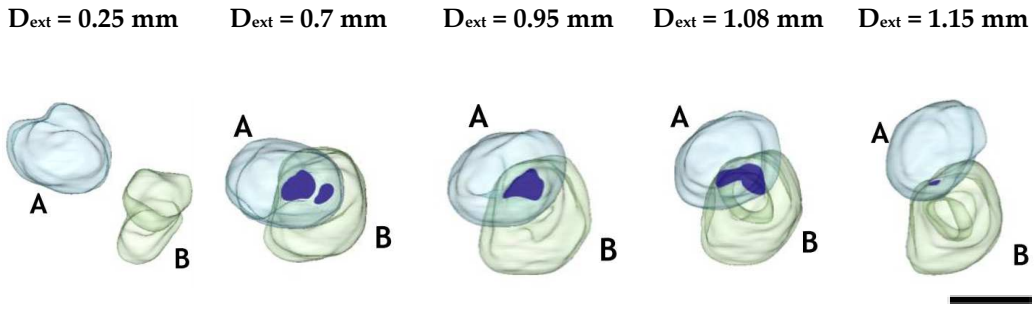

Figure 2.11 –Tracking of two globules during the extrusion shown in Figure 2.9. They are acting as discrete particles, coming close to each other and rolling off one another. The highlighted area is the contact zone [40]. Scale bar: 500 μm.

However, last investigations of Karagadde et al [44] show that transgranular liquation cracking of globules can occur in semi-solid materials by immersing an indenter (Figure 2.12).

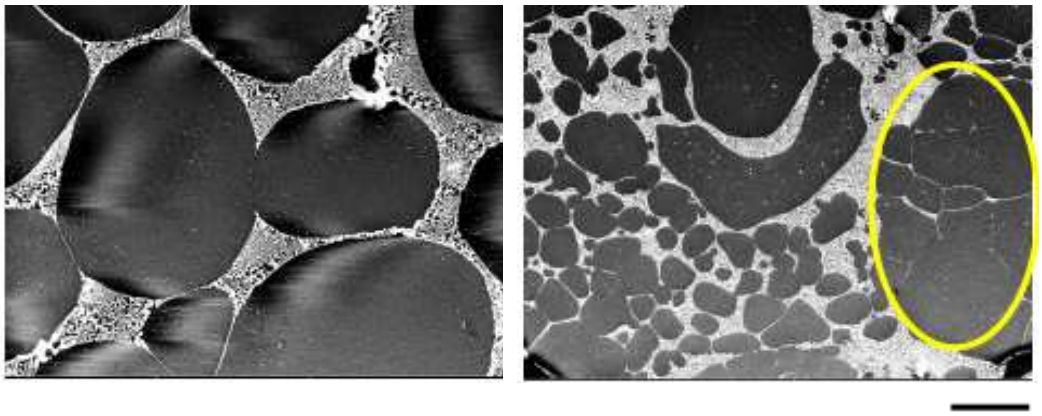

(a) **(b)**

Figure 2.12 – SEM micrographs of the (a) initial sample and (b) the cracked final specimen after indentation at 2μm/s at 555°C. The highlighted area shows how the transgranular liquation cracking starts in a grain (Supplementary in [44]). Scale bar: 250μm.

They consider that this phenomenon happens due to a combination of events shown in Figure 2.13. The studied material was a globular Al-Cu alloy at a high solid fraction (73%). Therefore, the compression enables the dilation phenomena making the liquid phase to flow through lower pressure regions, forcing the solid grains to contact each other creating a force chain (Figure 2.13 (a)). As a consequence of this contact, compressive and shear loads appear between them (Figure 2.13 (b)). This will produce elastic and small plastic deformations, generating dislocations that move fast to the surface. They seem to pin and interlock causing roughness at the surface and a localised remelting (Figure 2.13 (c)). Lastly, the intergranular liquid goes through the crack generating the transgranular liquation cracking phenomenon (Figure 2.13 (d)).

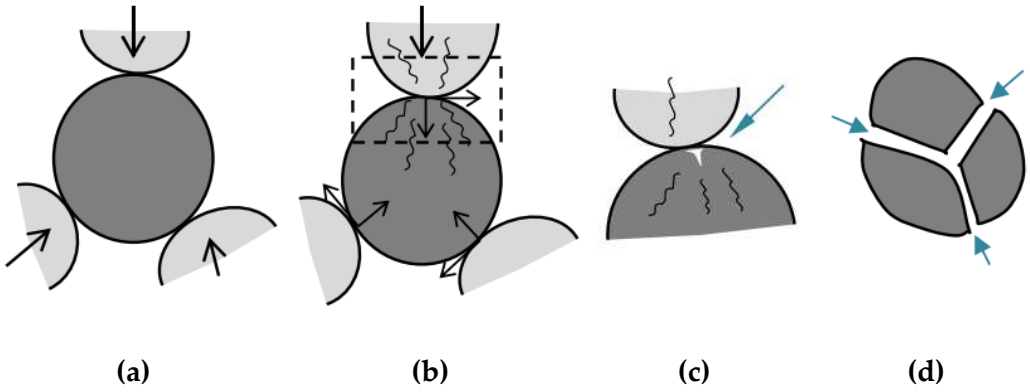

Figure 2.13 – Schematic illustration of the four stages of transgranular liquation cracking [44]. (a) grain contact, (b) generation of compressive and shear stresses, (c) localised remelting and (d) transgranular liquation cracking.

2.6. Discussion

Semi-solid behaviour

First of all, the work of the researchers during the material solidification on how the semi-solid material deforms at high solid fractions seem to clarify some aspects that were not properly explained in the conventional SSP field. They observed a granular behaviour of the material, which means that the grains have the capacity of sliding each other thanks to a small liquid film between them even at high solid fractions.

Looking at this information, it is possible to interpret that this material behaviour could be similar to the shear thinning if the grains have space to move (for example, the case of extrusion). However, when they are forced to contact between them, the strength required to deform it will increase. This behaviour could fit and explain the reason of having low forces during the SSF process until the last stage where the material starts being compacted, where it suddenly increases, as recorded in the work of Lozares et al [46].

Nevertheless, the most shocking result is the capability of the dendritic microstructure to have the same granular behaviour. It is true that they start being more difficult to deform at earlier solidification stages than globular particles (different coherency point) and this could imply liquid segregation during SSP. Even so, they still suffer the dilation effect, which suggests that even with the requirement of higher forces, they still should be able to be subjected to the SSF.

In addition, those results seem to confirm that the last compaction stage is closing the cracks that appear during the process. They also suggest that not only strain induced grain refinement can happen during the process, but also intragranular cracking refinement.

However, all those conclusions are based on the existence of liquid. But if there is no liquid in the material after the heating process as suggested by the work done in MGEP but it still deforms properly, which could be the reason of the material to behave as it does? Could it be related with the deformation?

Similarities with the conventional Closed Die Forging (CDF)

Going to manufacturing processes where the material is in the solid state, the most similar fabrication process is the Closed Die Forging (CDF). This technique has a very similar set up to that of the cell installed in MGEP where the material flows through a system of two closed dies thanks to the movement of a punch. The CDF is a near-net-shape process as it does not create flash. Moreover, it can be even closer to the net-shape if at the end of the manufacturing process a Precision Forging (PF) step is applied. This last process consists of a cold or semi-hot forming process to attain the required surface finish and tolerances, which implies an even higher material saving as there is no requirement of material allowances [51].

The CDF is commonly performed preceding the last PF step. It consists of attaining the best preform while saving material for the subsequent PF. Depending on the geometry, it is usually deformed either in hot or semi-hot conditions and commonly consists of 2-5 forging operations. In addition, the components manufactured via this technique are commonly suggested to be axis-symmetric and extrusion-like parts as this deformation mode prevents the material from losing cohesion due to the generated triaxial compressions stresses [51].

Comparing the analysed information, it seems that there is something that makes the difference between the process carried out in MGEP and the CDF. While the first means a unique manufacturing step, the second always implies 2 or more forging operations. Initially, only the temperatures seem to be different, which does not even suggest to be enough to generate liquid so as to explain the material behaviour difference. Hence, what could be going on? Is the material at these conditions extremely soft? Or has the liquid been generated due to other influencing factors? This PhD dissertation will try to answer these questions.

Chapter 3

SEMI-SOLID FORGING OF STEELS

"If you can't explain it simply, you don't understand it well enough"

Albert Einstein

Summary

The knowledge of how the process is carried out is vital to understand the problem and, therefore, to decide the forthcoming steps. This chapter gathers all the required information to properly understand how the SSF process is performed in term of facilities and manufacturing process. Aiming to find some limitations to the SSF process, several experiments have been done with different steels attaining some interesting outputs that broaden even more the process possibilities.

This chapter will, therefore, explain the equipment of the cell as well as the steps required to manufacture a component. Then, three different medium carbon alloys will be subjected to SSF in order to detect the process limitations and to widen the steels that have shown their capability to be used in the SSF. Moreover, two different spindle geometries are utilised to observe how the material fills the cavity depending on the complexity of the part.

3.1. Introduction

It is worth highlighting one more time the results achieved in MGEP. It was proved how sound automotive spindles can be successfully manufactured by SSF not only meeting the mechanical requirements but also reducing the manufacturing costs. The near-net-shape capabilities of the process made possible the save of a 20% raw material. This fact influences directly the final cost of the component, as the cost of the material is close to the 30-50% of the total amount. In addition, the material's deformation characteristics made also possible to reduce the manufacturing process to a unique forging step in a 400t press, in comparison with the 3 forging steps followed by a trimming stage in a 2500t press of the conventional HF process.

The difference between both lies in two main factors: working temperatures and tooling set up. While the HF consists of temperatures as high as 1250°C and an open die tooling design (in the studied case), the SSF goes beyond those temperatures in a closed die configuration. Therefore, it is still not ensured a cost reduction related to energy from reducing the forging steps as the heating cost would increase. Nevertheless, it does ensure a material cost reduction and a higher efficient process.

This chapter intends to give an overview of how the components are made in MGEP explaining the facilities and the process itself. This knowledge is necessary to understand the problems this dissertation faces in more detail. Furthermore, in an attempt to show the limits of the process, several different materials have been subjected to the SSF process. Note that the aim of these tests is observing the filling capability of the materials at different conditions. The analysis of the process from a more industrial point of view is assessed in Chapter 6.

3.2. Semi-solid forging cell

The beginnings of the SSF cell as we know it today comes from the requirement of fast forming speeds and final squeeze holding to SSF aluminium alloys by Azpilgain et al [52]. At that time, these requirements were only fulfilled by hydraulic presses. However, a new kind of servo motor driven mechanical presses (servo-mechanical press) were coming out. This press type was selected as the position control and speed performance were satisfied.

Looking at the potential this press implies in terms of widening the research capabilities, a leap to SSF high melting point alloys was considered. However, the actual tooling designed for aluminium alloys was not prepared to handle steels.

Hence, the PhD of Lozares was launched [13]. He designed and fabricated the tooling for high melting point alloys and led the automation of a cell that consisted of an induction equipment, a handling robot and the servo-mechanical press. In the following lines, each element of the cell is briefly described. For further information about the cell go to [13].

3.2.1. Servo-mechanical press

The press of the cell is a Fagor 400t AC servo-mechanical press. The main differences between the hydraulic and servo-mechanical presses are the higher productivity, better product accuracy and better machine reliability the latter gives. Moreover, its most important feature is the flexible ram movement that enables a wide range of working cycles. Even though, as a consequence of the movement of the connecting rod, the maximum press capacity is only available in the last stages of the ram movement. In the following table (Table 3.1) the main characteristics of the press are shown:

Table 3.1 – 4000 kN servo motor driven mechanical press [13].

Servo motor driven mechanical press SDM2 - 400 - 2400 – 1200	
Press capacity (kN)	4000 at 20mm from the BDC
Number of points	2
Working torque Max / Nominal (N.m)	5500 / 3000
Max stroke (mm)	400
Max ram speed (mm / s)	800
Die height (mm)	1000 to 1200 (stroke 400mm)
Stroke adjustment (mm)	200
Table size (mm x mm)	2400 x 1200
Max cadence (spm)	100
Die cushion capacity (kN)	400
Die cushion stroke (mm)	100
Motor power Max / Nominal (kW)	450 / 250

3.2.2. Induction equipment

The induction heating method is one of the most effectives to electrically heat conducting materials. It is based on inducing eddy currents in the billet that will, therefore, heat the material by Joule effect. However, as the generated magnetic fields are stronger closer to the coils, the surface of the sample will be affected by the highest amount of power, generating the so-called skin effect (hotter the surface than the core). Consequently, a heating cycle of several stages has to be designed to heat the billet up homogeneously. The following are the characteristics of the induction equipment of the cell (Table 3.2):

Table 3.2 – EFD induction heating equipment characteristics [13].

EFD induction furnace	
Power max.	150 kW
Frequency	1.7-3 kHz
Atmosphere gas	Argon

3.2.3. Handling robot

Controlling the temperature of the billet is of great importance. The temperature is definitely an influencing parameter against the material behaviour. Therefore, it is important to lose as less heat as possible during the movement of the billet from the oven to the press. Consequently, a six-axis KUKA robot with a self-designed grip (see [13]) has been installed in the cell to ensure a fast and reproducible material transfer. In addition, this will let us reduce the overall manufacturing time, being closer to industrial reality.

3.2.4. Tooling for high melting point alloys

In Figure 3.1 the tooling designed in MGEP is shown. It consists of an upper and bottom die holder connected by two hydraulic cylinders that enable the opening and closing. This movement is guided by four columns installed in the bottom die holder. In the upper die holder, other four hydraulic cylinders are placed with the aim of ensuring a proper clamping to prevent the dies from separating during the process. The bottom die holder has some holes to let the expulsion system go through to eject the component.

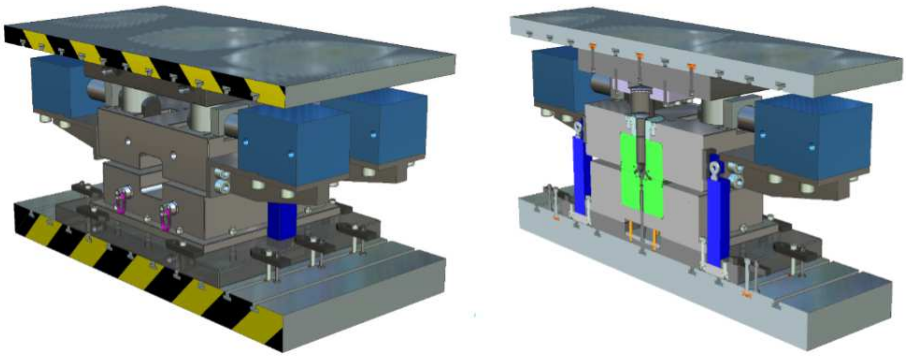

Figure 3.1 – CAD design of the forming tool [13].

During this dissertation, some modifications have been performed on this initial tooling (Figure 3.2). To ensure a faster and more controlled die opening, four new hydraulic cylinders have been placed connecting the upper and bottom die holders. Moreover, to make the whole process of die closing, opening and clamping faster and more efficient, a new hydraulic installation has been built based on a higher capacity hydraulic group. The cylinders' displacement is now controlled by several flow dividers that ensure all cylinders are moving at the same speed and time.

Figure 3.2 – Actual tooling for SSF.

3.3. Semi-solid forging process

The SSF process in the cell of MGEP consists of an initial billet heating in the induction furnace, the billet transfer to the press followed by the material deformation and component ejection. Each stage of the process is explained in more detail in the following sections.

3.3.1. Initial preparations

Before beginning with the component manufacturing, several preparations take place. First of all, the dies are preheated up to 270°C with the flow of oil through the tempering channels. Then, a CeraSpray® long-lasting ceramic varnish with lubricant effect that acts also as a thermal shock barrier is applied in both dies and punch (as suggested by Pierret et al [53]). Once the previous one is properly carried out, the dies can be closed and clamped, leaving everything ready to start with the manufacturing process.

3.3.2. Heating of the billet

It has been mentioned previously how the induction equipment implies an unavoidable inhomogeneous heating due to the skin effect. To overcome this problem, a several stage heating cycle was designed considering the recorded temperature of two S type thermocouples placed in the centre and surface of the billet (Figure 3.3 (a)). The minimum power the induction equipment gives is 24 kW, high enough to heat up the sample to the working temperatures. Therefore, after several trials, he obtained the optimum heating design to ensure the homogeneity by dividing the cycle in four heating (at 24kW) and three holding steps (switching off the power). This heating cycle lasts 231s. The resulting curve for the case of a C45 medium carbon steel is shown in Figure 3.3 (b). Note that the heating is carried out under a flow of 14-20 l/min of Argon to avoid the generation of oxide in the surface of the billet.

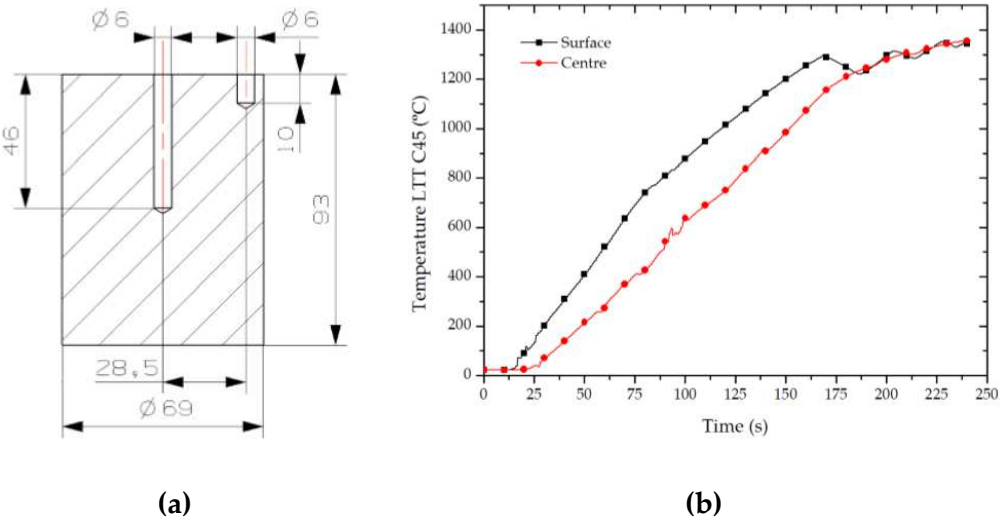

(a) **(b)**

Figure 3.3 – (a) Schematic illustration of the thermocouple location into the billet and (b) the temperature evolution curve for a C45 steel grade [13].

3.3.3. Transfer stage

Once the billet's heating is finished, the robot takes and places it in the press. As this movement must be fast, the robot is moving at his higher speed. The transfer time is about 12-14 seconds. However, the robot must know when to hold the billet and when to send the signal to the press to start the deformation. For that purpose, the communication between the induction equipment, robot and press is done using direct wiring and digital I/O lines. Hence, the robot controller is the responsible for the overall coordination even if the induction furnace and the press have their own hardware to define both the heating and deformation cycles.

In terms of security of the SSF cell, the robot has some sensors that detect collisions and inhibit its movement. In order to comply with the regulations, the cell is sealed with railings and equipped with a door that must be locked to keep the cell working. If the door is opened during the process, everything stops.

3.3.4. Deformation stage

The deformation stage consists of moving the punch at the maximum speed from the top dead centre (TDC) to the bottom dead centre (BDC) of the ram. The ram position is defined considering that the stroke of the press is 400mm and that the maximum load is only attained at the last displaced distances. In this case, the punch is maintained at the BDC compressing the material for 5 seconds. This step intends to prevent micropores and cracks from appearing in the component during

the solidification of the liquid phase. An example of the cycle is shown in Figure 3.4.

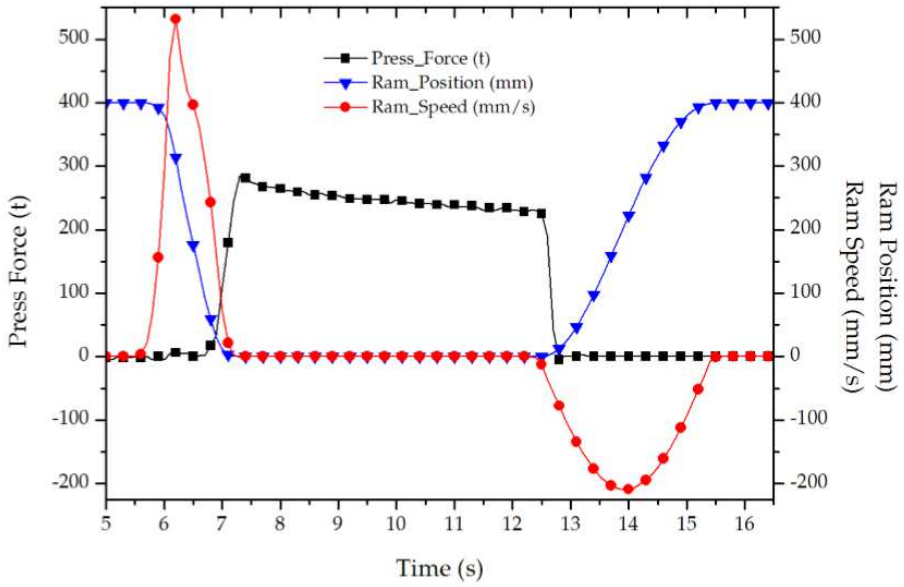

Figure 3.4 – Press force, ram position and ram speed during the process [13].

As a consequence of the ram deceleration when approaching the BDC, the speed is decreasing in the last stages of the displacement. Therefore, the obtained speed is the maximum the press can give considering this last fact. The ram speed when the material starts to deform is close to 410 mm/s. As observed in Figure 3.4, the registered maximum loads in the experiments carried out in MGEP were usually around 300t. Note that this load is not only from material resistance to deformation but also from the press frame deformation during the process.

3.3.5. Component ejection

To eject the component, once the deformation stage has finished and the ram is at the TDC, the clamping system retraction and die opening is manually activated. Once the dies are fully separated, the pneumatic cylinder of the press is manually activated to eject the component. Then, an operator is the responsible for retiring the component from the press and cleaning the dies.

3.4. Component manufacturing with different steel grades

3.4.1. Spindle geometries

The spindle, acting as a short axle, is the responsible for attaching the wheel assembly to the steering system. It pivots between the upper and lower A-frames or on the strut. Both the inner and the outer wheel bearings ride on the spindle. The retaining nut on the end secures the wheel into position. The component usually acts as the frame where the brake calliper is fixed. They are typically forged as they must be extremely strong and durable to support the weight of the vehicle. The Figure 3.5 shows schematically an assembly example.

The two spindle geometries used in this dissertation are shown in Figure 3.6. Considering that the disposal of the dies implies a downward flow of the material to fill the axle, the complexity difference between both lies in the larger material flow through a thinner cross-section in the perpendicular to the axle direction that is required to fill the cavity of the H spindle (Figure 3.6 (b)). In any case, both geometries correspond to very complex shapes according to EN 10243-1. The R component weights ~3 kg in comparison with the ~2.3 kg of the H one. Therefore, the initial billet for the H component is slightly smaller.

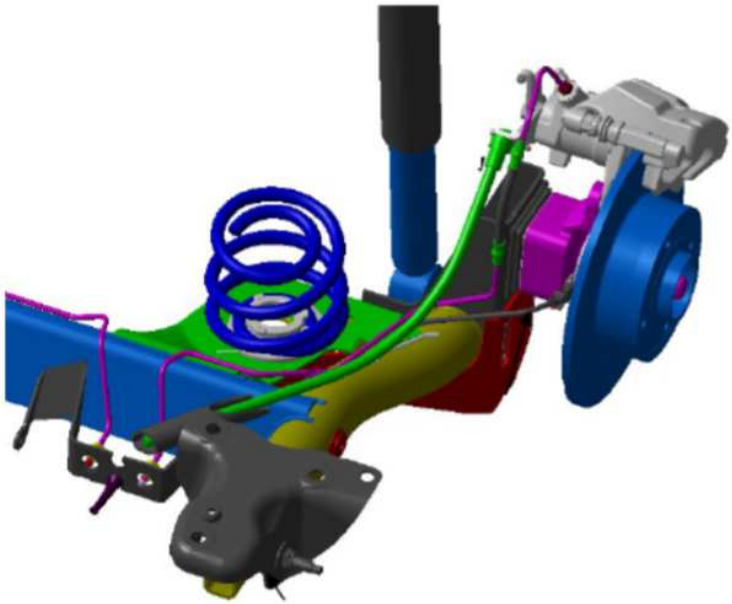

Figure 3.5 – CAD drawing of the rear suspension with the spindle in violet [13].

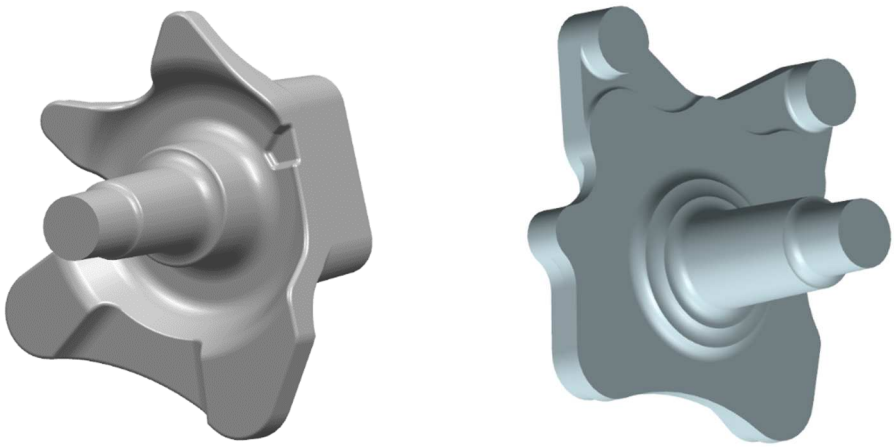

(a) (b)

Figure 3.6 – CAD drawing of the spindle geometries used in this dissertation: (a) R spindle (around 3 kg) and (b) H spindle (near 2.3 kg).

3.4.2. Materials

Now that one has an idea of how the process works and the components that will be manufactured, it would be easier to understand the following material selection (Figure 3.7).

The first material to test is the 42CrMo4E. This steel grade is selected first because it is the material utilised in HF for the R component manufacturing and second because there are already sound components with good mechanical properties manufactured via SSF [47]. Different manufacturing conditions will be tested with this steel in an attempt to observe the limits of the process.

Similarly, the selection of the S48C steel grade comes from its use in HF for the H component manufacturing. In this case, the aim lies on observing if a component of higher complexity can also be successfully manufactured via SSF with this steel grade. Lastly, the 44MnSiV6 microalloyed steel is an alloy designed to obtain great mechanical properties without any postprocessing heat treatment. Consequently, this steel will be tried to observe if it can be manufactured via SSF to make the process even more cost effective.

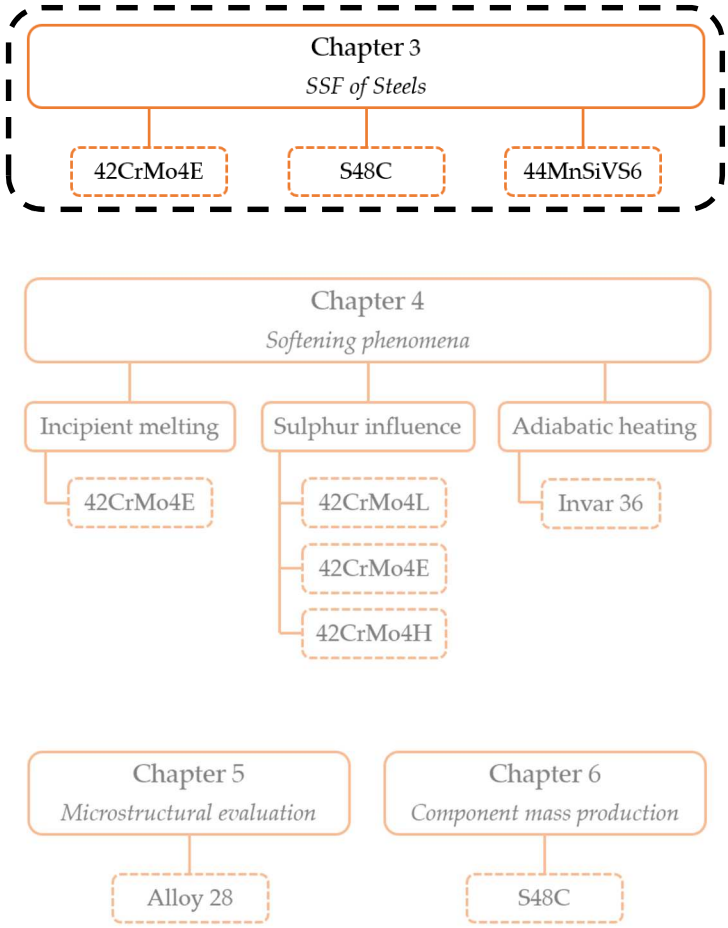

Figure 3.7 – Selected steels for the experimental procedure of the Chapter 3.

3.4.3. Medium carbon quenching and tempering alloys

3.4.3.1. 42CrMo4E

The 42CrMo4E steel grade, also known as 1.7225 or F-1253, is a commercially available quenching and tempering alloy commonly used in aeronautic and automotive industries. The steel grade was supplied by SIDENOR in cylindrical bars after hot rolling and a quenching and tempering heat treatment (Figure 3.8). The following table (Table 3.3) shows its chemical composition:

Table 3.3 – Chemical composition of the 42CrMo4E steel grade.

C	Mn	Si	P	S	Cr	Ni	Mo
0.42	0.80	0.25	0.011	0.024	1.08	0.10	0.21

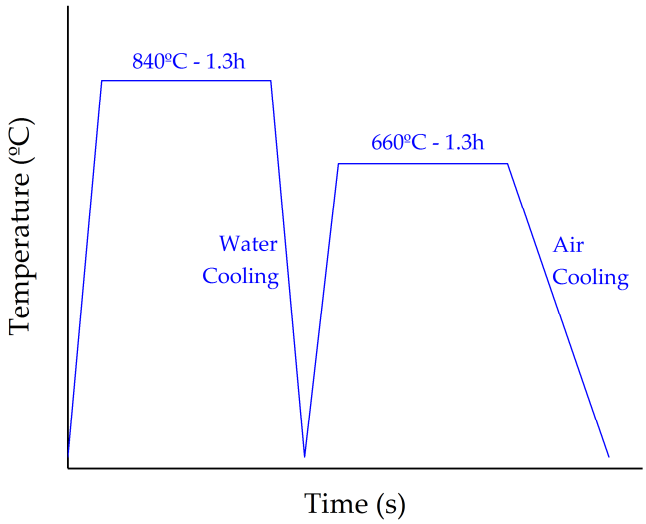

Figure 3.8 – Quenching and tempering heat treatment of the as supplied 42CrMo4E steel grade.

It is true that the 42CrMo4 steel grade has been successfully utilised during the SSF process previously in MGEP. Nevertheless, it has been manufactured with working temperatures of around 1360°C. This temperature was set up by trial and error. Lozares [13] began with temperatures inside the semi-solid state according to the DSC, but pores and cracks appeared. He then started to decrease the temperature until sound components were achieved. This last recorded temperature is in fact 1360°C.

However, it is still not known if at lower temperatures the component may be as well successfully manufactured. To tests that, three different manufacturing experiments have been carried out with this steel grade and the R geometry. The first one consists of reproducing the same manufacturing conditions as in the work done in MGEP [47] to be sure that the material will deform. Then, other two manufacturing trials are carried out removing the last and the two last heating stages respectively. The temperature of the billet in the centre and surface are the following (Table 3.4):

Table 3.4 – Billet temperatures for each manufacturing conditions.

1st trial		**2nd trial**		**3rd trial**	
T Centre	T Surface	T Centre	T Surface	T Centre	T Surface
~1360°C	~1360°C	~1340°C	~1360°C	~1290°C	~1315°C

It has to be considered that the transfer time from the oven to the press can lead to a considerable decrease in the surface temperature. However, all the components have been successfully manufactured without a noticeable increase in the recorded maximum load during the process manufacturing (Table 3.5).

Table 3.5 – Registered peak loads for each manufacturing conditions.

Max. load 1st trial	Max. load 2nd trial	Max. load 3rd trial
302,7 t	298,8 t	305,3 t

3.4.3.2. S48C

The S48C steel grade, also known as 1.1191 or CK45, is a quenching and tempering medium carbon steel grade commonly used in automotive industry for axles, gears and differentials manufacturing. The material was supplied by SIDENOR in round bars after hot rolling. In the following table (Table 3.6) the steel composition is shown.

Table 3.6 – Chemical composition of the S48C steel grade.

C	Mn	Si	P	S	Cr	Ni	Cu
0.48	0.82	0.27	0.019	0.024	0.16	0.15	0.21

In this case, the objective lies in observing if, at the same conditions, a geometry of higher complexity can be manufactured. This material is very similar to the C45, therefore the temperatures recorded for this material will be used as a reference here (Figure 3.3 (b)). Hence, after performing the complete heating cycle, which means temperatures close to 1360°C, two manufacturing trials have been performed, one with each geometry. In both cases, the material has been capable of successfully filling the geometries (Figure 3.9). However, opposite to what it was expected, the recorded maximum load was lower for the more complex case (H spindle) (Table 3.7).

(a) **(b)**

Figure 3.9 – SSF components with the S48C steel grade for (a) R and (b) H spindle geometries.

Table 3.7 – Registered peak loads for each manufacturing conditions.

Max. load R geometry	Max. load H geometry
306.7 t	271.5 t

3.4.4. Medium carbon 44MnSiVS6 microalloyed steel

Microalloyed steels are alloys composed by many different elements in small quantities (like Nb, V, Zr, Ti…) that give to the material different properties. This kind of alloys situates between mild and low alloy steels in terms of performance and cost. As a consequence of their chemical composition, they can be designed to have great strengths (more than 1000 MPa) and the possibility of attaining same mechanical properties as quenching and tempering steels by controlling the cooling in hot working conditions.

Regarding the selected 44MnSiVS6 steel, also known as 46MnVS6 or 1.5233, it is, in fact, one of the most resistant of this family of alloys. The material was supplied by SIDENOR in cylindrical bars after hot rolling. In the following tables (Table 3.8Table 3.9), the chemical composition and mechanical properties of this steel are shown.

Table 3.8 – Chemical composition of the 44MnSiVS6 microalloyed steel

C	Mn	Si	P	S	Cr	Ni	Mo	V	Ti
0.45	1.21	0.89	0.007	0.029	0.10	0.08	0.014	0.27	0.013

Table 3.9 – Mechanical properties of the as supplied 44MnSiVS6 steel

Rm (MPa)	Re (MPa)	A (%)	Z (%)
1051	738	14	22

The challenge of this material is twofold. First, to see if the microalloying elements added to this material can have a noticeable influence on the process and if the obtained microstructure in the SSF component is the aimed one to avoid the post-processing heat treatment. To observe that, a component has been manufactured with the R spindle geometry.

The heating has been carried out using the same cycle as in previous cases (Figure 3.3 (b)). It is true that due to composition differences, the temperature of the material might be slightly different after the same heating cycle due to the fact that electrical and thermal conductivities of the materials are not the same. However, this alloy still has a similar carbon content to previous ones, which means that the melting temperature would be similar and, therefore, they will be at more or less the same conditions.

In an attempt to take the higher advantage of the test, the process has been performed in such a way that the component is ejected as fast as possible. This comes from the capacity of the material to ensure great mechanical properties if ferrite-pearlite microstructure is obtained. Consequently, after the dies opening and part ejection, the component has been let to air cool to avoid high cooling rates that could lead to bainite or martensite generation.

The component has been successfully manufactured recording a peak load of 275.2t, similar to the maximum loads recorded with previous materials. This means that the added alloying elements do not have a huge influence on the deformation behaviour at these conditions as the load has not increased either decreased. However, due to the resolution of the system of the press to record the load, only major deformation changes can be noticed.

In addition, after analysing the microstructure of the component, the desired ferrite-pearlite microstructure has been observed (Figure 3.10). In the axle zone

(Figure 3.10 (a)), ferrite Widmanstatten can be appreciated. This comes from a slightly rapid cooling. In the rest of the component, the proper ferrite-pearlite microstructure is obtained.

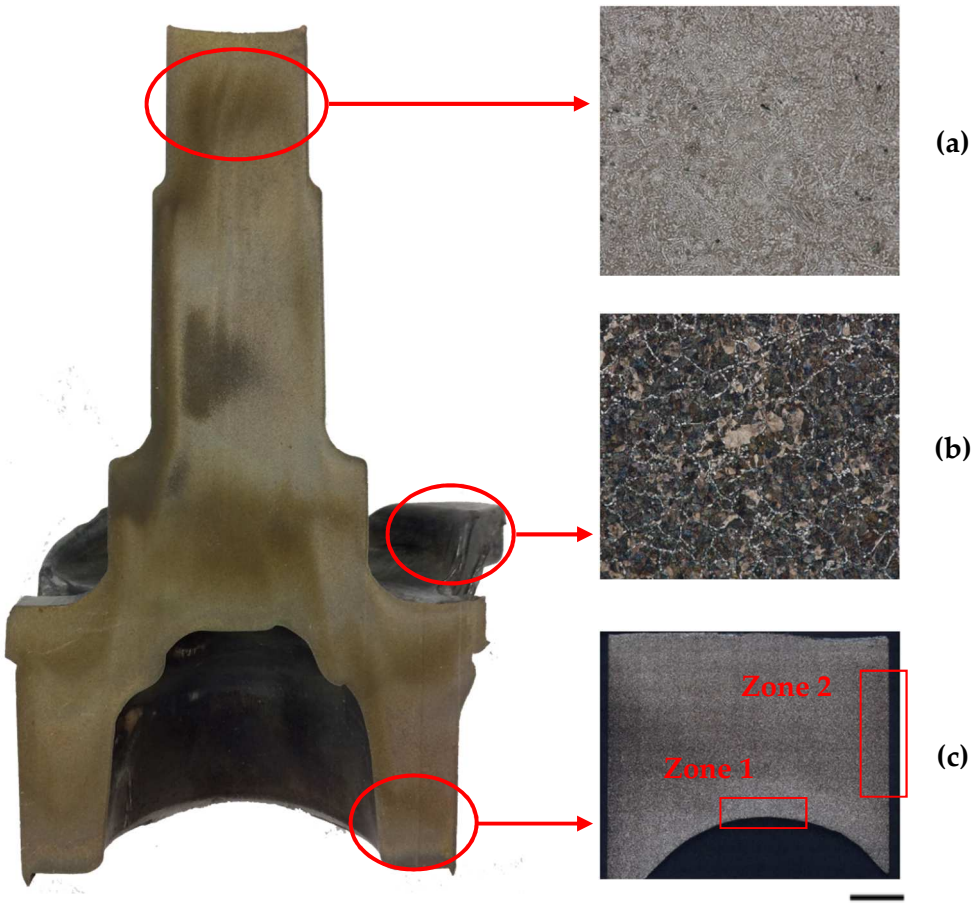

Figure 3.10 – The manufactured SSF component of 44MnSiVS6 cut in half and the microstructures at different positions: (a) axle, (b) middle and (c) bottom. The scale bar means 100μm for (a) and (b) and 5 mm for (c).

The difference between zone 1 and 2 of Figure 3.10 (c) is the grain size. In the zone 1, grains of the order of 22μm are noticed whereas in the zone 2 grains of close to 100μm are created. This comes from the strain differences between the distinct sections of the material. In those areas where the material has been in contact with the punch or the die (zone 1), higher deformations have occurred. When moving away from the surface, a lower degree of deformation have happened and, therefore, thicker grains are generated (zone 2). Note that Figure 3.10 (c) is a cut of the bottom part of the component in the perpendicular to the axle direction.

3.5. Concluding remarks

In this chapter, how the components are made and the gathered results when SSF several steel grades are presented. The obtained results do not do more than opening the possibilities instead of reducing them.

42CrMo4E

The results from 42CrMo4E show that the temperature parameter does not seem to be so critical as temperatures of around 100°C below the solidus have been used to successfully manufacture components. Moreover, the load has not increased, which could mean that even lower temperatures can be used.

S48C

The information obtained from the experiments with S48C suggests that the amount of material or the geometry has a strong influence on reducing the force required to completely fill the geometry. This conclusion comes from the successful filling of the higher complexity but less weighted H geometry with lower load recordings than the ones for the R spindle.

44MnSiV6

The capability of deforming the 44MnSiVS6 at same conditions exhibit that minor alloying elements do not seem to have a strong influence on letting the material or not to deform and fill the mould, even if they can have had a minor influence on it. Moreover, it opens the possibility of increasing the effectiveness of the process as the steels designed to avoid heat treatments can be utilised.

Observing the results attained with the three alloys, one must consider that many factors that were not controlled may have had influence. However, their influence does not seem to be the reason for the specific flow behaviour the material is exhibiting. Therefore, a phenomenon or group of them that is common for all these studied materials could be a reasonable explanation. In this case, some hypothesis regarding the generation of the observed material softening will be presented in the following lines.

Softening phenomena

There are several options that might explain what is happening to the material. The material could have a severe softening at working temperatures that enable the observed filling even whilst being in the solid state. This suggestion does not seem to be the most probable one as the generated backwards flash

through the remaining space between die and punch (around 0.3 mm thick) suggests that liquid should have been created (Figure 3.11).

(a) **(b)**

Figure 3.11 – Generated flash through the space between dies and punch (a) without and (b) with the installation of a copper ring.

Incipient melting

In the forging industry, the material at these working temperatures is considered useless. For most carbon and alloy steels, temperatures above 1250°C are avoided as the "Overheating" phenomenon happens. A step beyond such temperatures, the grain boundaries are oxidised and an incipient melting of lower melting constituents in the steel occurs. This is known as "Burning" and, according to forging industry, it is irreversible, which means that the material is considered as rejection [54]. Consequently, there is evidence of having small amounts of liquid at lower temperatures than the solidus. Not only in forging industry but also in casting it is observed a primary melting of grain boundaries that have been associated with cracks creation [55,56].

The influence of sulphur

Regarding this last phenomenon, the sulphur seems to have great influence on softening the material by making the material more brittle or even generating this incipient melting at those conditions [57]. If we observe the composition of the tested materials, one can observe that all of them have high sulphur contents.

Therefore, if S content is related with the generation of liquid below the solidus or generating a remarkable softening and the materials actually have a high amount of it, its potential effect cannot be neglected.

Adiabatic heating

Another considered phenomenon is the so-called adiabatic heating. It means a sudden plastic deformation of the material that is capable of releasing heat. This could also explain that even not having liquid through the material after heating, it is generated afterwards in the severely strained zones (for example, the flash zone) as a consequence of the sudden increment of temperature. This hypothesis seems also to be reasonable as the extrusion type deformation implies the generation of large strains.

Non-equilibrium liquid generation

Last but not least, the generation of non-equilibrium liquid could also be a possibility. This may be something uncommon, but if the equilibrium conditions are severely affected, the material behaviour changes. It has been experimentally shown in a fast differential scanning calorimetry how a non-equilibrium liquid was generated prior to a solid-solid phase transformation just by heating the material at very fast rates [58]. The same effect has not been experimentally analysed for a combination of temperature, pressure and deformation conditions, but some theoretical works suggest that this phenomenon could happen [59,60]. However, the analysis of this hypothesis seems to be difficult with the equipment we actually have and, therefore, it won't be considered for the moment.

Summary of the chapter

This chapter has been devoted to explaining the SSF cell equipment and operation. In addition, first manufacturing tests with different steels have been performed for different goals using the alloys 42CrMo4E, S48C and 44MnSiVS6. All of them have been properly manufactured even if different temperatures or more complex geometries were utilised.

The 42CrMo4E steel grade has been properly fabricated at temperatures close to 1300°C. The S48C has been used to successfully manufacture a component of higher complexity registering a lower peak load during the process. Lastly, the 44MnSiVS6 has been as well manufactured attaining a microstructure that can avoid the post-processing heat treatment.

The obtained results did not do more than increase the guess of having a phenomenon or group of them that enable the observed soft behaviour while maintaining the great properties. In the following chapter, the feasibility of the previous hypotheses will be analysed.

Chapter 4

SOFTENING PHENOMENA

"For every fact there is an infinity of hypotheses. The more you look the more you see"

Robert Pirsig

Summary

The SSF manufacturing process shows an unexpected material behaviour at the studied conditions. It is hard to guess why it behaves as it does and even more to understand it. However, there are some first signs during component manufacturing that open the discussion about what could be going on. Those will indeed be the starting point of this chapter.

This chapter will be devoted to analysing the incipient melting phenomena, the influence of sulphur and the adiabatic heating during the SSF process. The obtained results will show how nor the incipient melting neither the influence of sulphur is the reason for the material softening. The capability of increasing the temperature during deformation at near solidus temperatures will be confirmed but still, further investigations have to be performed to establish the adiabatic heating as the driving phenomenon during SSF.

4.1. Introduction

The SSF of steels is continuously giving surprises. What initially was thought to be impossible, it has actually become a reality. Indeed, these specific findings are at the same time encouraging and disconcerting. In the very beginning, solid fractions above 90% according to DSC were prohibited as the material stopped behaving as a semi-solid. At that time the design was clear. Even if this was hard to model, the reason for the ease of cavity filling was known. However, no competitive components were capable of being manufactured.

Sound components were attained at temperatures below the solidus temperature measured by DSC by close to 100°C. This fact implies a new stage in terms of understanding what happens in the material as, theoretically, there is no liquid enabling this semi-solid behaviour. To complicate matters even further, the previously pointed findings create even more uncertainties as components at lower temperatures and materials that were not supposed to deform were successfully manufactured.

At this point, one can hardly see a close similarity between the conventional SSF and the actual procedure in MGEP. Therefore, in an attempt to shed light on what could be going on in the material, other aspects that were not considered in the conventional SSF will be analysed. As it can be guessed from the previous section, this chapter will analyse three different phenomena: the incipient melting phenomena, the influence of sulphur and the effect of adiabatic heating. The utilised materials in this section are exhibited (Figure 4.1).

The steel grade selected for the analysis of the incipient melting phenomena is the 42CrMo4E. This steel grade has been proved to be capable of being subjected to the SSF attaining no defects and great mechanical properties. Moreover, in the previous chapter it has been observed how at even lower temperatures than 1360°C, components are properly manufactured. Therefore, this is the best material to start with analysing the possible phenomena. Consequently, the influence of sulphur has also been analysed by using this steel grade in its low (L), medium (E) and high (H) sulphur version.

Lastly, to analyse the influence of adiabatic heating, the use of this steel grade was inappropriate as no post-mortem analysis was possible. Hence, an austenitic steel that does not have any phase transformation between the working and room conditions has been selected. In this case, the Invar 36 has been utilised as its low quantity of alloying elements could make easier the microstructural analysis.

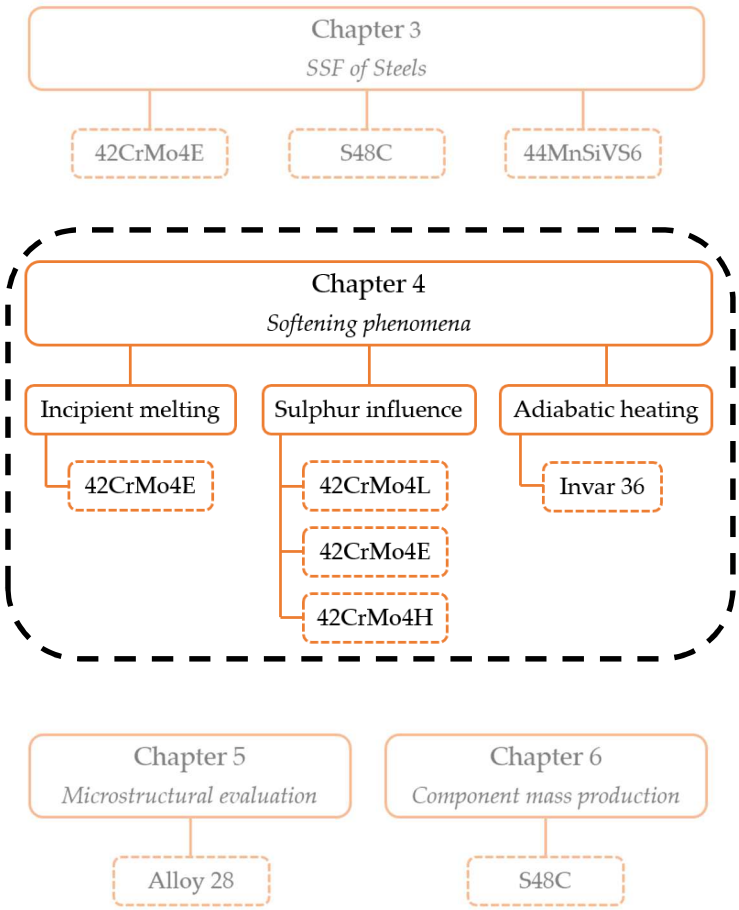

Figure 4.1 – Selected steels for the experimental procedure of the Chapter 4.

4.2. Incipient Melting Phenomena

4.2.1. Brief literature survey

One of the considered phenomena is the so-called "incipient melting", also known as "liquation". As mentioned before, this phenomenon has been widely investigated in continuous casting processes as it is related to crack appearing [55,56]. It consists of the melting of grain boundaries at temperatures below the theoretical solidus. Its appearing depends on the solute or residual elements segregation at grain boundaries [56]. Thus, the elements' distribution through the material impacts directly on how and when this phenomenon appears. Note that "liquation" is generally attributed to solidification processes and, consequently, the temperatures related to the boundary melting will be lower due to the required undercooling for solidification [61].

Watanabe and Okane [62] analysed this effect on Ni-Cr and Ni-Cr-Mo steel grades at different carbon contents. They observed that the initial stage of liquid creation happens mainly in the grain boundary triple points (Figure 4.2 (a)) and at the grain boundaries which intersect with a segregation band (Figure 4.2 (b)).

As they suggest, this comes from the movement of the grain boundaries as a consequence of the grain growth because of heating. This movement is prevented thanks to the segregation bands created during steel making. Therefore, these grain boundaries, including the triple points, are fixed in such bands. Based on this, when reaching temperatures below the solidus, these zones have an incipient melting due to a low melting point reaction like eutectic caused by the enrichment of segregated elements (in this case Ni, Cr and Mo) through grain boundary diffusion.

If the temperature increases, the diffusion of segregated elements becomes more active, increasing the alloying elements enrichment in the grain boundaries and, consequently, widening the liquated region (Figure 4.2 (c)). By a further rise in temperature, the melting occurs both in segregation bands and grain boundaries (Figure 4.2 (d)). At even higher temperatures, the whole sample melting begins (Figure 4.2 (e)).

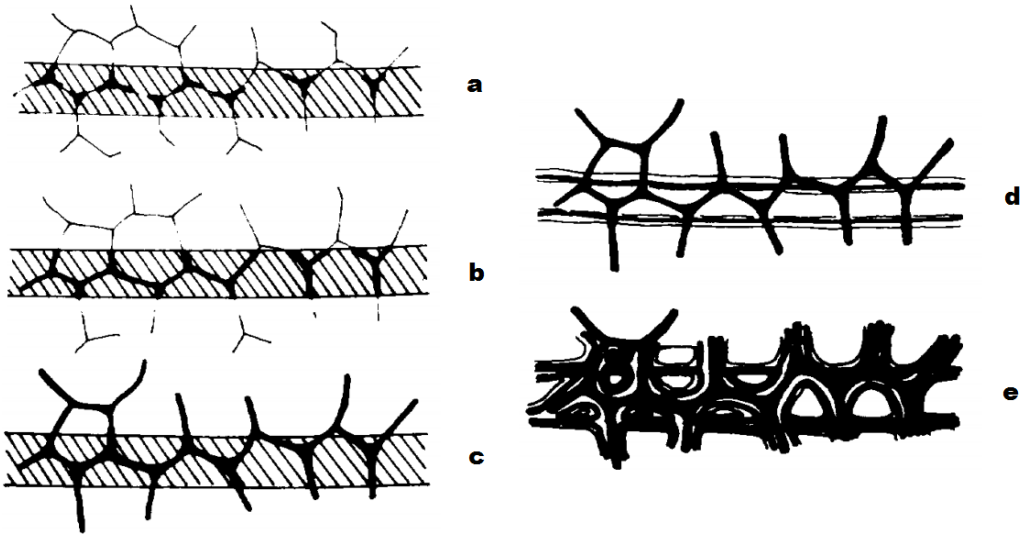

Figure 4.2 – Schematic illustration of the incipient melting phenomena at different stages. The hatched zone is the segregation band [62].

In their case, they observed that the segregated elements that allow the incipient grain boundary melting were Ni, Cr and Mo, being crucial the

coexistence of Ni with Cr and/or Mo. In the following figure (Figure 4.3), we can observe how the incipient melting changes with different heating speeds (rapid refers to 140°C/s and slow refers to 1°C/s) and carbon content for different steels.

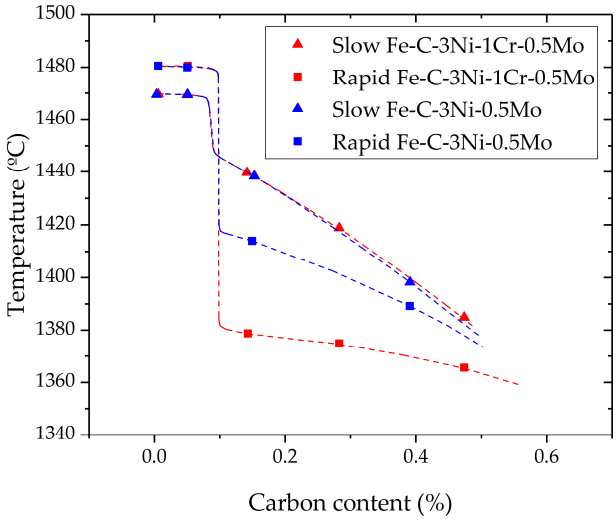

Figure 4.3 – Carbon content vs temperature at which the onset of liquation of grain boundary is observed [62].

Many researchers have also observed the incipient melting phenomenon [63–66]. Even under different names (Incipient Melting Temperature (IMT), Zero ductility temperature (ZDT), Nil ductility temperature (NDT) or ductile-brittle transition temperature ($T_{d/b}$)), there is a temperature associated with the appearing of liquid that softens the material. This limiting temperature is obtained during hot tensile tests. The recorded temperature when the specimen breaks off without any discernible necking is the temperature at which first small amounts of liquid is generated. Another parameter like Zero Strength Temperature (ZST), defined as the temperature where the material loses its strength, is also interesting as it is related to an even higher amount of liquid [61].

For the reasons mentioned above, it makes sense to think about the possibility of suffering the Incipient Melting phenomenon in our highly alloyed steel. In order to clarify whether this effect explains the softening we are observing in the material, several measurements have been carried out.

To begin with, it is necessary to define the theoretical temperature where the material starts to melt. It has been measured using a DSC equipment. Secondly, IMT and ZST temperatures have been obtained to compare the resulting temperatures with the theoretical melting one. In addition to those tensile tests,

compression tests have also been carried out to confirm if there is any behaviour modification on the strain-stress curves of the material at measured temperatures. At last, direct observation of the material during heating up in a High-Temperature Confocal Laser Scanning Microscope (HT-CLSM) has been performed to confirm all the previous experimental measurements.

4.2.2. Material

The material used for these experiments is the 42CrMo4E steel grade. Its composition and as-supplied state are explained in section 3.4.3.1. Its selection comes from the great results obtained in MGEP as the first SSF components attaining not only energy and material saving but also as forged mechanical properties were manufactured with this steel.

4.2.3. Differential Scanning Calorimetry (DSC)

This thermal analysis technique has been used traditionally to measure weight fraction of solid [67]. This process consists of three steps: the measurement of the heat of melting, the calculation of weight fraction of solid using the method of partial areas and these last results are transformed to the volume fraction of solid [68].

4.2.3.1. Technique

In this method, small samples (around 100 mg) are heated up at rates between 5-20°K/min from a temperature where the material is completely solid (usually 30°C under the solidus temperature) to a temperature above liquidus. Then, the differential power flow rate is obtained. It is essential to control the temperature and compare it with that of the reference sample when heated at a constant heating rate.

To transform the DSC output enthalpy change curve (Figure 4.4 (a)) to liquid volume generation against temperature, the partial areas method is employed. It refers to the calculation of the whole area under the peak enthalpy-area curve to determine the melting enthalpy of the material. The peak characteristics are [68,69]:

- The changes of slope, jumps and peaks showing the thermal events
- The peak area is the enthalpy variation of the transformation
- The specific heat is calculated from the baseline

- Solidus-liquidus interval: T end of melting - T beginning of melting (T_f - T_o)

The liquid fraction is proportional to the absorbed energy during the transformation. The sample is heated until total melting. Therefore, the liquid fraction can be calculated considering the peak area of the transformation, as shown in Figure 4.4 (b).

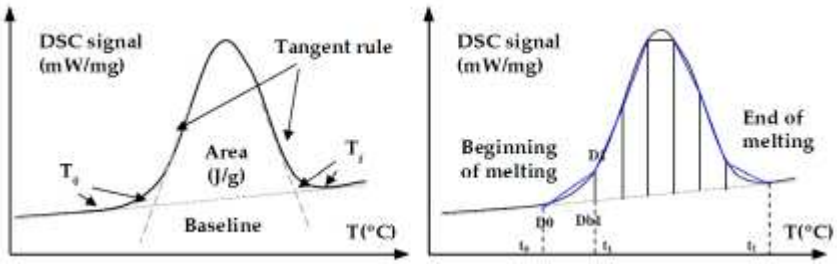

(a) **(b)**

Figure 4.4 – Melting peak features (a) and determination of the liquid fraction (b) [68].

4.2.3.2. Drawbacks

The major challenge here is to achieve exact values from the method of partial areas. As the temperature increases, the composition of the solid phase changes to maintain local equilibrium at the solid-liquid interface following the equilibrium phase diagram. Moreover, the heat of melting, the parameter that gives the information about the required energy by the atoms to be transferred from solid phase to the liquid across the solid-liquid interface, is also dependant on composition as it is in function of the type of atoms, their concentration and their spatial distribution.

According to this, it is shown that when the heat of melting of the alloy is significantly different from the latent heat of the solvent metal (when the alloy is not dilute), this method of partial areas exhibits a significant error. In other words, it means that the partial areas method assumes the material as a unique system that melts homogeneously. It does not consider segregation phenomena that could modify the melting behaviour and, as a consequence, the solid-liquid volume transformation curve may have a different shape in comparison with the real melting.

Furthermore, it is hard to define the equipment resolution in terms of first phase transformation detection. It means that the first drop in the curve may not imply the initiation of melting, but it could be related to the detection of a certain amount of liquid. Besides, it is difficult to accurately identify the melting initiation and ending temperature from the resultant curve. In addition, it is very difficult to

ensure the real solidus and liquidus temperatures. How to set those temperatures (selected as the initial and final point to calculate the peak enthalpy area) and how to calculate the area inside the curve is quite open to personal appreciation. This could also imply an error on the real evolution of the liquid against temperature.

Another aspect to take into consideration is that this technique utilises near-equilibrium conditions. It uses heating rates in a range of 5 to 20°K/min, which differs from the industrial reality, where those are at least of the order of 170°K/min. In addition, the material temperature must be homogeneous for thermal analysis. It means that the obtained solid vs liquid fraction curves do not simulate accurately industrial conditions as they can achieve neither those high heating rates nor a similar temperature distribution through the sample.

Despite these drawbacks, this technique is still the best to estimate the temperature at which the material seems to start and end to melt. It easily gives a great reference point to start designing experiments with other techniques to find other specific temperatures.

4.2.3.3. Results

So as to achieve the liquid fraction curves, DSC experiments have been carried out in the NETZSCH model STA 449 F3 Jupiter® simultaneous thermal analyser that is capable of reaching maximum temperatures of 1650°C (Figure 4.5 (a)). The experimental sequence consists on heating a sample of 100 mg at a rate of 20-50°K/min up to 1100°C and, then, on heating it up at a rate of 10 °K/min until 1550°C. This segmentation is made so as to ensure good sample temperature homogeneity and to avoid damaging the equipment.

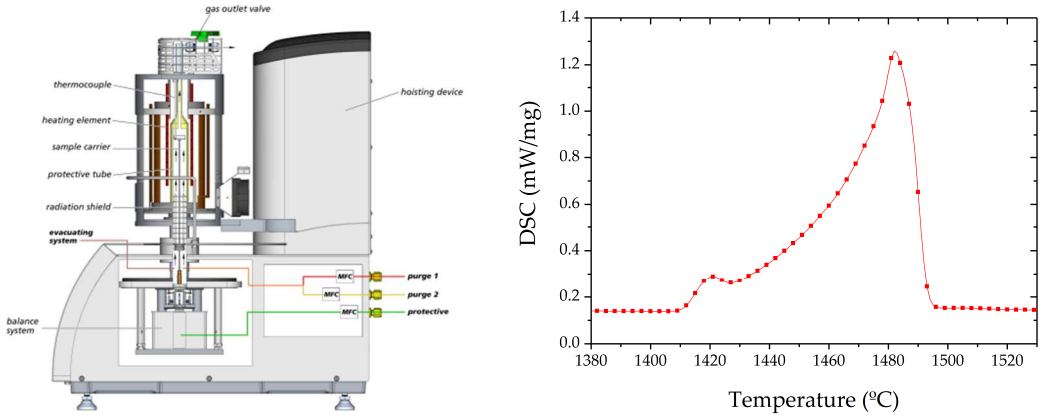

(a) **(b)**

Figure 4.5 – (a) Schematic illustration of the NETZSCH STA 449 F3 Jupiter® equipment and (b) DSC signal outcome for 42CrMo4E steel grade.

The power flow rate against temperature curve during the melting of 42CrMo4E steel grade is shown in Figure 4.5 (b). According to this data, the transformation seems to happen in the following order: $\gamma \rightarrow \gamma+L \rightarrow \delta+L \rightarrow L$. From this data, and using the partial areas method, the liquid fraction against temperature curve can be obtained.

First of all, it must be decided how to limit the curve inner area. There are many baseline options depending on the curve shape (straight line, curved line…). In this case, and making it clear that this selection is completely subjective, it has been decided to use a straight line from the defined solidus to liquidus temperatures. The selected solidus and liquidus temperatures are 1408°C and 1496°C respectively. Then, the area is calculated by using the Newton-Cotes approximation and transformed to liquid volume percentage. The following is the obtained curve (Figure 4.6):

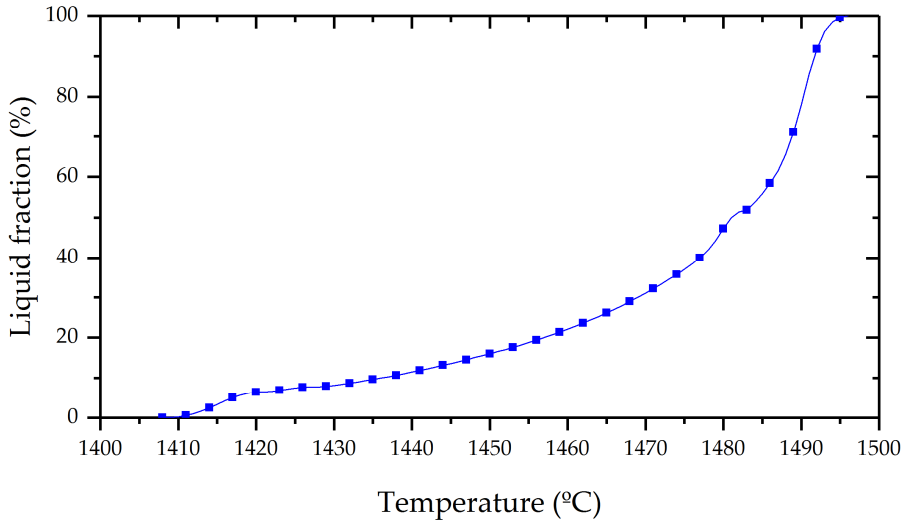

Figure 4.6 – DSC liquid fraction vs temperature curve of 42CrMo4E Steel grade.

4.2.4. IMT and ZST measurements

As mentioned before, the incipient melting phenomenon was considered to be the responsible for metal cracking during continuous casting. The ductility of the material at such a state is directly related to corner and face cracking, internal tears, etc. [55]. Thus, great efforts were made focused on characterizing the behaviour of the ductility in the materials at different temperatures with the aim of observing any influential information.

During the performance of hot tensile tests, a temperature where a drop in ductility happened was observed. After microstructural analysis, it was concluded that the creation of a thin liquid film was the responsible for such ductility loss [70]. From then on, the hot tensile test technique has been the most used one to detect the temperature at which the first liquid film appearing is guessed [61,64–66].

4.2.4.1. Equipment

This technique is based on the deformation of a sample heated to a certain temperature at a selected strain rate. Normally, due to the ease of test performance and post-mortem microstructure analysis, tensile tests are selected for this task. This kind of experiment requires heating and deformation equipment. It is similar in essence the use of a Gleeble equipment or a mechanical testing equipment with an external induction or resistive unit. In any case, the sample must be heated in situ to avoid heat loses that difficult the temperature estimation.

In this case, it has been utilized the Gleeble 3800C thermomechanical equipment of SIDENOR I+D to perform such tests (Figure 4.7). This equipment is capable of performing tensile tests until 10t and compression tests until 20t. The maximum speed the equipment can get is 2 m/s. The heating system is based on Joule effect, which is capable of achieving temperatures higher than steel melting point.

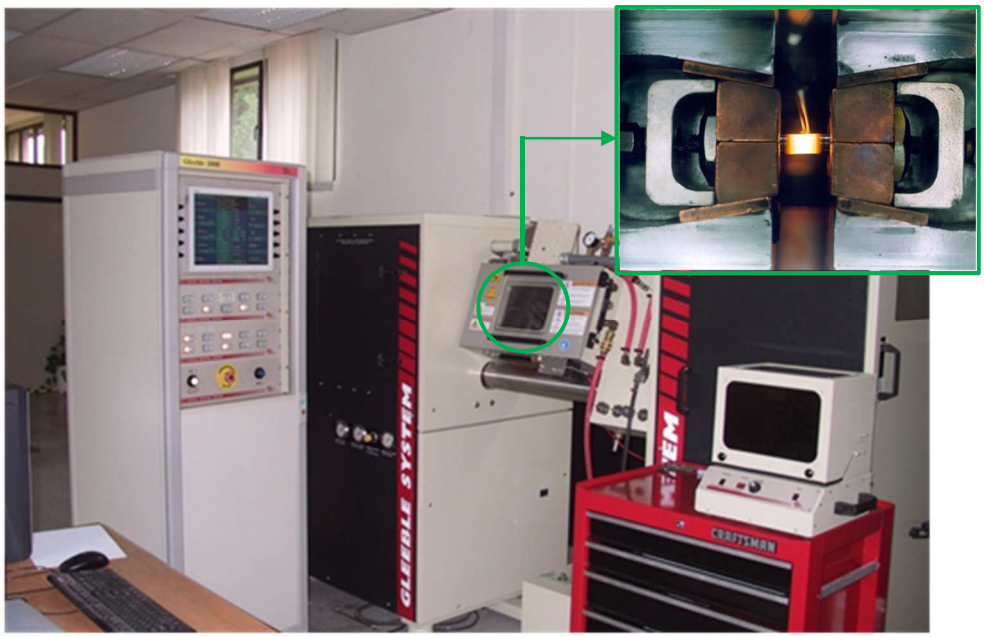

Figure 4.7 – Gleeble 3800C thermomechanical equipment of SIDENOR I+D.

The main advantage is the Joule effect heating system. It enables fast heating and a constant control of temperature during the process, avoiding any temperature rise caused by adiabatic heating as the temperature control works in a closed loop. As a result, we can maintain the same temperature during the deformation. However, as this temperature regulation requires time, at very fast strain rates the adiabatic heating may have influence.

4.2.4.2. Experimental set up

The experimental set up to obtain the IMT and ZST consists of heating the sample up to several defined temperatures. Then, once the sample has reached the working temperature and has been homogenized during a couple of seconds, a tensile stress is applied to observe the cross section in the case of IMT and the deformation force in the case of ZDT. The recorded temperature at which the material breaks off without any discernible necking (cross-section reduction) is the IMT. Conversely, the temperature at which almost no force is required to fracture the sample is the ZST.

In the Gleeble equipment, the sample shape is standardized. In the case of tensile tests, the sample dimensions are shown in Figure 4.8 (a). The sample working zone is the central one. There, a couple of R-type thermocouples are welded to measure the temperature and to feed the closed loop heating control. In Figure 4.8 (b) the applied heating cycle and strain rate during each experiment can be observed.

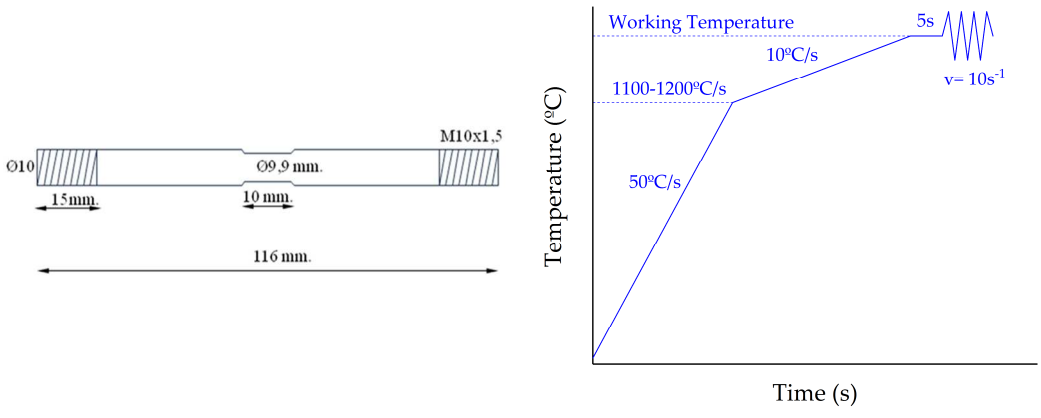

(a) **(b)**

Figure 4.8 – (a) Tensile test sample dimensions for Gleeble equipment and (b) used heating cycle and strain rate during each experiment.

4.2.4.3. Results

The measured IMT temperature for 42CrMo4E steel grade is 1380-1385°C. It has been performed the hot tensile tests at different temperatures until no necking is observed to record this temperature as IMT (Figure 4.9). In Figure 4.10 (a) the recorded deformation force during the experiment is shown.

(a) **(b)** **(c)**

Figure 4.9 – (a) Sample with huge necking; temperature great below IMT. (b) Sample with little necking; temperature near IMT. (c) Sample with no appreciable necking; IMT.

Regarding the ZST of 42CrMo4E, it is located between 1392-1394°C. The following figure shows the residual force recorded during the sample deformation at such temperatures (Figure 4.10 (b)).

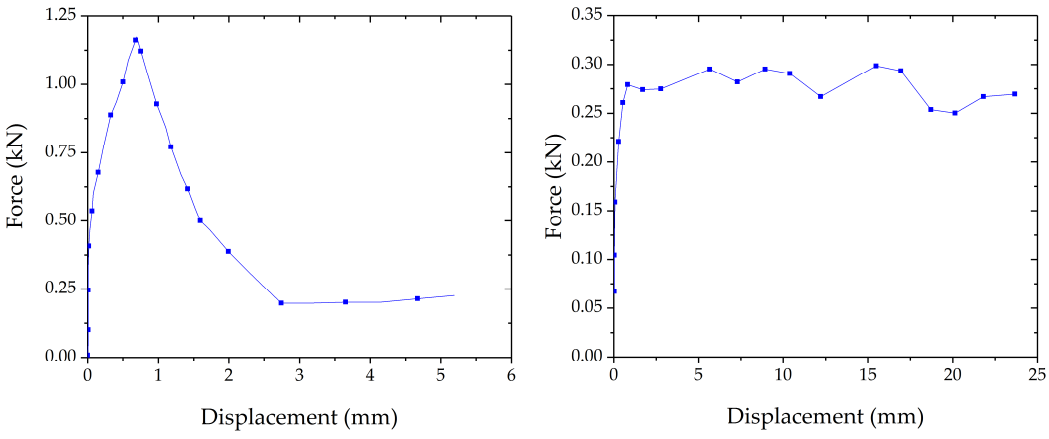

(a) **(b)**

Figure 4.10 – Recorded load against displacement during the hot tensile test at (a) IMT and (b) ZST.

According to previously referenced researchers, these results are in good agreement with the hypothesis of having liquid at temperatures below the theoretical solidus measured with the DSC equipment. The measured IMT is around 25°C lower than solidus, whereas the ZST has a difference of around 15°C. This means that there could be some alloying elements that melt under the conditions of the experiment, which are closer to the industrial reality than the DSC technique.

In addition, this hypothesis also argues the shape of the recorded force against displacement curves. The breakage of the sample without any discernible cross section reduction comes from the ease of the material to grain decohesion. It is easier for the material to have an intergranular fracture than grain deformation. This explains the peak in Figure 4.10 (a), which suggests that there is happening a micro-deformation until grains start to separate, as a consequence of the generated thin liquid film through the grain boundaries. At higher volumes of liquid, the force required to separate the grains from each other is residual, as the graph expresses the load for equipment claws movement (Figure 4.10 (b)).

4.2.5. Compression tests

This experimental procedure is widely applied for quality control and to study the deformation behaviour of many types of materials. Its capacity of achieving large strains makes this test a great choice to record material deformation information for subsequent modelling. In fact, it is often alleged that compression tests resemble closely the open die-forging operation. Moreover, this technique has been commonly used to analyse semi-solid materials at high-solid fractions [71–73].

The aim of this experiments lies on observing any kind of inflexion temperature where the material has a stress drop. Several conditions will be tested to observe whether the recorded turning temperature on material behaviour, if any, is similar to the measured temperatures during hot tensile tests (IMT and ZST) or not.

4.2.5.1. Equipment

A parallel-plate compression device mainly consists of a static and dynamic or both dynamic plates that provide the required speed and force to deform the material. In case of hot deformation experiments, as it has been pointed out in section 4.2.4.1, it is suggested to have an in-situ heating equipment to avoid unnecessary loses.

For this task, it has also been used the Gleeble 3800C thermomechanical equipment of SIDENOR I+D (Figure 4.7). In the same fashion as for hot tensile tests, it is also desired the avoidance of adiabatic heating. It is difficult as if it is generated, it will happen in localized sections at a very brief lapse of time. Therefore, the closed loop may not have enough time to balance it. In any case, this equipment is the most suitable for this task as it is designed to perform thermomechanical experiments.

4.2.5.2. Experimental set up

The experimental setup, in this case, differs from the tensile test as the sample geometry is different. In this instance, cylinders of 10 mm of diameter and 15 mm long are used. They are located between two horizontally arranged plates with tantalum and graphite foils in each side to avoid sticking. Two R-Type thermocouples are welded in the centre of the billet for a closed loop heating control. The following figure shows the experimental sequence (Figure 4.11).

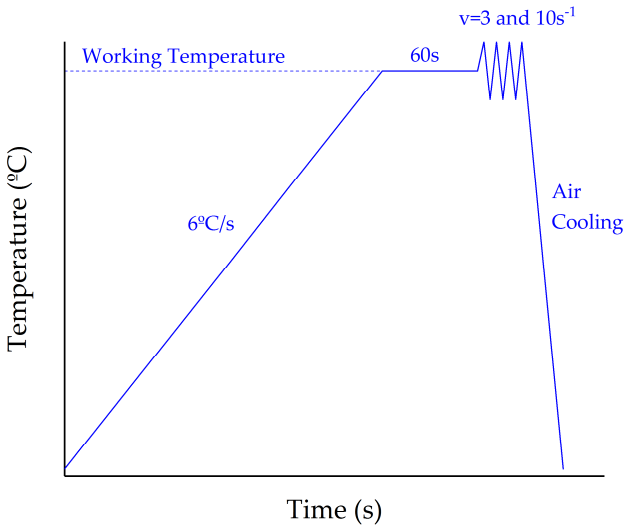

Figure 4.11 – Schematic illustration of the utilised experimental sequence for hot compression tests in Gleeble.

In order to have a relatively high window to observe a stress fall, temperatures between ZST and 60°C below the IMT have been tested. Therefore, compression tests are carried out each 10°C from 1320°C to 1400°C. The velocity and heating rate parameters have been selected considering the used manufacturing conditions of the SSF process. Consequently, a 6°C/s heating rate has been applied followed by a homogenisation stage. Then, deformation at 3 and $15s^{-1}$ strain rates is performed. The former is the initial strain rate when the punch gets in contact with

the billet. The latter is a higher value as thin sections in the mould increase the strain rate of the material during filling.

Due to the price of tantalum foils and R-type thermocouple wires, one experiment at every condition has been carried out. As the aim was to confirm the behaviour observed in hot tensile tests, the errors that could be observed are assumable. A second repeat was carried out in those cases where the welded thermocouple came off or the heating exhibited an error.

4.2.5.3. Results

The obtained curves for some conditions exhibited a great deviation presumably by a bad heating, which means that the real deformation temperature was not the correct one. Taking this into account, only the curves of which working temperature can be trusted have been considered. From the force against ram displacement data acquired from the Gleeble, the true stress and true strain information can be calculated. The true strain is calculated with the following equation where "h_o" means the initial height of the sample and "d" means the compressive displacement:

$$\varepsilon = \ln\left(\frac{h_0 - d}{h_0}\right) \quad \textbf{(1)}$$

The true stress (σ') is calculated considering the sample deformation. As the compression goes, the sample height is reduced, the section goes up and, therefore, the sample's contact surface with the plate increases. Due to the constant volume of the sample and assuming a negligible barrelling, the following equations (equations 2 and 3) enable the true stress calculation:

$$\sigma' = \frac{F}{\pi \frac{\emptyset_i{}^2}{4}} \quad \textbf{(2)}$$

$$\emptyset_i{}^2 = \frac{\emptyset_o{}^2 \cdot h_o}{(h_0 - d)} \quad \textbf{(3)}$$

where "F" is the recorded force and "$Ø_i$" and "$Ø_o$" are the modified and initial diameters respectively. The obtained true stress against strain curves are shown in Figure 4.12.

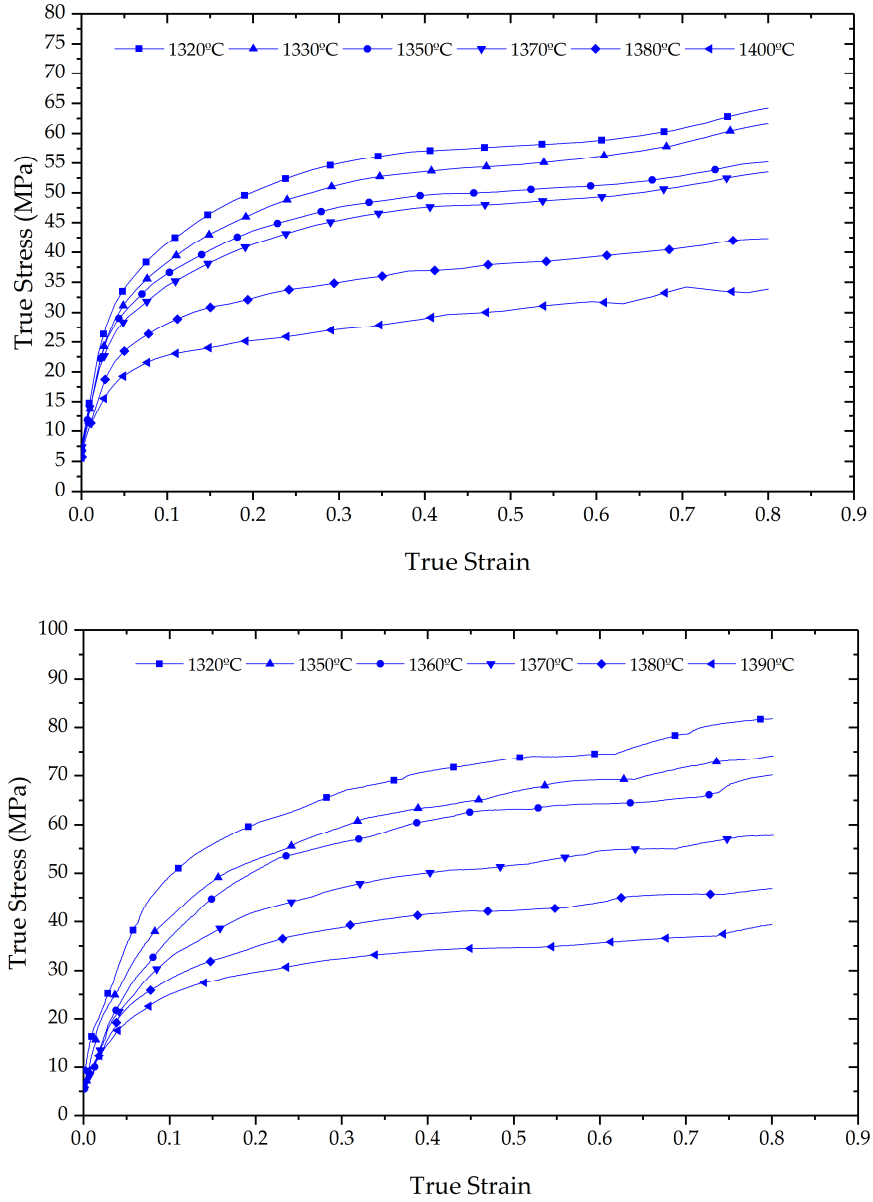

Figure 4.12 – True stress vs strain curves for different temperatures at (a) $3s^{-1}$ and (b) $15s^{-1}$ strain rates.

According to these results, it seems that at temperatures near 1380°C a fall in stress happens. In the case of $3s^{-1}$ strain rate, a fall from around 40MPa to near 25MPa respectively in the measured stress between 1370°C and 1380°C can be observed. In spite of being smaller, there is also a significant difference between 1380°C and 1400°C. The same is appreciated at the strain rate of $15s^{-1}$ where the stress fall seems to happen at a slightly lower temperature, in between 1370°C and 1380°C.

The recorded temperatures are in accordance with the previously measured IMT. Consequently, the compression results may as well be explained due to the

appearance of an intergranular liquid film that permits a softer deformation. At higher temperatures, a higher volume of liquid might be created enabling an even less resistant deformation. In the following figure the deformed samples are shown (Figure 4.13):

Figure 4.13 – Samples shape after the compression at different temperatures at $3s^{-1}$.

It can be noticed how the grain decohesion starts to be severe at temperatures near those where a fall in stress is observed. Assuming that a thin intergranular liquid film may exist, this crack generation could be generated due to the granular behaviour of the material. As there is not enough liquid to fill the created spaces, cracks appear (see section 2.5.2).

There are also samples at lower temperatures where some cracking is observed (Figure 4.14). It could mean that we could have a localised melting in some specific zones where a high concentration of lower melting constituents exists. However, other reasons like the creation of a very fragile grain boundary phase also make sense.

(a) **(b)**

Figure 4.14 – Pictures of deformed samples at 1340°C and (a) $3s^{-1}$ and (b) $15s^{-1}$. The hatched zones show the created cracks.

4.2.6. High Temperature Confocal Laser Scanning Microscopy (HT-CLSM)

The HT-CLSM method permits the performance of high temperature in situ 2D microstructure evolution analysis of metals. The use of a laser beam enables the distinction of phases at high temperatures in spite of the glow as it gives higher illumination intensity than the thermal radiation. The latter in combination with the confocal optics permits to clearly distinct phases and image the sample surface during phase transitions, melting and solidification. Therefore, since this technique was developed [74], many researchers took advantage of it to analyse the material microstructure during cooling [75–78] and heating [79,80].

The goal of this experiment lies in observing the microstructural evolution during heating at higher heating rates than in DSC and compare both results. This information is required to in-situ observe what is happening inside the material during the heating process. To do so an experimental routine similar to the one proposed by Hechu et al [81] will be followed.

4.2.6.1. Equipment

The utilised HT-CLSM equipment is the Yonekura V2000DX-SVF17SP model of the Steel Processing Research Group of the University of Warwick (Figure 4.15 (a)).

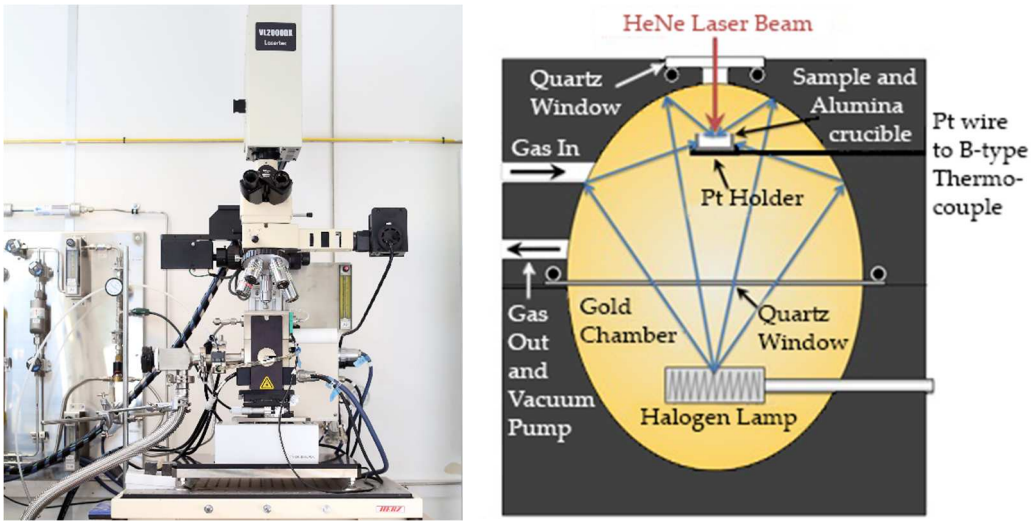

(a) **(b)**

Figure 4.15 – (a) Yonekura V2000DX-SVF17SP model HT-CLSM and (b) schematic illustration of the high temperature furnace [82].

It consists of a confocal scanning laser microscope with an ellipsoid-shaped gold chamber where the sample is heated under an inert atmosphere. The upper quartz window permits to look at the sample during heating and cooling. The lower separates the infrared heating stage from the testing zone to enable the creation of the desired experimental atmosphere.

The heating is carried out by a 1.5kW cylindrical halogen lamp that heats the sample with direct and reflected light (Figure 4.15 (b)). It has a platinum sample holder with two B-type thermocouples measuring the temperature of the centre of the crucible that feeds the external closed-loop heating control. The equipment is capable of heating the sample from ambient to 1600°C in 30 s and a rapid cooling of as much as 100°C/s using high pressure He gas.

4.2.6.2. Experimental set up

The sample dimensions for this equipment are comparable to those for DSC. They are cylindrical samples of 3mm of diameter and 1mm thick. The cut faces must be as parallel as possible to avoid imaging problems and to ensure the contact between the sample and crucible so as to minimise the error of the recorded temperature. In addition, the upper surface must be polished for microstructural observation. The following is the used heating cycle (Figure 4.16):

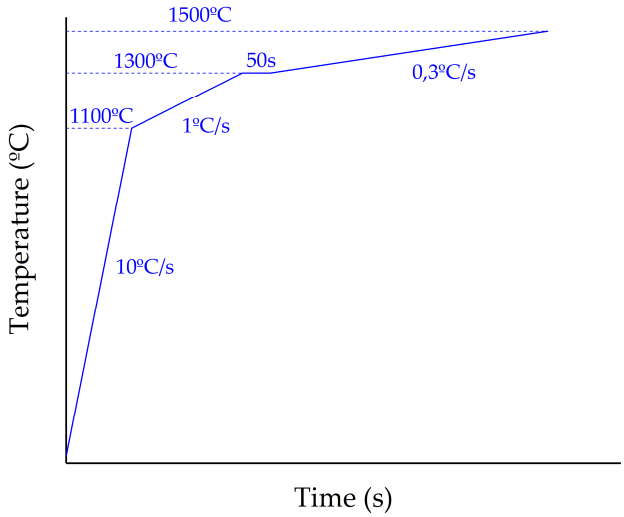

Figure 4.16 – Schematic illustration of the utilised experimental sequence for the high temperature microstructural evaluation in the HT-CLSM equipment.

An initial fast heating rate is applied until 1100°C. Then, to heat it up until 1300°C more homogeneously, a rate of 1°C/s is used. After that, a homogenisation stage of 50 seconds has been set in order to homogenise the temperature through the sample and to properly focus the microscope for the subsequent observation. Lastly, a slow heating velocity up to 1500°C to record all the phenomena during the melting of the steel is applied.

4.2.6.3. Results

Some of the images obtained during the experiment are shown in Figure 4.17. At the temperature at which the components are made (1360ºC) the austenitic microstructure can be clearly observed (Figure 4.17 (a)). While the temperature is increased, the austenite grain boundaries start moving leading to grain growth (Figure 4.17 (b)). The very first liquid phase has been observed at 1455ºC (Figure 4.17 (c)) ($\gamma \rightarrow \gamma + L$). The liquid generation started in the grain boundary triple points, increasing its amount through the grain boundaries and partial melting some grains.

At 1470°C the remaining austenite transforms to δ-ferrite (Figure 4.17 (d)) at the same time that the liquid generation continues (Figure 4.17 (e)) ($\gamma + L \rightarrow \delta + L$). Finally, at 1500°C the whole sample melting happened (the melting temperature was reached: $\delta + L \rightarrow L$) (Figure 4.17 (f)).

Looking at those results, the phase transitions guessed looking at the DSC curves are confirmed. It is true that the temperatures are different, however, it is likely to be due to the uncertainties the confocal equipment has to properly measure the real temperature. Consequently, as the DSC measurement is more precise in this aspect, those registered temperatures will be assumed as solidus and liquidus ones. In any case, note that the first observed liquid was recorded in a very small zone of the whole sample. This means that some liquid and/or δ-phase may have been generated previously in other zones of the sample at lower temperatures.

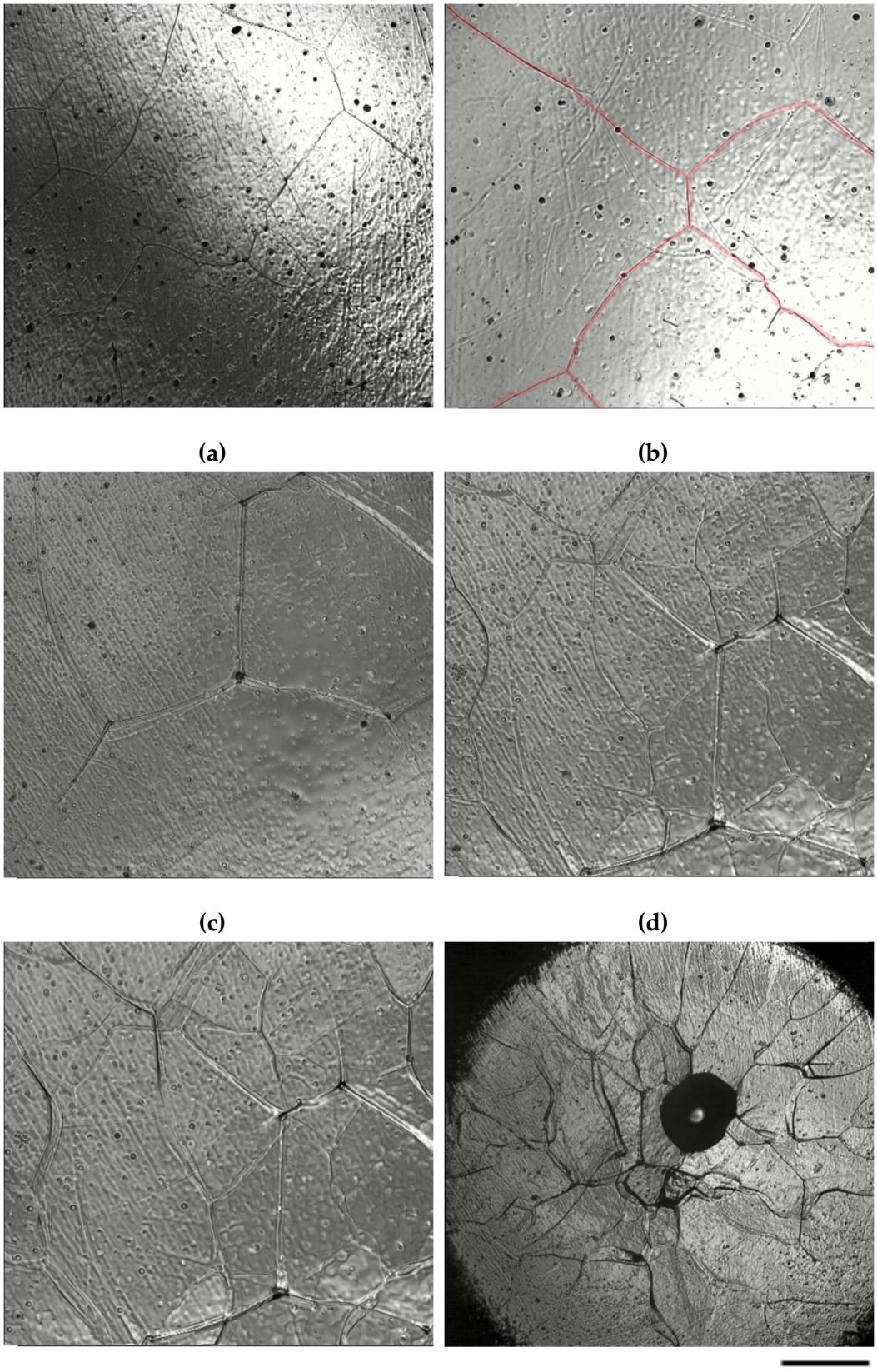

Figure 4.17 – Images taken with the HT-CLSM at (a) 1360°C, (b) 1405°C, (c) 1455°C, (d) 1470°C, (e) 1490°C and (f) 1500°C. The bar distance means 200μm in (a-e) and 510μm in (f).

4.2.7. Conclusions

The initial guess of having liquid due to uniquely thermal effects has been proved to do not happen in the studied steel grade as this material does not exhibit any signs of incipient melting. The reason could be the material thermal history. As the material comes after a quenching and tempering treatment, the alloying elements seem to have been homogeneously dissolved in the matrix. Therefore, they should be stable and properly distributed through the material. As a result, the material would exhibit low segregation which implies an almost inexistent incipient melting phenomenon.

Nevertheless, the tensile tests showed the capability of the material to break both without any discernible elongation and without putting up any resistance. These two phenomena are related to the liquid appearance in the literature (see section 4.2.1). However, at least in purely thermal conditions, it has been proved the inexistence of it until higher temperatures. Therefore, it seems it could happen due to a soft or really fragile grain boundary that enables the grain decohesion. It could also be possible to have a combination of temperature and deformation that could generate small amounts of liquid.

The compression tests result also suggests this lasts hypothesis. At temperatures close to IMT and ZST the material strength drops and grain decohesion is observed in the deformed samples. However, even at lower temperatures than those, some cracks are also visible in the surface, which means that the intergranular cracking is possible at even lower temperatures.

One of the elements that have been proved to have a huge influence on material embrittlement at high temperatures is the Sulphur and, indeed, all the studied steels have a great amount of it (see section 3.4.2). Therefore, the following section will be devoted to analysing its influence on the material microstructure and behaviour.

4.3. The Influence of Sulphur

The previously mentioned “Overheating” and “Burning” phenomena have been related to the presence of sulphur [57]. The latter, as defined by Edward G. Nisbett [54], implies the oxidation of grain boundaries and incipient melting of lower constituents in the steel. The temperature where this phenomenon occurs has been identified at 1355°C for many carbon and alloy steels, although it could happen at lower temperatures in function of time and segregation.

The reason for sulphur to have an influence on "Burning" is due to its ease to segregate to the grain boundaries at high temperatures. Many works relate the embrittlement of the material at hot deformation conditions with the segregation of this element to the grain boundaries [83–85]. In addition, the sulphur impacts on decreasing the melting temperature and widening the semi-solid interval of the materials. Taking advantage of this effect, some off-the-shelf materials have been adequate to the conventional SSF [86].

Therefore, at the studied conditions, a higher amount of sulphur concentration in the austenite grain boundaries that could lead to material embrittlement or liquid generation should be expected. Indeed, this effect has been shown by Hee Yu et al [87] and Zabil'skii and Nikonova [64] in different carbon low alloyed steels. They observed a lower pre-melting temperature at higher sulphur contents, as shown in Figure 4.18.

Consequently, to analyse the effect the sulphur can have in the SSF process, a steel grade with different sulphur contents will be tested. In this case, the previously utilised 42CrMo4 steel grade will be used with low, medium and high sulphur contents.

As observed in the HT-CLSM, there is no melting until temperatures close to the solidus measured by the DSC. Therefore, at medium and low sulphur content it is not expected to observe any liquid, but its effect should be seen in the case of severe embrittlement. In the case of high sulphur content, a softer deformation behaviour and different sulphur distribution through the material are guessed.

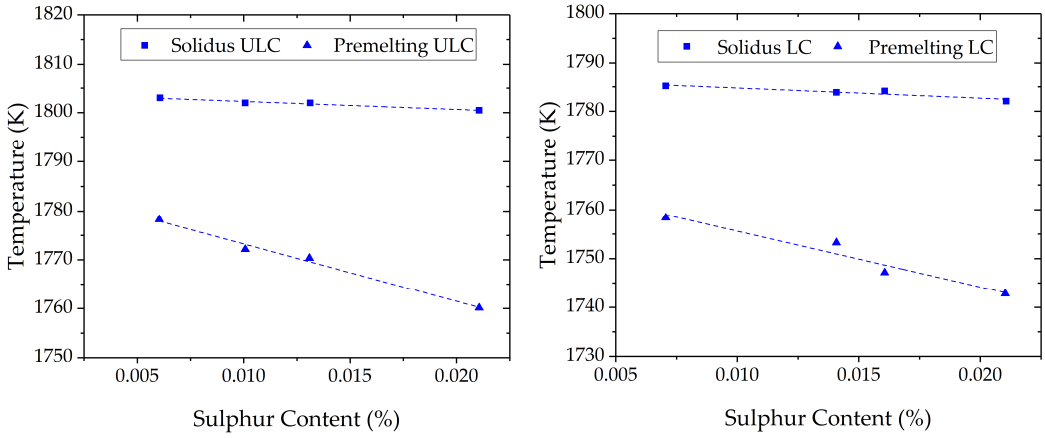

(a) **(b)**

Figure 4.18 – Difference between the solidus and incipient melting temperatures for different sulphur contents in a (a) Ultra Low (ULC) and (b) Low (LC) carbon steels [87].

The tests will consist of some quenching experiments at different temperatures to observe any sulphur segregation or liquid traces. Then, some components will be manufactured to observe whether the generated embrittlement (if any) means a change in the recorded load or not.

4.3.1. Material

The material used for these experiments is the 42CrMo4 steel grade with low (L), medium (E) and high (H) sulphur content. The composition of the three grades is shown in the following table (Table 4.1).

Table 4.1 – Chemical composition of the three 42CrMo4 steel grades.

	C	Mn	Si	P	S	Cr	Ni	Mo
42CrMo4L	0.41	0.90	0.29	0.011	0.003	1.08	0.11	0.19
42CrMo4E	0.42	0.80	0.25	0.011	0.024	1.08	0.10	0.21
42CrMo4H	0.41	0.84	0.22	0.010	0.083	1.06	0.11	0.19

The material is supplied in cylindrical bars by SIDENOR. It is fabricated by continuous casting. After that, it is subjected to hot rolling and a quenching and tempering treatment. The treatment conditions for the 42CrMo4E are explained in section 3.4.3.1. The treatment conditions for the low and high sulphur contents are slightly different in terms of temperature and timing (Figure 4.19).

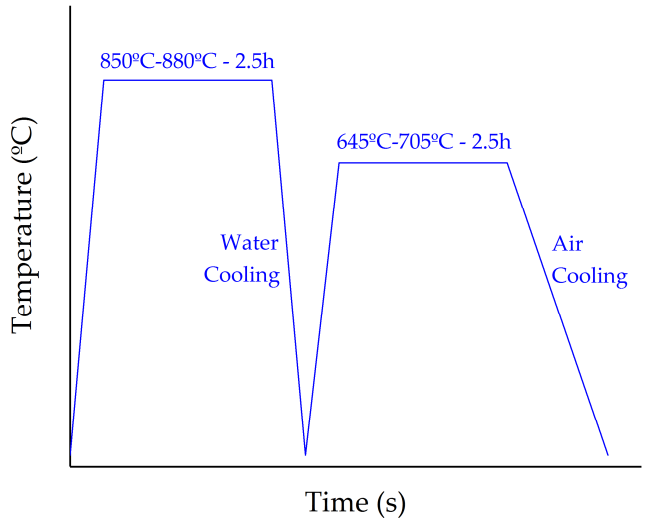

Figure 4.19 – Quenching and tempering heat treatment conditions of the as supplied 42CrMo4L and 42CrMo4H steel grades.

4.3.2. Quenching tests

The quenching tests have been carried out by heating 15 mm diameter and 20 mm long samples (Figure 4.20) up to three different temperatures: the temperature at which the components are made (1360°C) and other two 30°C above and below this temperature (1390°C and 1330°C). In the subsequent step, the sample is water quenched to freeze the microstructure.

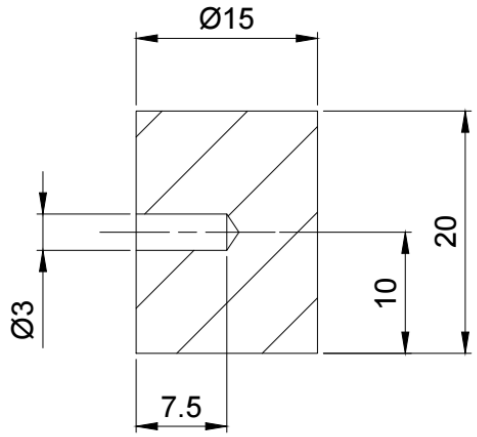

Figure 4.20 – Schematic illustration of the samples used for quenching experiments.

The heating has been carried out in a 15kW SMJR-15 induction equipment without any protective atmosphere as the heating has been manually controlled to be as fast as possible. It must be noted that the experiment was carried out using type K thermocouples with Inconel covering, which means that they are working in the limit of their temperature range. This could imply a deviation in the measured temperature. In addition, as the thermocouple is located in the centre of the billet (Figure 4.20), it is highly possible to have a thermal gradient between the surface (higher temperature) and the centre.

In the following lines, the results of the evaluation of the microstructures by taking advantage of a Scanning Electron Microscope (SEM) and the Electron Diffraction Scattering (EDS) technique are explained.

4.3.2.1. 42CrMo4L

Initial Microstructure

In Figure 4.21, the MnS shape in the as-supplied material is shown. The MnS precipitates are observed to be hosted in pore-like cavities, probably due to the sample preparation. There are not many of them and their size is of the order of 2 μm.

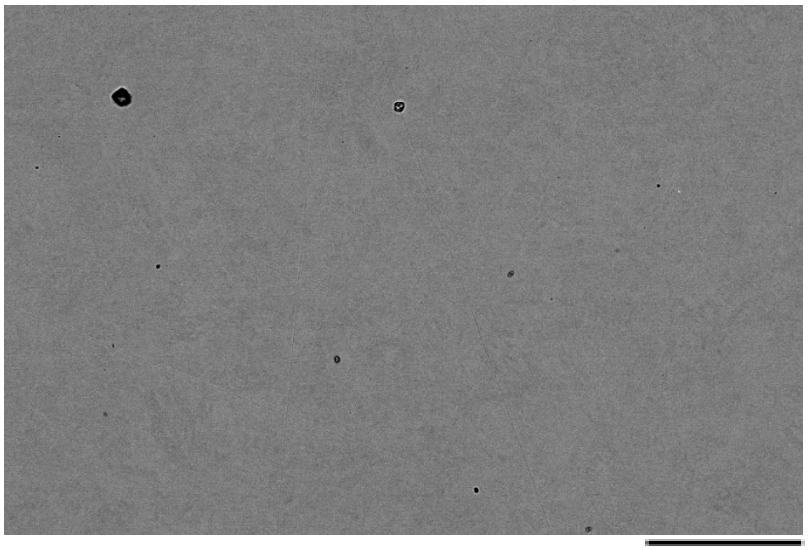

Figure 4.21 – Initial MnS distribution in the as-supplied 42CrMo4L steel. Scale bar: 50μm.

Quenched Microstructure

After quenching, long cracks starting from the surface are generated due to thermal contraction. The higher the temperature, the larger and wider the cracks. In Figure 4.22, some examples of the observed cracks are shown. In any case, neither liquid traces nor sulphur segregation is observed. Most of the S content leads to MnS sulphides creation and neither those seem to be the responsible for this cracking. All the MnS have the same shape as observed in the as-cast sample. It has not moved or segregated to the grain boundary, where the crack seems to happen. This may suggest that at these temperatures the grain boundary itself is soft or brittle enough to enable cracking.

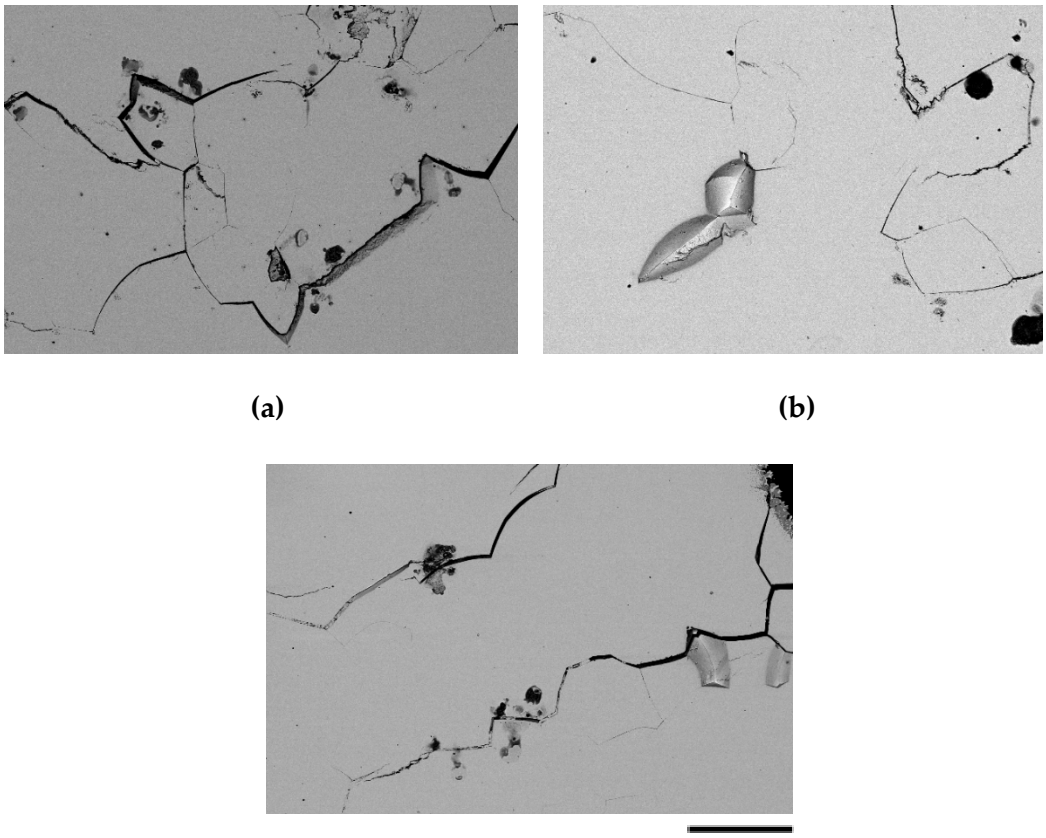

(a) **(b)**

(c)

Figure 4.22 – Examples of the generated cracks during quenching from (a) 1330°C close to the surface, (b) 1360°C in the mid-length and (c) 1390°C close to the surface. Scale bar: 200μm.

4.3.2.2. 42CrMo4E

Initial Microstructure

At this medium sulphur content, an appreciable increase in MnS is noticed. Even if bigger and not as round as in the previous case, they still remain being isolated particles dispersed through the sample (Figure 4.23).

Quenched Microstructure

In the same fashion as before, no liquid traces or sulphur segregation is noticed. The same grain boundary cracking is observed. However, at this sulphur content, as the MnS content is higher, there are some that are inside the created cracks (Figure 4.24). This does not necessarily mean that the precipitates are the responsible for cracking, it is more likely that they act as crack propagators.

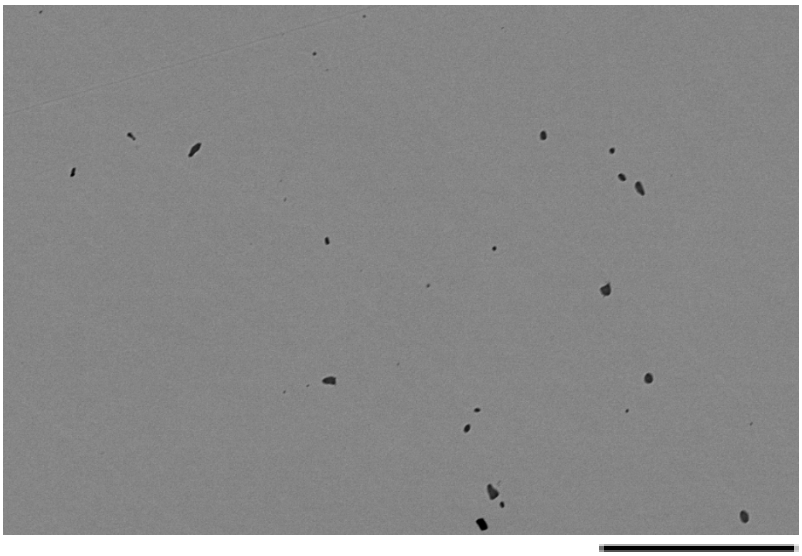

Figure 4.23 – Initial MnS distribution in the as-supplied 42CrMo4E steel. Scale bar: 50μm.

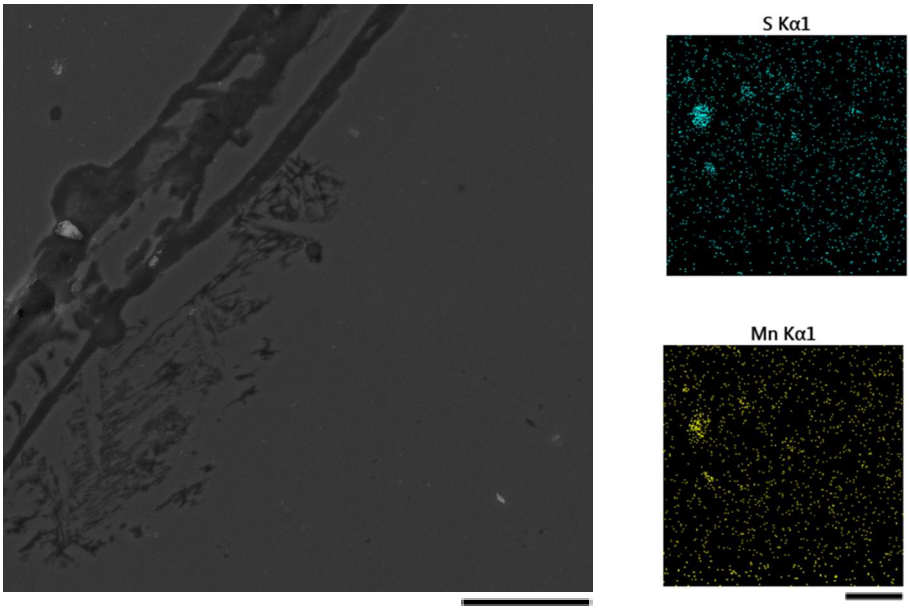

Figure 4.24 – Example of a crack with MnS precipitates on it. Scale bars: 10μm.

4.3.2.3. 42CrMo4H

Initial Microstructure

At this sulphur content, an evident increase in the amount of MnS sulphides and their size is noticed. As shown in Figure 4.25, they are not only isolated round particles. They are now groups of round precipitates as well as large and big (around 10 μm) MnS sulphides.

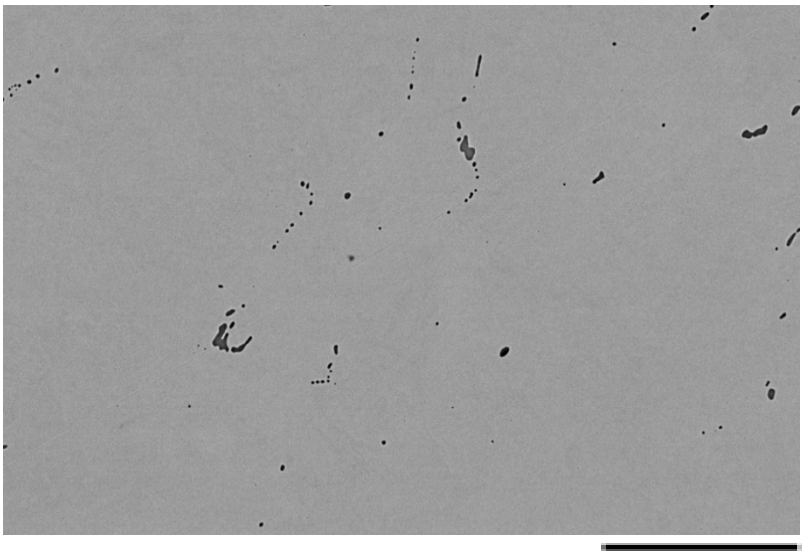

Figure 4.25 – Initial MnS distribution in the as-supplied 42CrMo4H steel. Scale bar: 50μm.

Quenched Microstructure

At these conditions, no liquid traces or sulphur segregation is observed. The quenched microstructures confirm the effect of MnS as crack initiation or propagation zones. In the Figure 4.26 how the generated cracks go along the sulphides can be clearly observed. Note that these images are taken from the areas close to the mid-centre of the sample, wherein the other steel grades no cracks were noticed.

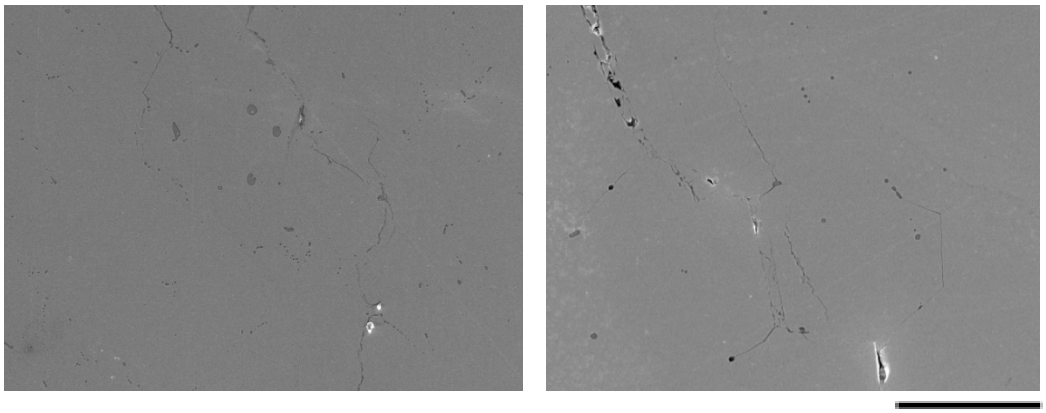

(a) **(b)**

Figure 4.26 – SEM images of cracks crossing MnS sulphides for (a) 1330°C and (b) 1390°C. Scale bar: (a) 100μm and (b) 50μm.

4.3.3. Component manufacturing

After the quenching tests, it seems that the steels with higher amounts of sulphur are more brittle and, therefore, will deform easier at the studied temperatures. In order to analyse this effect on 42CrMo4 steels with different S content, some components with each grade will be manufactured.

The manufacturing set up is the same explained in section 3.3. The selected geometry for these experiments is the R part as it was successfully tested with this material. The heating cycle is the one designed to reach 1360°C with the 42CrMo4E (see section 3.4.3.1). In the following table (Table 4.2) the registered peak loads are shown:

Table 4.2 – Average of the recorded peak loads during manufacturing the three 42CrMo4 steel grades.

	42CrMo4L	**42CrMo4E**	**42CrMo4H**
Average recorded load	251t	254t	252.3t

The observed results suggest that there is almost no difference between manufacturing any of the studied steel grades. The recorded peak loads are very similar for all the cases, which could imply that the material resistance differences are minor in comparison with peripheral effects.

Indeed, higher peak loads were identified when the initial billet volume was little bigger than required. In the same fashion, lower peak loads were registered when the clamping system was not properly closed. Therefore, in the case of this steel grade, it seems that the material resistance during filling is pretty similar and that the sulphur content, even if it can have a minor influence, is not the responsible for the observed flow capabilities.

4.3.4. Conclusions

It is clear that at lower amounts of S, lower MnS precipitates are created. However, they were already present in the as supplied microstructure. This means that they were not created during the reheating but during the steel manufacturing process. Despite all the uncertainties the temperature inhomogeneity through the sample and the temperature control can generate, it is clear that the sulphur has not segregated to the grain boundaries and, consequently, it has not created nor a lower temperature composition either a brittle grain boundary.

Regarding the MnS sulphides, they melt at 1610°C, which means that this precipitate will still be solid at the considered temperatures. Its dissolution is more likely to happen, but this does not occur until 1420°C, a temperature that is still above the working ones and where the solubility of MnS suddenly increases (Figure 4.27). The work of Gu et al [80] shows in-situ in an HT-CLSM how, even at semi-solid state, the MnS particles are still present in a C45 steel grade.

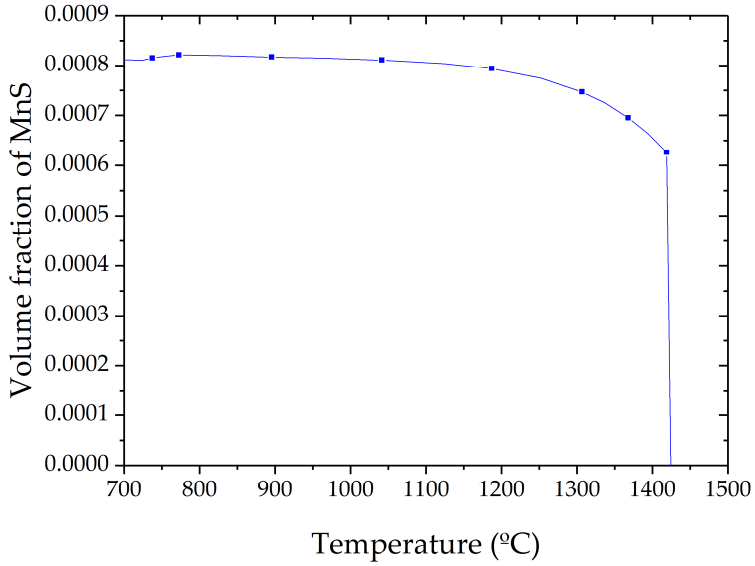

Figure 4.27 – Volume fraction of MnS particles against temperature for the case of 42CrMo4E.

In any case, the influence of MnS enhancing the embrittlement is widely proved [88]. If those precipitates are created in the grain boundaries, they can act as crack initiation and propagation zones, therefore reducing the required force to deform the material. This suggestion seems to be reasonable observing the cracks generated around some MnS particle caused by thermal contraction.

This phenomenon, indeed, can explain the behaviour of the material during hot tensile and compression tests. If the grain boundary itself is weak and there are some crack initiation or propagation precipitates like MnS, the material could behave as it was observed in sections 4.2.4 and 4.2.5.

Nevertheless, this possible softening does not seem to be high enough to consider it as the reason for the observed material flowing behaviour. The manufacturing tests do not exhibit any load difference between the three steel grades, which means that if it has an effect, it is minor at the studied conditions. In addition, even if the material´s flow curves at high temperatures shows its softness,

it is hard to think that this phenomenon is enough to increase the fluency of the material to create the flash observed in the components (Figure 3.11).

This analysis suggests that thermal effects may not be the unique ones having an influence on what is happening to the material and that the influence of other variables like deformation and deformation rates should be considered. Hence, in an attempt to analyse the effect the deformation and deformation rates could imply to the material, the observation of a possible adiabatic heating in the material will be carried out.

4.4. Adiabatic Heating

Forming processes are based on modifying the initial shape of a material to obtain the desired geometry. Therefore, the material is subjected to different degrees of deformation depending on the shape to attain. As the initial geometry of the material is permanently deformed, we are facing processes that imply plastic strains, which are responsible for heat generation in deformed regions. This heating phenomenon is the so-called "*adiabatic heating*".

4.4.1. Brief literature review

4.4.1.1. Adiabatic heating concept

The adiabatic heating is defined as a process where there is no heat transfer between the studied system and the surrounding environment. In the studied case, the heating source comes from the work generated due to plastic deformation of the material in a very short lapse of time. Therefore, one can assume that this phenomenon would be driven by the material and the deformation conditions.

Material

The material deformation behaviour will highly define the temperature rise as a consequence of adiabatic heating due to the generated amount of plastic energy is directly related to the material composition and crystallographic structure.

In the solid state, the material can be deformed either elastic or plastically. The former means a recoverable deformation whereas the latter implies a non-recoverable deformation without reaching to fracture. In the elastic regime, the atomic bonds of the crystallographic structure are stretched without reaching to slip. In the plastic regime, the atomic bonds are broken enabling further material

deformation without changing the volume. This is mainly governed by the so-called "*slip*" and "*twinning*".

The slip (Figure 4.28 (b)) occurs when the crystal planes glide past each other thanks to the movement of dislocations, defined as linear defects where the crystallographic registry is lost. It means that the atoms move through the lattice from site to site and, therefore, the orientation of the crystal is not modified. Conversely to the slippage, the twinning (Figure 4.28 (c)) does not disrupt the position of the atoms in the crystal but it does the orientation. In this case, the crystal plane twists generating a region of three or more different oriented planes [89].

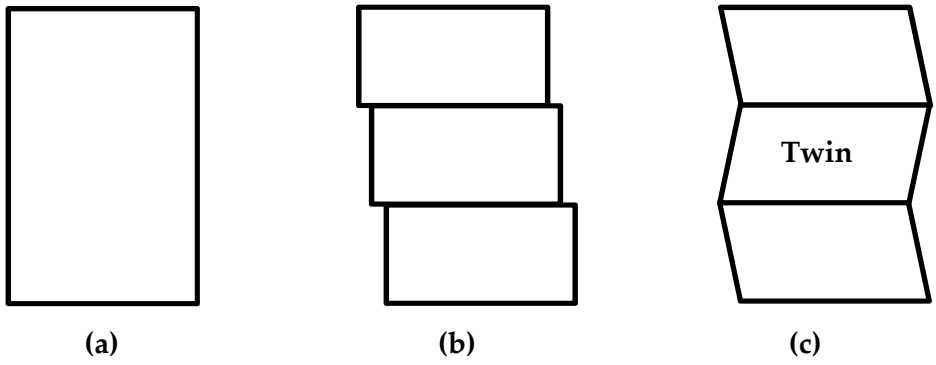

Figure 4.28 – Schematic illustration of (b) slip and (c) being (a) the initial state of the crystal plane.

When one or the other happens is influenced by the deformation conditions but, more severely, by the material. The first influencing factor is the crystallographic structure of the material (or how the atoms are ordered through the material). It will define the ease of the material to slip. In this case, comparing the two most common structures in steels, Face Centered Cubic (FCC – austenite) and Body Centered Cubic (BCC - ferrite) structures, the atoms ordering makes a difference in letting the slip to happen. While the FCC structures have 12 preferential planes to slip, among the 48 slip planes the BCC consist of, none is preferential. This means that a priori, the BCC structure will have more difficulties to slip in comparison with the FCC.

However, the material has another influencing parameter called "*Stacking fault energy*" (SFE). A crystal plane is composed of a chain of atoms with the same structure and orientation. However, the order of those atoms usually has some irregularities in the planar stacking sequence called "*stacking fault*" (SF). The width of this SF depends on the repulsion and attraction balance of the system which is directly related to the alloying elements of the material. Therefore, if the studied

alloy has a high SFE, the SF width will be smaller letting the atoms to be closer and, hence, enhancing the slippage. On the contrary, if the alloy has a low SFE, the SF will be wider decreasing the mobility of dislocations and consequently enhancing dislocation accumulation and twinning deformation [90]. Some researchers have taken advantage of this effect to strengthen an Mg alloy [91].

Looking at this, it is clear that it is easier to deform a material that enhances the slippage. This means that the energy required to deform an FCC material with high SFE will be lower than that required to deform a BCC material with a low SFE. Moreover, the adiabatic heating is defined as "the instantaneous dissipative heating that occurs during plastic deformation" [92] which releases the heat generated due to the applied deformation energy. Therefore, the material that opposes more resistance to deform will generate more adiabatic heating.

Deformation conditions

The adiabatic heating is the phenomena that happens when a material is deformed in such a short lapse of time that the generated heat due to the creation of dislocation and deformation twins is higher than the heat dissipated to the surroundings. Hence, higher strain rates will imply the creation of higher amounts of dislocations and deformation twins per second, which will translate in a greater self-heating as there would be less time to release the heat.

Moreover, the deformation conditions have a direct impact on the material dynamic behaviour. Considering that the material is being deformed, one can expect that the mechanical behaviour of the material will be influenced. In this case, strain hardening and softening effects can be generated as a consequence of dislocation and deformation twins' generation. This would mean a greater or lower resistance to continue deforming the material which depends on the applied strain rate. Therefore, how they are developed during deformation will influence the generated plastic energy and, thus, the adiabatic heating.

4.4.1.2. Adiabatic heating in steels

The adiabatic heating phenomenon has been widely studied in the machining field. It is true that it influences many forming processes, but not at the same level as it does in machining. In their case, the cutting of the material generates a huge sudden temperature increase in the so-called "primary" and "secondary" zones. This heating is due to the adiabatic heating, which is driven by the produced large deformations and high rates.

In order to try to predict the evolution of these zones, many researchers have tried to shed light on the material behaviour at these conditions. One interesting work related to this is the research of Hor et al [93]. They characterised the mechanical behaviour of 42CrMo4 and 100Cr6 steel grades over several strain rates at temperatures ranging from 20°C to 1000°C. They divided the tests depending on the forming domains in terms of temperature (Ts means the solidus temperature of the material).

- Cold working domain: $T/Ts<0.3$
- Semi-hot working domain: $0.3<T/Ts<0.5$
- Hot working domain: $T/Ts>0.5$

Hor and co-workers used a GLEEBLE 3500 thermomechanical testing machine for compression at low and moderate rates and a Split Hopkinson Pressure Bar (SHPB) apparatus for high compressive rates. In order to reach also to higher strain levels, they used a hat-type shear sample in the GLEEBLE equipment.

They observed that the adiabatic heating starts having influence at 10s-1 strain rates. Until 1s-1 rates, the material seems to behave quasi-statically. However, Andrade-Campos et al [94] observed during tensile tests in an AISI 304 stainless steel a 70°C temperature rise at 1s-1. Therefore, the strain rate condition for the generation of the adiabatic heating seems to be somewhere between 1 and 10s-1.

Regarding the cold working region, Hor observed a 120°C temperature increase in the surface but an even higher temperature rise was expected to exist in the centre of the specimen. For the case of the semi-hot working domain, they did not analyse the temperature rise but the mechanical behaviour of the material. They did not observe any significant effect on the mechanical behaviour of the material caused by self-heating during compression, but they did during shear tests. A softening effect was observed as a result of localised adiabatic heating in the shear zone of the sample. This last fact confirms the influence of large strains on the generation of adiabatic heating.

Lastly, they concluded that in the hot working domain the adiabatic heating has no influence due to the low stress the material presents at these conditions. It seems then that at these temperatures no self-heating should happen. Nevertheless, Mirzadeh et al [48] observed a 15°C temperature rise in a 17-4H stainless steel sample compressed at 1000°C. The same temperature rise was recorded during compression of 22MnB5 at 750°C by Naderi et al [95]. Both tests were carried out at 10s-1 strain rate. In any case, those observed temperature raises do not seem to be enough to think about the creation of liquid during the SSF process.

4.4.1.3. Adiabatic heating estimation

It has been already mentioned several times but it is important to remember that the adiabatic heating is produced due to the generated plastic deformation on the specimen. Therefore, it is reasonable to think that we can obtain somehow the amount of expected generated plastic work from the flow stress curve of the material. The following equation is commonly used for this purpose:

$$W_p = \int_0^{\varepsilon_p} \sigma(\varepsilon_p, \dot{\varepsilon}_p, T) \cdot d\varepsilon_p \quad \textbf{(4)}$$

where W_p means the produced volumetric plastic work (J/m^3) and σ (Pa) means the recorded true stress depending on the plastic strain (ε_p), plastic strain rate ($\dot{\varepsilon}_p$) and sample temperature (T). Considering that the stress is not constant during the deformation, the generated plastic work would not be either constant. Therefore, the integral of the flow stress change against the produced deformation will define the evolution of the created amount of plastic work. Once it is properly defined, one can guess the expected temperature rise is the result of the following expression:

$$\Delta T = \frac{W_p}{\rho \cdot C_p} \quad \textbf{(5)}$$

where ρ and C_p are the material density (kg/m^3) and heat capacity (J/kg·K) respectively. Nevertheless, not all the plastic work converts into heat. In cold working investigations, it has been observed that there is a certain fraction of the plastic work that dissipates to the surrounding and another part that remains in the material as latent energy [96,97]. This fraction is known as "Inelastic Heat Fraction" (IHT) or "Taylor-Quinney coefficient". Many researchers have developed different equations assuming different phenomena to calculate this parameter [98–100].

If high temperatures are considered, there is no chance to store any latent energy but the heat loses to the surrounding begin to have greater influence. Therefore, depending on the experimental setup, conduction, convection and radiation lose should be considered as the plastic work dissipation modes.

4.4.2. Adiabatic heating at high temperatures

With the information in the literature one can easily neglect the adiabatic heating effect on the material at the temperatures this work deals with. However, based on the compression tests of 42CrMo4 (see section 4.2.5) and the adiabatic

heating calculation (equations 4 and 5), a sudden temperature increases of about 10°C should happen during a normal compression test if the temperature is recorded. Therefore, to be sure whether we can neglect or not this phenomenon, some compression tests recording the temperature will be performed and compared with the theoretical temperature rise.

4.4.2.1. Materials

The selected material for the following tests is the Invar 36. This steel grade is an almost pure Fe-Ni alloy with a very low thermal expansion that is commonly used in precise engineering to manufacturing parts for watches and engine valves, among others. The material is supplied by Aperam in bars of 10mm diameter and 500mm long. Its composition is shown in the following table (Table 4.3):

Table 4.3 – Chemical composition of the Invar 36 steel grade.

C	Mn	Si	P	S	Cr	Ni	Cu	Co
0.004	0.30	0.098	<0.003	0.005	0.07	36.22	0.02	0.05

The reason for selecting this material comes from the possibility of analysing its microstructure after the experiment in case we observe something interesting during the tests. As it is an austenitic steel, there is no phase transition during cooling from working state until ambient temperature. Moreover, the "*cleanliness*" of this material in terms of alloying elements makes easier the microstructural analysis.

4.4.2.2. Experimental procedure

The compression tests have been carried out in the HDS-V40 thermomechanical Gleeble equipment of the Advanced Steel Research Centre of the University of Warwick (Figure 4.29 (a-b)). As previously, 10 mm diameter and 15 mm height samples are used. The top surfaces of the samples must be as parallel as possible and free from any flash to avoid any hot spot due to Joule heating. The material at these temperatures can adhere to the anvils easily. Therefore, graphite and tantalum foils in each side have been used. To ensure a proper heating performance, Nickel paste has been applied between each element from the anvil to the sample. This will create good contact ensuring the power to go through all the elements without loses.

(a) **(b)** **(c)**

Figure 4.29 – (a-b) Gleeble HDS-V40 thermomechanical equipment of the University of Warwick and (c) utilised sample.

This equipment also controls the temperature in a closed loop. In this case, Type C thermocouple wires are placed into two 2-3 mm deep and 0.7 mm diameter holes (one wire per hole as shown in Figure 4.29 (c)). This thermocouple set up ensures that they will not detach from the sample during the deformation. In the following figure (Figure 4.30), the experimental procedure is shown.

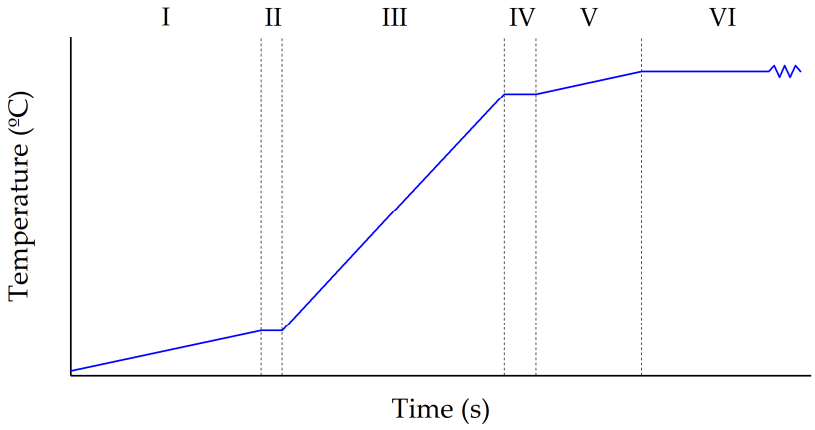

Figure 4.30 – Schematic illustration of the experimental sequence for compression test.

I- Heating from ambient temperature to 200°C at a rate of 1°C/s. This stage is oriented to burn the nickel paste to ensure a great conductivity through all the elements.

II- 20 s of holding to ensure a quite homogeneous and stable temperature before the start of the fast heating.

III- Heating up from 200°C to 100°C below the aimed temperature at a rate of 5°C/s.

IV- 30s holding time to balance the overshooting that the PID creates (between 5-10°C).

V- Heating up to the last 100°C at a rate of 1°C/s to ensure a low overshooting (2-4°C).

VI- 2 minutes of holding at the working temperature to homogenise the temperature through the sample. Once the holding time finishes, the heating control is switched off and the deformation at 10 s^{-1} while recording the temperature happens.

4.4.2.3. Results

Surprisingly, a temperature peak during compression at the explained conditions and at temperatures well above 1000°C have been noticed. The Figure 4.31 explains the shape of the recorded temperature against time results for the compression tests without heating control during deformation.

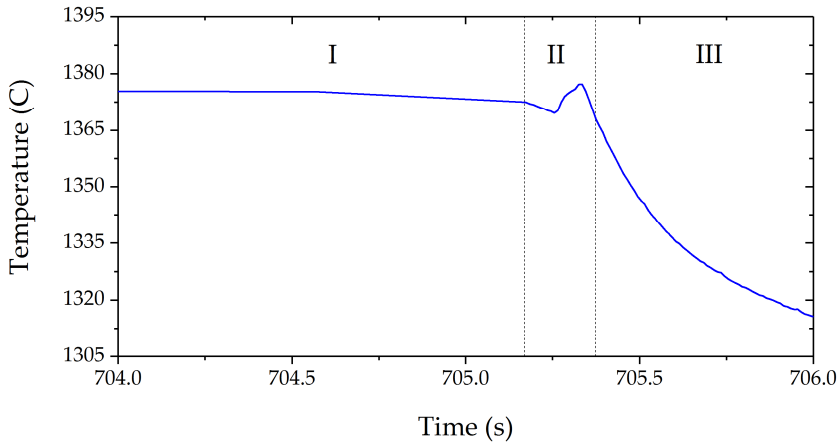

Figure 4.31 – Schematic illustration of the obtained temperature against time curve for the compression test without heating control.

I- Stage VI of the process described in Figure 4.30. Last seconds of homogenisation time and ram placement to the acceleration position.

II- The deformation at a constant strain rate ($10s^{-1}$) happens. The recorded peak exhibits a delay due to the time needed for the ram to accelerate and contact the sample holder as well as the time needed for the material to conduct the generated temperature to the thermocouple. The thermocouple installation also has a significant influence on the recording quality.

III- Natural cooling of the deformed sample mainly via conduction through the anvils and ram movement to the initial position.

At the same time that this curve was recorded, the true stress against the true strain curve was also obtained for each case (Figure 4.32). These curves give us the strength of the material at such temperatures. Therefore, we can take advantage of this information to calculate the theoretically expected temperature rise by using the equations 4 and 5 (see section 4.4.1.3). Then, the theoretical and measured temperature increase can be compared. The measured maximum increase is calculated considering the temperature when the peak starts and the maximum recorded temperature of the peak. Note that the theoretical temperature rise assumes that all the generated plastic work converts into heat (no loses). In Table 4.4, the results are compared.

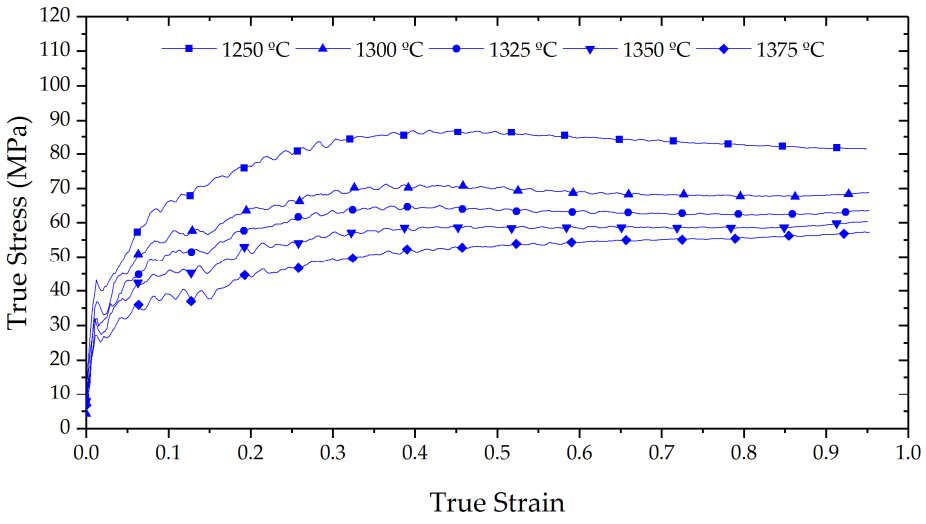

Figure 4.32 – Obtained True Stress against True Strain curves on INVAR 36 for different temperatures at a strain rate of $10s^{-1}$.

Table 4.4 – Comparison between the measured and calculated temperature raises.

Temperature	1250°C	1300°C	1325°C	1350°C	1375°C
Theoretical raise	26°C	21.35°C	19.4°C	17.7°C	16.1°C
Measured raise	13.83°C	6.62°C	9.14°C	8.76°C	7.54°C
Difference percentage	53.2%	31%	47.11%	49.49%	46.83%

It can be observed how the measured temperature increase is well below the theoretical. Nevertheless, this was expected to happen as a consequence of the cooling of the sample, which becomes more severe while deforming because of the increase of the contact area. Moreover, as mentioned before, the placement of the thermocouple also influences the recorded result. It can be seen how the measured raise for the case of 1300°C has dropped presumably due to a bad thermocouple attachment.

In any case, the observed tendency of the amount of plastic energy converted into heat that remains in the sample seem to be logical. At lower temperatures, the cooling rates are lower and the generated amount of plastic work increases due to the material's strength is higher.

Although it is confirmed the heating generation at these temperatures, the increase is still low. Considering the solidus temperature of the tested material (~1450°C), quite a few more degrees are required to observe a high enough self-heating to overcome it. Therefore, it should be needed an increase in the generated plastic work at the same time that the cooling loses are reduced.

The cooling loses can be easily avoided by increasing the deformation rates. In this way, the material will not have time to cool excessively down. Regarding the plastic work, the increment of strain rate could have influence as it could increase the resulting stresses. However, this increase does not seem to be great enough to generate the required plastic work amount. Therefore, the unique parameter that can be fitted to do so is the strain which, in fact, is quite high in some areas of the geometry due to the extrusion-like deformation type.

Hypothetical approach to large strains

If it is assumed that the flow curve of the material at these conditions reaches a steady stress value at strains of 1 (Figure 4.33), fact that was observed in a close temperature regime in the work of Hor et al [93], one can easily calculate the theoretical plastic work of the material deformed over strains of 1.

If one makes the fitting of the curves of Figure 4.32 while considering the steady state, it is easy to calculate the plastic work generated at different temperatures and large strains. Assuming the ideal situation where no heat loss happens, the following figure shows the temperature increase for different temperatures after the hypothetical material deformation at $10s^{-1}$ strain rate (Figure 4.34).

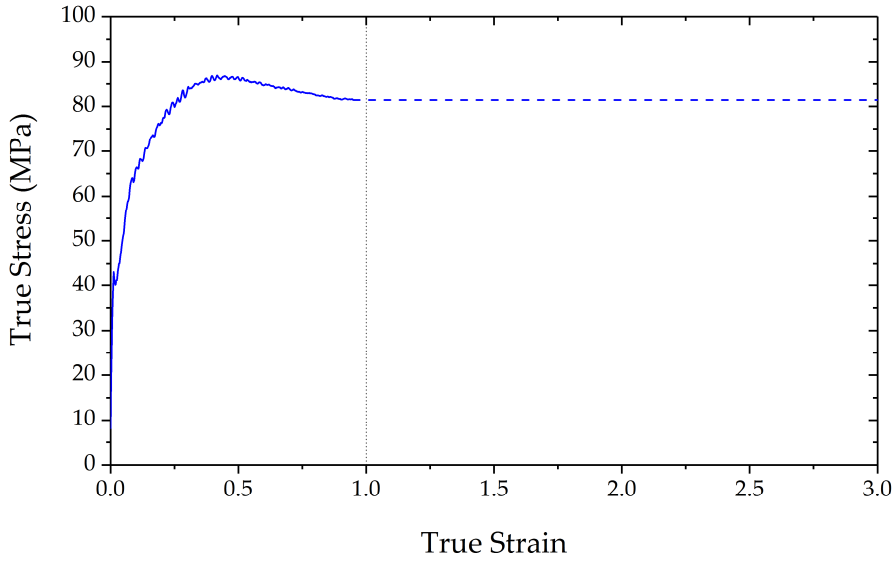

Figure 4.33 – Schematic illustration of the hypothetical flow stress curve evolution at strains larger than 1 for the case of Invar 36 at 1250°C.

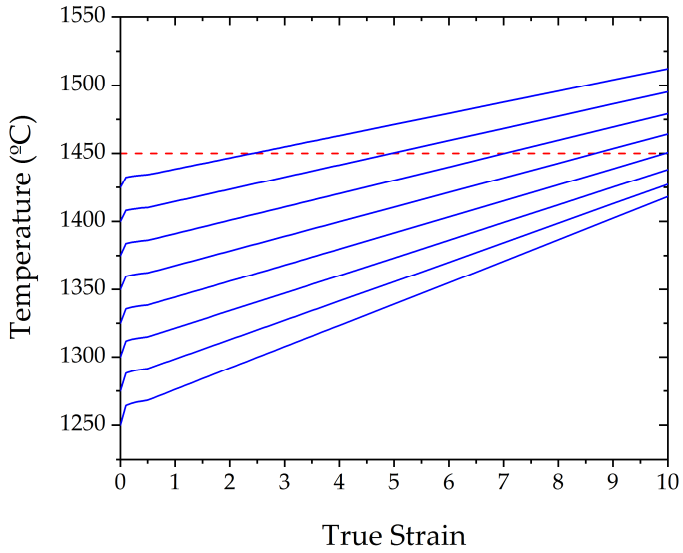

Figure 4.34 – Hypothetical temperature rise curves due to adiabatic heating during the Invar 36 deformation at large strains and $10s^{-1}$. The dashed red line means the solidus temperature of the alloy.

Looking at those hypothetical results, it seems sensible to expect temperature rises of the order of 50°C at strains between 4 to 6. To analyse if it is realistic the obtaining of such strains, a rough extrusion simulation has been carried out using COMSOL Multiphysics software assuming low friction values and the Invar 36 material flow curve according to a Ludwick type fitted equation. The registered values of the localised strains are around 4 in the areas close to the surface (Figure 4.35). Consequently, it seems worthy to analyse this phenomenon at large strains.

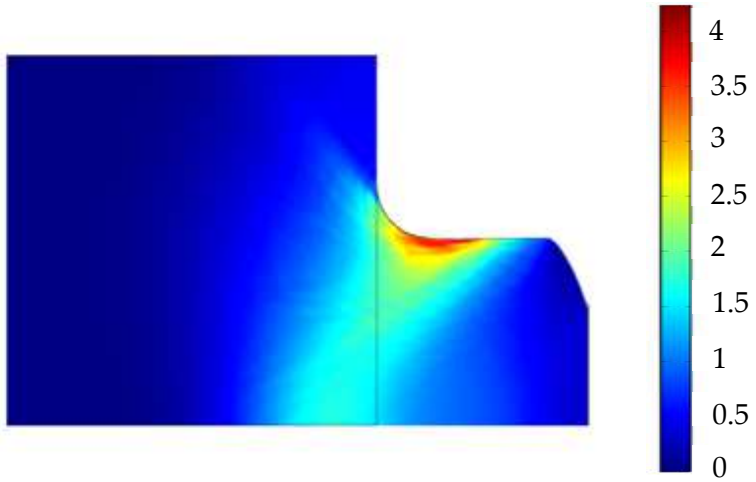

Figure 4.35 – Picture of the simulated strains during a simple extrusion tests with an Invar 36.

4.4.3. Large strain tests

The obtaining of large strains while recording the force with a simple and homogeneous deformation distribution is a very complicated issue. It becomes an even higher challenge if the goal lies on relating the measured results with the generated true stresses.

These large strains usually happen in extrusion-like material deformation, and more precisely in the surface area due to friction. However, it is impossible to obtain any true stress against true strain relationship from such an inhomogeneous deformation. That is why when large strains are aimed to be tested, shear experiments become the best solution.

Introduction to shear experiments

The shear tests simply consist of a material subjected to shear stresses (Figure 4.36). This type of deformation means high strains at low displacements. There are many different sample geometries depending on the equipment and research topic [101–104], but all of them are prepared to deform one specific zone as homogeneous as possible.

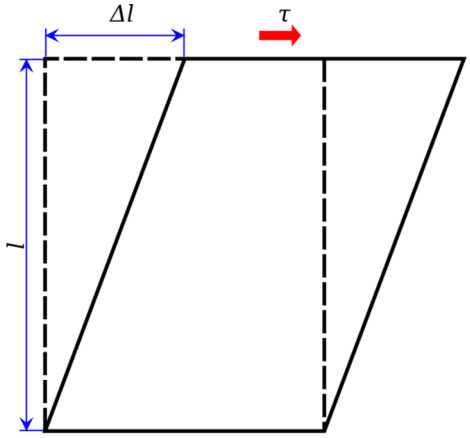

Figure 4.36 – Schematic illustration of a square subjected to shear.

As mentioned, the main drawback of this experiment is the complexity to ensure a homogeneous deformation. This homogeneity is secure when only shear type deformation is happening in the sample. However, usually bending of the material happens creating a mix of deformation types and affecting the accuracy of the measurement.

This last fact implies a higher complexity to relate the recorded force and displacement with the generated stresses and deformation. If different deformation modes are happening at the same time, the strain stops being homogeneous and, therefore, the relation between the theoretical and real deformation could differ significantly.

One of the most used techniques is the torsion tests, where a pure shear deformation is ensured. However, as the specimen is cylindrical, the generated shear strain goes increasing along the radius. Hence, the generated shear strains in the surface are very high while in the centre are almost zero. In this case, even if the sample is subjected to pure shear, the inhomogeneous distribution of the deformation makes it hard to properly define the generated deformation and stresses.

Regarding the studied case, the shear tests are aimed to be carried out in the HDS-V40 Gleeble equipment, which can uniquely deform uniaxially in compression mode. As the experiments involve high temperatures, the sample also must be designed to meet the joule heating requirements in the areas to deform. Taking all these into account, the Hat-Type sample (Figure 4.37) has been selected as the best geometry to optimise so as to meet the required conditions.

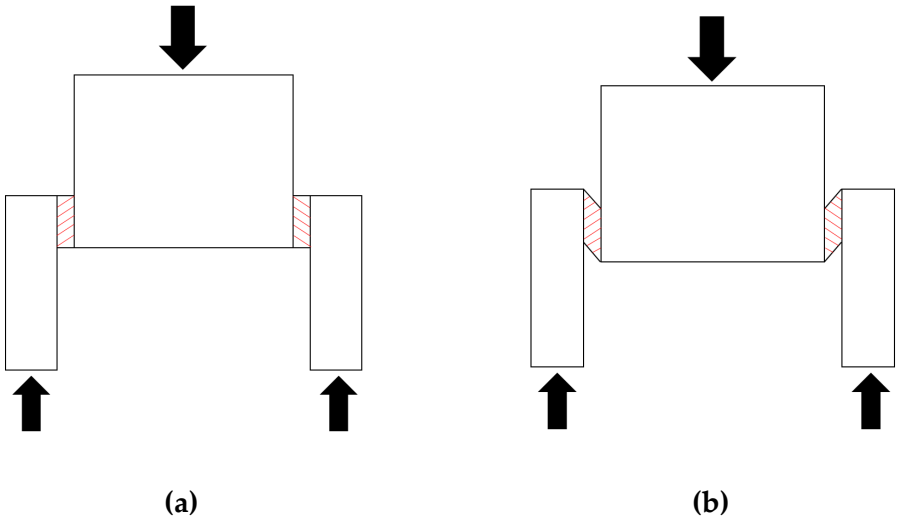

Figure 4.37 – Schematic illustration of the Hat-Type shear sample (a) before and (b) after deformation. Note that the sample is cylindrical.

This geometry was first used by Hartmann et al [105] in 1981 and further optimised by several researchers [106,107]. In the studied case, the sample shape used by Hor et al [93] will be used as it was designed for a Gleeble equipment.

Modelling the shear experiment

The Hat-type sample dimensions must ensure a correct heating of the shear zones by Joule effect at the same time that as homogeneous shear deformation as possible is generated. To analyse the best sample dimensions, simulations using COMSOL Multiphysics have been carried out. The selection of this software comes from the ease to set up a two steps simulation: Joule heating and deformation.

Joule Heating Simulation

The Invar 36 austenitic steel will be used for these experiments to still have the chance of post-mortem analysis. As they are supplied in 10mm diameter bars format, the modified dimensions of the Hat-Type sample geometry will have to be

designed according to it. After several trials, the following dimensions were observed to be the optimum for joule heating (Figure 4.38 (a)).

The heating simulation (Figure 4.38 (b)) was performed by defining a current flow going through the sample responsible for the Joule heating. In order to consider the heat loses, conduction and radiation losses have been considered. A rough estimation of such losses has been considered using approximate values for the emissivity and the conductive parameter.

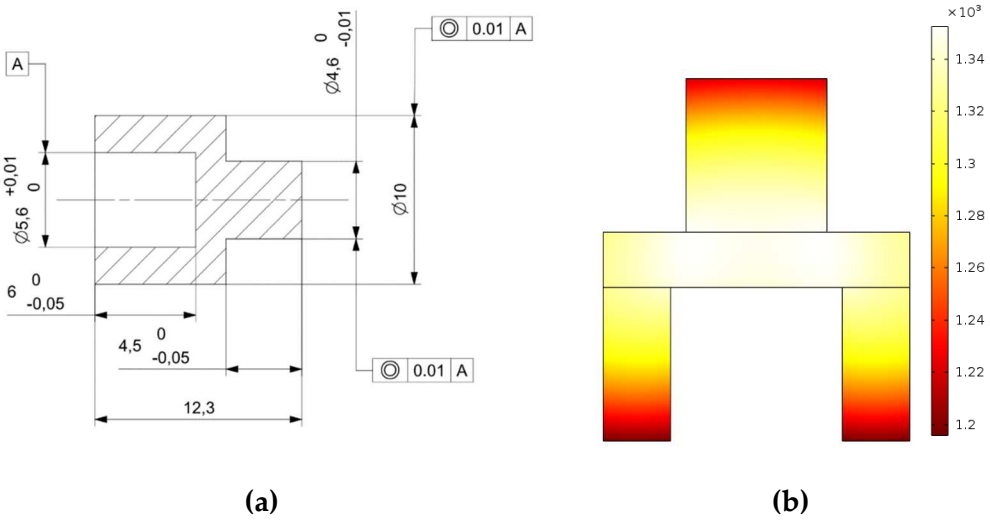

(a) **(b)**

Figure 4.38 – (a) Shear sample geometry dimensions and (b) temperature distribution of the Joule heating simulation using COMSOL.

As shown in Figure 4.38, the shear sample dimensions focus the Joule heating in the shear zones whilst maintaining the top and bottom areas colder. This not only helps to concentrate most of the deformation in the shear zones as they are softer, but also to avoid the sample sticking. This last fact indeed could help to test even higher temperatures than in compression.

The shear zone was tried to maintain as big as possible to have the largest possible area for microstructural analysis. However, this makes the heating very sensitive to any little dimensional deviation. Therefore, care must be taken when machining the samples to try to avoid any minimal geometrical deviation.

Deformation Simulation

Once the heating simulation is acceptable and close to the reality, the deformation simulation can be built. In this case, as the sample has different

temperatures, the material will have different resistances in function of that. Hence, taking advantage of the flow curves obtained previously (Figure 4.32), the material stress-strain performance in function of the temperature has been fitted. However, so as to make the calculations easier and faster, the influence of strain has been neglected assuming a constant plastic stress for each temperature. The following equation and parameter's values (T) are the expressions implemented in the software:

$$\sigma_p = A \cdot (T^B) - \sigma_0 \quad \textbf{(6)}$$

Table 4.5 – Value of the parameters for the equation 6 according to the Invar 36 flow curves.

Parameter	Units	Value
A	MPa/°C	3.64551e17
B	-	-5.03097
σ_o	MPa	50

In the same fashion as before, to reduce the simulation time, only plastic deformations have been considered in the shear section. In the other areas, elastic deformations are only considered. In Figure 4.39 the simulated strain distribution after 1.6 mm ram displacement is shown.

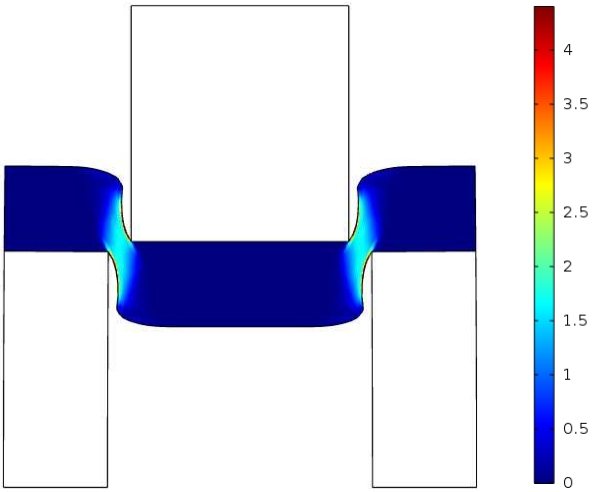

Figure 4.39 – Simulation of the generated equivalent strains after 1,6mm displacement.

The strain results of the simulation seem to be quite homogeneous in the shear zone apart from some peaks in the corners where very localised large deformations seem to happen. The generated equivalent strain in the homogeneous area is between 1.5 and 2. These strains are not excessively large. To increment this value a lower gap size between the upper cylinder and lower hole must be set. In this case, a gap of 0.5 mm has been defined to maintain the calculation time as low as possible since smaller gaps require finer meshes and larger gaps mean smaller strains.

Experimental evaluation

At this point, focusing on the shear sample and the information it could be gathered from the Gleeble equipment, how to relate the displacement data to the generated equivalent or effective strain should be defined. This is crucial to be able to analyse the stress-strain curve from the force-displacement curve. However, this relation is not excessively straightforward as depending on the initial conditions and hypotheses, similar but different expressions can be found [102,108,109]. To evaluate their validity and select the most suitable model, calculated results using some of them will be compared to the simulated output.

The simulation data will consist of tracking different points from the gap during the displacement to observe their deformation evolution (Figure 4.40 (a)). These points are placed at 0.2 – 0.6 – 1 – 1.4 mm distance from the upper surface. The recorded strain against displacement curves are shown in the following figure:

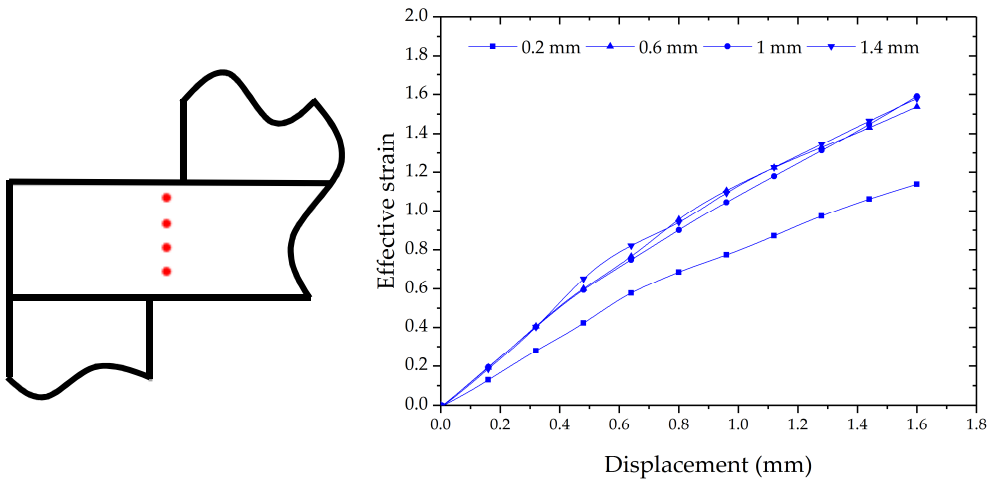

(a) **(b)**

Figure 4.40 – (a) Position of tracked points and (b) strain-displacement results for each one.

Looking at the simulated strain evolution (Figure 4.40 (b)), it seems that even if in the areas close to the corners high strains are observed (Figure 4.39), they are lower than expected close to the surface of the gap (0.2 mm). Nonetheless, in the core of the gap a constant effective strain is estimated (between 0.6 and 1.4 mm).

The equivalent or effective strain value will be calculated and compared by using the models of Stüwe [108] and Pardis et al [109]. These two models are selected as they come from theoretical suggestions to end up on a "true strain" like expression. Other most common and widely used approaches like Tresca or von Mises are only valid for isotropic materials and exhibit a great discrepancy in the studied conditions [102,108]. The main difference between these two models lies in how the deformation takes place. In the case of Stüwe, a square is deformed to a parallelogram (from 1 to 2 in Figure 4.41). In contrast, Pardis and co-workers consider this initial deformation from a square, but from then on, the calculations assume the deformation of a parallelogram to a more deformed parallelogram (from 2 to 3 in Figure 4.41). The effective strain equations of Stüwe and Pardis et al are shown in equations 7 and 8 respectively.

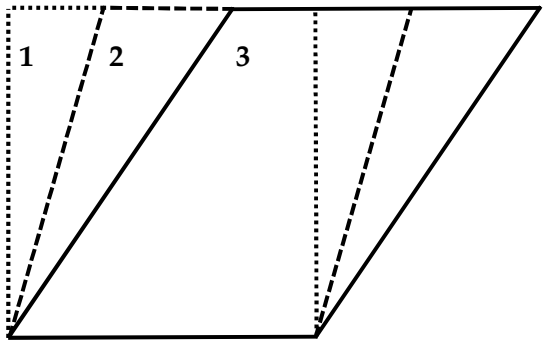

Figure 4.41 – Shape transition during shear deformation. 1-2: square to parallelogram. 2-3: parallelogram to a more deformed parallelogram.

$$\varepsilon_{eff_{Stüwe}} = \frac{1}{2} \cdot \ln\left(\frac{1 + \left(\sqrt{\frac{\gamma^2}{4} + 1} + \frac{\gamma}{2} \right)^2}{1 + \left(\sqrt{\frac{\gamma^2}{4} + 1} - \frac{\gamma}{2} \right)^2} \right) \quad \textbf{(7)}$$

$$\varepsilon_{eff_{Pardis}} = \sqrt{\frac{4}{3} \cdot \left[\ln\left(\sqrt{\gamma^2 + 1} \right) \right]^2 + \frac{(\tan^{-1}\gamma)^2}{3}} \quad \textbf{(8)}$$

$$\gamma = \frac{\Delta l}{l} \tag{9}$$

where γ is the shear strain calculated using the equation 9 according to Figure 4.36. Comparing the results of the effective strain against displacement using these equations and the simulated data, the model of Pardis and co-workers seem to fit closely its evolution in the homogeneously deformed areas (Figure 4.42).

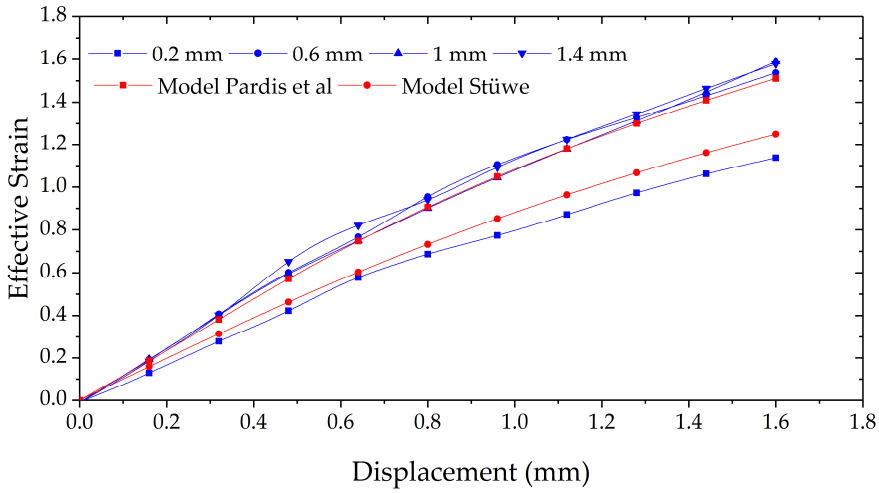

Figure 4.42 – Comparison of simulated and calculated effective strain against displacement.

These results suggest that a homogeneous shear deformation is possible enabling its data conversion to true stress and true strain. However, the simulation has been performed in its simplest version assuming the as simplest case as possible. Therefore, in order to confirm the validity of the shear test, the obtained stress-strain curves should be compared with those attained by compression. If the difference between them is negligible, the suitability of this experimental set up for material characterisation at large strains will be confirmed.

Results

During the first experiments, a non-desirable heating was detected. The sample hottest area was the upper cylinder (Figure 4.43). This could have happened due to the machining of the sample. During the setting up of the Joule heating simulation, it was noticed how a minimal difference in the geometry heavily influenced the heating behaviour. In this case, during machining, the

corners around the gap were smoothed leaving a 0.2 mm radius. This means more material than modelled in this section. Therefore, at these conditions, the top of the sample seems to be the zone with the lower effective section being the first in heating up.

Unluckily, it was impossible to perform any shear test using this samples. Anyway, this set up has a huge potential to perform thermomechanical tests at high temperatures and large deformations. Hence, bigger sample dimensions ensuring a proper heating should be studied to definitely confirm its validity.

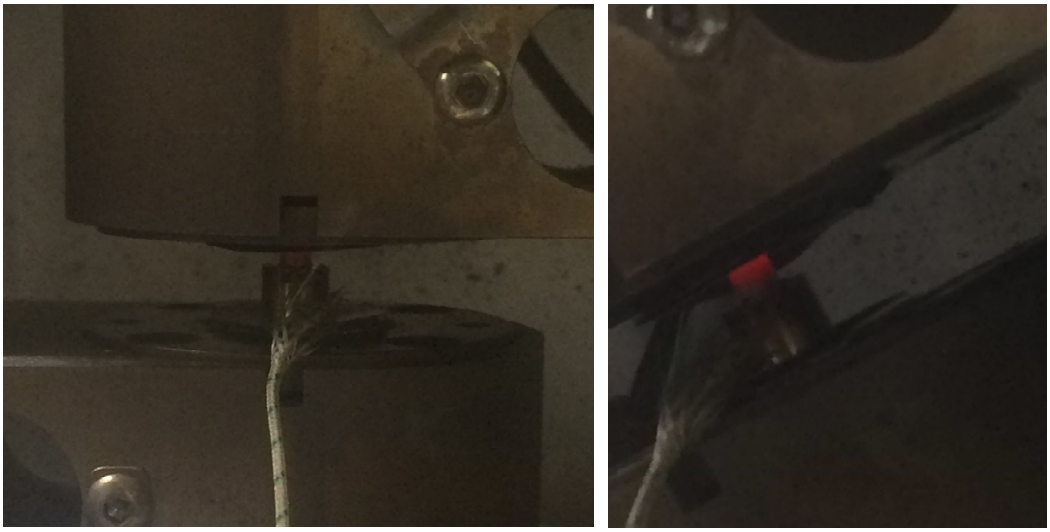

(a) **(b)**

Figure 4.43 – Shear sample heating in the Gleeble HDS-V40 equipment.

4.4.4. Conclusions

After studying the adiabatic heating influence on the Invar 36 at temperatures close to its solidus, it can be said that, even if low, there is a temperature increase. Since it has been recorded after low sample deformation and huge heat loses, everything suggests that higher temperature raises can be attained by increasing the strain rates during larger deformations.

As mentioned, the strain rate increase will help on minimising the cooling at the same time that it will increase a little the amount of plastic stress. However, to increase the plastic work, larger plastic deformations must be achieved. Hence, a combination of both could create the required energy to overcome the solidus temperature.

This can be analysed by using the modelled shear experiment. Even if the tested geometry was not appropriate for Joule heating, by resizing it to higher dimensions maintaining the same shear zone section, this problem can be overcome. Despite the test validity is not confirmed yet, it still has a high potential to obtain proper information at those experimental conditions.

All in all, the adiabatic heating at these temperatures is a reality. However, it is not clear yet its influence as it is not known the required amount of deformation to surpass the solidus temperature. If this deformation agrees with those attained during the process, the adiabatic heating would start being a strong possibility and further investigations should go in the direction of how this hypothetical phase transformation happens.

4.5. Concluding remarks

This chapter has been devoted to shed light on how the observed softening phenomena could have been created. As the initial guess was the generation of liquid, different analyses have been carried out to observe any sign of incipient melting, grain boundary softening and even a strong self-heating.

Incipient melting phenomena

The incipient melting analysis of the 42CrMo4E steel grade consisted of different tests to examine and relate the liquid generation to the observed deformation behaviour. After their performance, it was concluded that no incipient melting happened as there were no liquid signs during the in-situ observing of the material while melting until temperatures close to the solidus measured by DSC were reached. This steel grade was supplied after quenching and tempering and, therefore, the material composition was highly homogeneous avoiding any segregation that could lead to some lower melting point liquid creation. Therefore, the obtained results mean that the incipient melting is definitely not the main driving phenomena of the softening observed in the material at the studied conditions.

However, a clear softening was observed during tensile and compression tests at temperatures close to the components manufacturing one (1360°C). This means that the material is suffering a softening that enables the grain decohesion. If the grains lose their cohesion, it means that the breakage has been produced through the grain boundaries. As this steel and all previously analysed materials have a great amount of sulphur and, indeed, this element is related to the creation of a fragile grain boundary, its influence has been analysed.

The influence of sulphur

The same 42CrMo4 steel grade has been studied with different sulphur contents: low, medium and high. During quenching experiments, it was observed how the sulphur forms MnS sulphides instead of segregating to the grain boundaries. Moreover, those MnS were already present in the as supplied state. Hence, they were not created during heating.

It was also seen how at higher sulphur contents longer contraction cracks were created, which could imply that the MnS precipitates act as crack initiators or propagators. Nevertheless, during SSF components with each grade, no load difference was noticed. This means that even if this can have an influence on the steel deformation behaviour, it is not great enough to assume it as the reason for the observed material flow capabilities. Therefore, and considering that this process involves an extrusion-like deformation creating a great amount of plastic deformation, the influence of a hypothetical self-heating has been studied.

Adiabatic heating

The influence of the generated plastic work on how it suddenly heats up the temperature of the deformed zones of the sample has been analysed. It has been observed how this phenomenon is a reality even if the recorded increases were around 10°C, still low to observe any severe softening effect. However, the experiments were carried out at a moderate strain rate ($10s^{-1}$) and small strains (a true strain of 1). The obtained results and the theory behind this phenomenon seem to agree in the suggestion that larger strains and faster rates would mean a greater heat generation and lower heat dissipation.

In order to confirm this hypothesis, a shear sample has been designed to reach large strains. It was modelled ensuring a homogeneous deformation that could be successfully related to the generated equivalent strain. However, it failed when heating up as it was so small that any tolerance discrepancy makes a huge effect on Joule heating. In any case, it still seems to be the most suitable tests to analyse this phenomenon and, therefore, a sample resizing should be carried out to confirm or deny the influence of adiabatic heating.

Summary of the chapter

This chapter has dealt with three different phenomena. The incipient melting, defined as a primary melting of grain boundaries due to a lower melting composition, is not the reason for the observed material behaviour in the 42CrMo4E. The sulphur has shown its influence on making the material more

brittle but still not enough to enable a material flow close to what it has been observed during the process. Lastly, it has been confirmed the temperature increase at these conditions due to adiabatic heating. However, the performed tests do not resemble the process' conditions and, hence, further experiments are needed to observe its real effect.

Chapter 5

MICROSTRUCTURE EVOLUTION

"Science never solves a problem without creating ten more"

George Bernard Shaw

Summary

Even if there are many hypotheses, no one is still confirmed to be the reason why the material behaves as it does during the SSF process. It is hard to relate what is through in theory with what is happening in reality. This chapter is intended to try to shed light on this by taking advantage of an austenitic alloy to observe how its microstructural behaviour has been during the SSF process.

In an attempt to analyse the microstructural evolution during the SSF process, an austenitic steel that does not have any phase transition from working to room conditions has been utilised. In this case, an alloy 28 stainless steel has been the selected material to manufacture a component via SSF for its subsequent microstructural analysis taking advantage of a micro-XRF equipment, a microhardness tester and optical and SEM microscopes. The outcome of this study does not confirm the driving phenomena that soften the material during SSF. However, it will show the influence of the incipient melting on this specific alloy to enhance the fluidity of the material. Moreover, it will also prove the generation of huge deformations that could imply the existence of adiabatic heating.

5.1. Introduction

If the microstructure evolution during conventional SSF at very high solid fractions is controversial, it is even more at the studied conditions. There, the amount of liquid through the material, if any, is not known. Therefore, many doubts are generated about how the deformation pattern could be.

The complexity of observing the microstructural behaviour at high temperatures is the major obstacle to this end. Direct observation of the material at these conditions are reduced to a very few and special machines with different drawbacks.

One of the options is high-temperature microscopes. They are suitable to observe the evolution of the material during heating and cooling, as used in the previous chapter to analyse the incipient melting of the 42CrMo4E steel grade (see section 4.2.6). However, even if they have the possibility to deform in-situ the material, the work conditions of this accessory are usually below the temperatures this work handles [110].

The other option is the X-ray techniques. There are not many facilities that fulfil the working conditions [111,112] and a great expertise is required to work on this state of the art technologies. Most of them are based on beam absorption that detects density differences to construct the image. This is, in fact, the main issue with this kind of equipment as the steels this work deal with have a really small density difference between phases to enable the material observation.

Consequently, the in-situ analysis of the material has been neglected as a possible technology for this PhD. This fact made us focus on how to obtain the highest amount of information from a post-mortem analysis. This is why, in an attempt to analyse the material microstructure after SSF to identify the possible generated deformation phenomena, an austenitic steel will be used for component manufacturing as it ensures no phase transition during material cooling. In the following lines the material, demonstrator manufacturing and microstructural results are shown.

5.2. Material

It is clear that if the microstructural analysis of a component is aimed, it must be manufactured with a material that enables its study. In this case, an austenitic alloy that does not have any phase transformation from ambient to working

temperatures is also required for this test. To do so, the Alloy 28 austenitic steel has been selected (Figure 5.1).

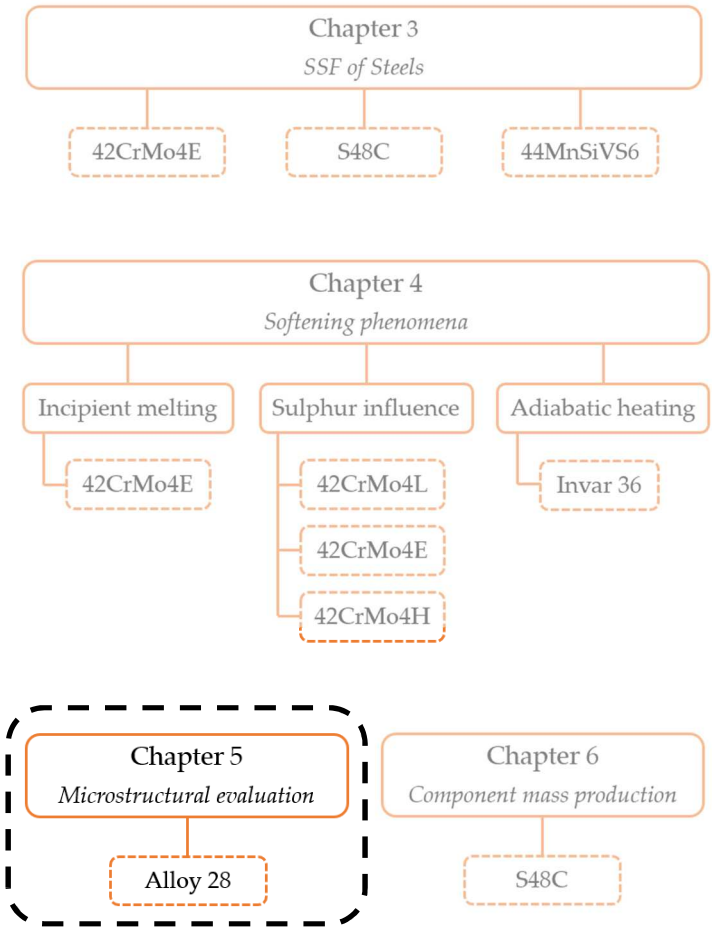

Figure 5.1 – Selected steel for the experimental procedure of the Chapter 5.

The Alloy 28 (UNS N08028) is a special austenitic nickel-iron-chromium alloy with additions of molybdenum and copper. As a consequence of its high resistance to corrosion, it is commonly used in nuclear power plants, oil and gas piping and chemical processing. If sound components are made, this will not only mean that this technology could be used in other fields, but also that nickel alloys can be as well deformed, which are indeed very complex to forge. The chemical composition of the alloy is shown in the following table.

At this point, the aimed working temperatures for this material should be defined. To do so, it is very important to analyse when it starts to melt. As this temperature is not crucial and will only be a reference value to select the heating cycle, thermodynamic calculations taking advantage of FactSage© software will

be used. In the following figure (Figure 5.2) the equilibrium solidification behaviour of the alloy 28 is shown.

Table 5.1 – Chemical composition of the Alloy 28 steel grade.

C	Mn	Si	P	S	Cr	Mo
0.01	1.38	0.31	0.013	<0.005	27	3,75
Ni	**Cu**	**Ti**	**Nb**	**V**	**Al**	
31.2	1.04	0.05	0.03	0.07	0.013	

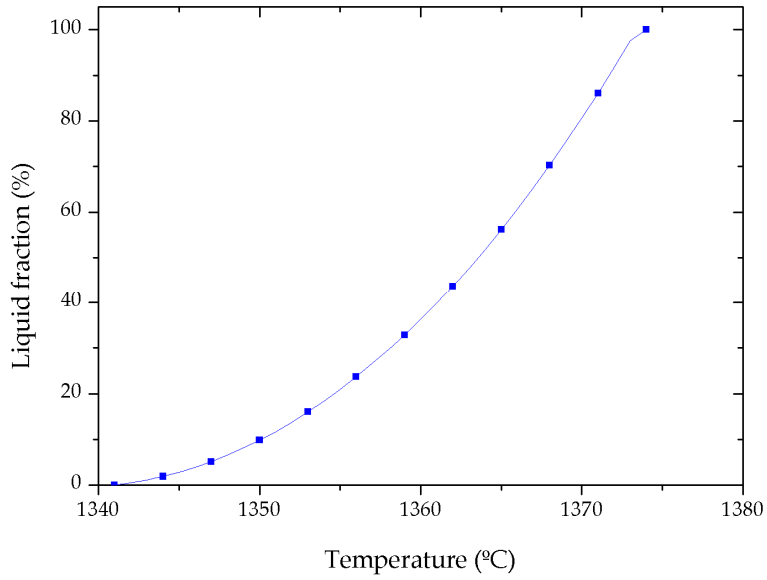

Figure 5.2 – Equilibrium solidification curve calculated with FactSage© software.

As it can be observed in the Figure 5.2 temperatures above 1341°C will imply the existence of some liquid. The material completely melts at 1374°C according to these calculations. Therefore, the selected working temperature should be below 1340°C.

5.3. Demonstrator manufacturing

The manufacturing of a component with an austenitic steel seems to be the most reasonable experiment to attain interesting information from the

microstructure. However, a steel like the alloy 28 is not easy to work with. In this case, most of the nickel-based alloys have a considerably high strength at high temperatures. Therefore, high loads are guessed to be required for a proper deformation. This may mean the requirement of heating up to temperatures close to the solidus one to make it softer. Consequently, thermomechanical tests will be carried out in the material to observe the stress evolution against temperature. Then, the geometry and heating cycle that will be used is explained. Lastly, the results from the SSF process are shown.

5.3.1. Thermomechanical tests

The performance of hot compression tests is important in terms of gaining the knowledge about how the thermomechanical behaviour of the material is. In this case, it is still unknown the relation between the observed stress against strain curve and the capability of the material to be subjected to the SSF. Nevertheless, it is actually known the strength of the 42CrMo4E steel grade when it was manufactured. Therefore, there is a sign of which stresses should be looked for in order to have more chances to have a safe test.

In this case, in the same fashion as in section 4.4.2, compression tests with the same samples and set up will be performed in the HDS-V40 Gleeble equipment of the University of Warwick (Figure 4.29). Three different temperatures will be tested: 1100°C, 1200°C and 1280°C. The choice of those temperatures lies on the wish to observe the material behaviour difference at a wide temperature window. In this case, the maximum reached temperature is 1280°C as the sample started sticking to the anvils. In all the cases a strain rate of 10s-1 has been defined. The true stress against true strain results are shown in Figure 5.3.

It must be noted that due to the dendritic composition of the sample the deformation was not homogeneous. In this case, only at 1280°C, the sample was quite circular. In the rest of the cases, the material deformed randomly. Therefore, the shape of the curve may not be completely real.

In any case, it can be observed the great yield strength this material has even at high temperatures. At 1280°C, a temperature only 60°C below the theoretical solidus, a maximum stress of around 125 MPa has been recorded. This is the double of the maximum stress recorded in 42CrMo4E at 1360°C. Hence, the heating must be designed to obtain temperatures of close to 1320°C in order to increase the possibilities of success when performing the SSF process with this alloy.

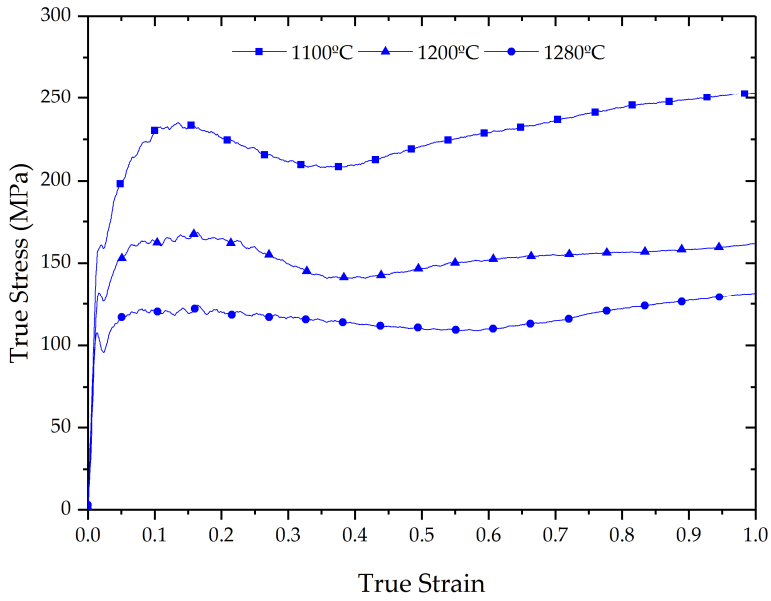

Figure 5.3 – True stress against true stress results after compressing the alloy 28 at a strain rate of $10s^{-1}$ at 1100°C, 1200°C and 1280°C.

5.3.2. Geometry

The aim of manufacturing this demonstrator with an austenitic steel is simply the obtaining of interesting information about how the microstructure has evolved during the process. In this case, if the component complexity is higher, it will mean a much more difficult material flow, which could imply most severe microstructural changes and, hence, an easier identification of created phenomena. Therefore, the H spindle geometry (see section 3.4.1) will be the selected component.

5.3.3. Heating cycle

As it has been mentioned previously, the heating cycle must be designed in such a way that high enough temperature through the billet is ensured to increase the chances to success when manufacturing. Comparing the thermomechanical tests of Alloy 28 and 42CrMo4E, it seems that for the austenitic steel temperatures closer to the solidus should be set. Therefore, the heating cycle will be designed to attain temperatures around 1320°C.

Temperature evolution analysis

The analysis of the temperature evolution during heating has been carried out using thermocouples and a thermal camera. This way, temperatures of the surface, mid-length and close to the centre are recorded. For this task, billets of 65mm of diameter and 93mm long have been used. Two type R thermocouples with ceramic coverings are placed into two 4mm diameter and 43mm deep holes at 8mm and 24mm from the centre of the billet (Figure 5.4).

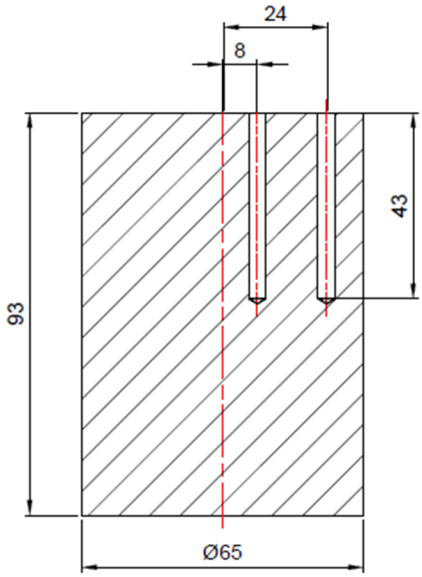

Figure 5.4 – Schematic illustration of the billet size and thermocouple location.

To avoid a huge discrepancy of the emissivity value when analysing the surface temperature with the thermal camera, a high temperature and high emissivity coating has been applied. The selected paint is the Aremco HiE-Coat™ 840-MX ceramic-based black pigmented coating. It withstands a constant exposure to temperatures up to 1316°C and peaks of even higher temperatures. The emissivity values of the product at different temperatures for different wavelengths are stated in [113] (Figure 5.5).

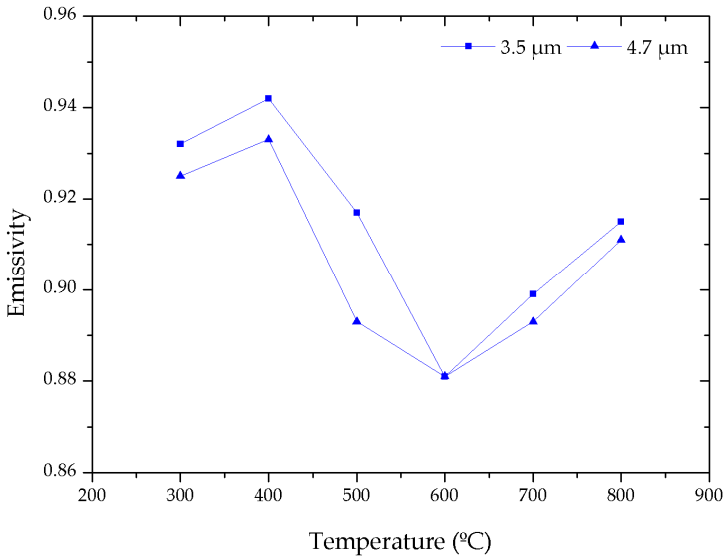

Figure 5.5 – Emissivity values of the coating at different temperatures for 3.5 and 4.7μm wavelengths [113].

The used thermal equipment is a FLIR Titanium 550 M with 360x256 InSb detectors (pixels) and a sensitivity (Noise Equivalent Temperature Difference or NETD) of 20 mK. This camera is actually equipped a narrow-band filter in the IR spectral range of 3.97-4.01 μm. Therefore, the emissivity of the material must be defined for this last parameter. In Figure 5.5 the values closer to the camera's conditions are shown.

Looking at those values it can be assumed that the emissivity value would be situated around 0.92±0.03. In any case, it is hard to guess how the emissivity would change over 800°C. Therefore, temperature calculations in the areas close to the thermocouples position would be analysed by using 0.89, 0.92 and 0.95 values to observe the temperature difference depending on the emissivity.

Heating cycle's design

Looking at Figure 3.3 (see section 3.3.2) it can be seen how temperatures slightly higher than 1330°C are achieved in an LTT C45 steel if the last heating step is removed. Considering the compositional and microstructural differences between this and the Alloy 28, lower temperatures are guessed in the last case. Therefore, the first heating trial will be performed with the same heating cycle but removing the last heating step. The following figure (Figure 5.6 (a)) shows the recorded temperature with the thermocouples while heating.

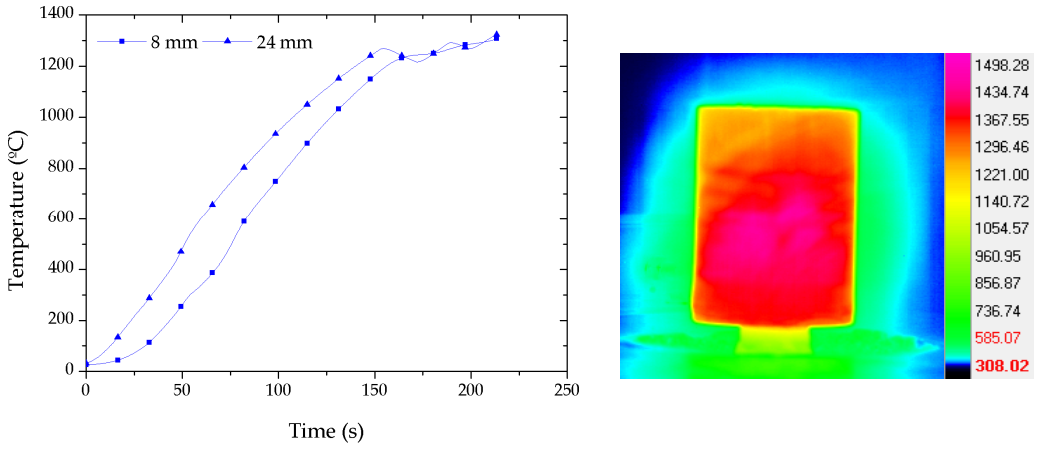

(a) **(b)**

Figure 5.6 – (a) Temperature evolution during heating measured by thermocouples at positions 8mm and 24mm far from the centre of the billet and 43mm depth. (b) Thermal image of the surface of the billet just after opening the oven.

It can be observed how the temperature in the middle of the billet is quite homogeneous at the end of the heating reaching a maximum temperature of 1325°C which perfectly fits the aimed working temperature for this SSF trial. In Figure 5.6 (b) the temperature of the surface of the billet just after the oven opened is shown assuming an emissivity of 0.92. To have a rough idea of the temperature change of the surface from the upper to the downer areas, the temperature of different points through the length of the sample has been recorded (Figure 5.7).

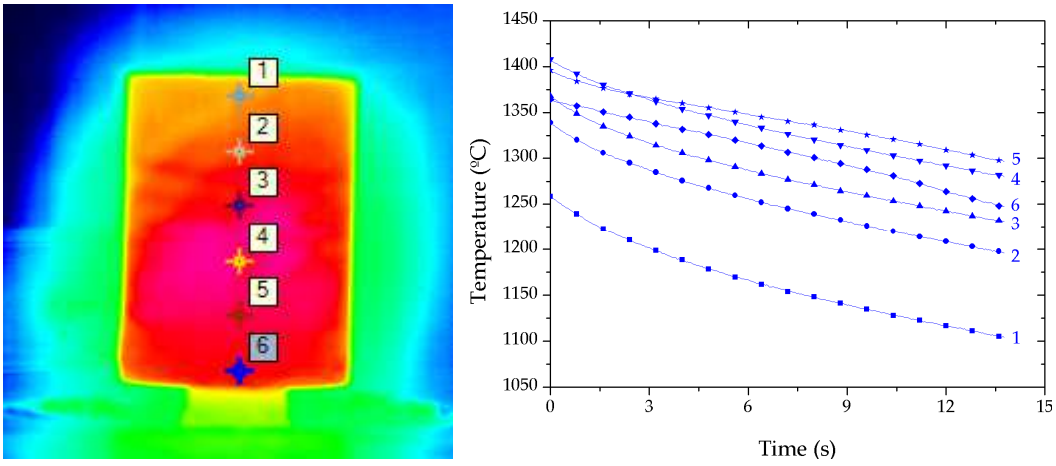

(a) **(b)**

Figure 5.7 – (a) Tracking points location in the billet. (b) Tracking points temperature evolution during cooling just after the heating.

This data clearly shows the temperature inhomogeneity there exists between the upper and bottom zones. In addition, the skin effect can be appreciated as temperatures over 1400°C are presumably reached in some areas of the middle length of the sample even if a couple of millimetres inside the sample only 1325°C are measured. In any case, it is worth remembering that the emissivity value was 0.92 for those images. To observe the error in terms of temperature that a minimal change of emissivity can imply, temperature calculations with different emissivity values will be compared. In this case, the tracked point is the one located close to the depth where the thermocouples are placed. This will enable a comparison between those values and will also help to analyse the skin effect. The resulting cooling curves are shown in the following figure (Figure 5.8).

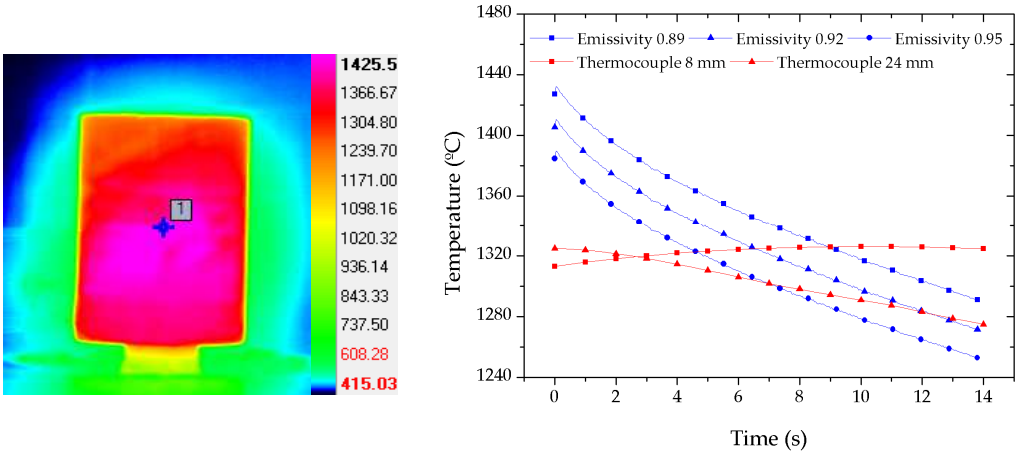

(a) **(b)**

Figure 5.8 – (a) Tracking point location in the billet. (b) Temperature recordings during 14s cooling after the heating cycle for thermal data assuming 0.89, 0.92 and 0.95 emissivity values and thermocouples.

First of all, it is clear that a minimal change in emissivity means a difference in temperature. In this case, a change of 0.03 in emissivity implies a 30°C difference. Therefore, it is hard to define an accurate surface temperature of the material. Nevertheless, even assuming the highest emissivity, temperatures close to 1400°C are attained in the central part of the billet, which means around an 80°C difference from the recorded temperature with the thermocouple closer to the surface (skin effect).

Assuming that the robot needs around 12-14 seconds to place the billet in the tooling, the temperature of the material in the middle and bottom zones still is 1325°C in the centre but near 1280°C in areas close to the surface. In the case of the top surface (Figure 5.7 (b)), the temperature seems to be greatly lower being around 1160°C the measured value in the very top areas. Bearing in mind that the

heating in all the previously studied cases for SSF has been made with the same oven, this temperature inhomogeneity does not seem to be an issue.

5.3.4. Component manufacturing

The component manufacturing by SSF has been carried out following the steps explained in section 3.3. After the analysed heating cycle, the robot took the billet and placed it into the tooling. Then, the press moved down deforming the material until it abruptly stopped due to an overload recording (more than 380t were achieved). The following figure shows the shape of the obtained component after moving back the punch and opening the tooling (Figure 5.9).

(a) **(b)**

Figure 5.9 – Manufactured component with alloy 28 austenitic steel.

It can be appreciated how the material has not filled completely the cavity. It filled the central axle but it did not the last part of the lateral cavity. However, a huge back extruded flash can be observed. This happens due to an improper state of the copper ring located in the punch that is the responsible for preventing this flash from creating. It seems that this flash is, in turn, the reason for overloading. It is guessed that if a proper copper ring is installed, this could be avoided and the material will fill the cavity without any problem.

In any case, the flowing capabilities of the material seem to be quite great looking at the generated flash. Note that the punch contacts the colder area of the billet (the top part). This could mean that even having lower material temperatures, the material is still capable of successfully flowing through such a small section like the gap between the punch and mould (around 0.3mm).

However, looking at the material that stopped flowing, a severe grain decohesion seemed to happen (Figure 5.10). This could mean that a really brittle grain boundary or even liquid was generated during heating and/or deformation.

Figure 5.10 – Observed severe grain decohesion in the areas where the flow stopped.

5.3.5. Conclusions

The main conclusion is that the Alloy 28 steel grade can be subjected to SSF. It seems that the studied conditions are excessive and, hence, lower temperatures should be tried to avoid this grain decohesion which is associated to liquid generation or brittle grain boundary and, at the same time, is harmful as it could create internal defects.

Initially, it was thought that due to the high strength of the material, its deformation was going to be tricky. However, it deformed properly if it was not for the deteriorated copper ring. Moreover, the material temperature is inhomogeneous after heating that does not seem to be an issue to flow correctly as the flash of less than 1mm was generated with a colder material (according to the thermal camera it was around 1200°C).

Regarding the heating, it has been observed the inhomogeneous temperature distribution through the billet this oven implies. Around 80°C difference was recorded between the surface and the thermocouple placed a couple of millimetres far from the surface. However, after letting the material to air cool for 12-14 seconds, the temperature of the surface decreases really quickly and only the areas close to the centre of the billet are capable of maintaining the attained target temperature. It was also observed the importance of calibrating properly the emissivity as it can lead to a huge temperature difference that, at the studied conditions, could mean the expectation of liquid or not.

All in all, the alloy 28 steel has been properly subjected to SSF even with a huge material temperature inhomogeneity and a deteriorated copper ring that did not work as it was expected. Now is high time to observe how the microstructure has evolved during the process. The following section will go into it to try to shed light on how and why the material has flowed.

5.4. Microstuctural analysis

This section is devoted to observe and analyse the material at a micro-level trying to find any clue of how and why it has been deformed. To do so, different analysis like micro X-Ray fluorescence, optical microscopy, microhardness and SEM has been carried out. In the following lines, the obtained results are shown.

5.4.1. Micro X-Ray fluorescence

The aim of using an austenitic steel is based on having the chance to attain information from the post-mortem material. However, it is hard to know in advance which are going to be the most interesting zones to analyse. Therefore, a compositional analysis of a half of the component has been performed in order to observe areas of interest.

To do so, it has been used the Bruker 2D Micro-XRF M4 Tornado equipment of the University of Warwick. It enables attaining compositional and element distribution information down to a 20μm resolution of quite large parts as it has a sample chamber of 200 x 160 x 120mm. The following figure shows the compositional distribution of the component (Figure 5.11).

It can be clearly observed the initial dendritic composition of the alloy. The dendrites (light blue) have a lower concentration of Mo than the interdendritic region (darker blue). This dendritic distribution seems to be lost after the material deformation. In the axle, for example, once the material goes through the first extrusion, the dendritic shape is broken even if there still are composition inhomogeneities.

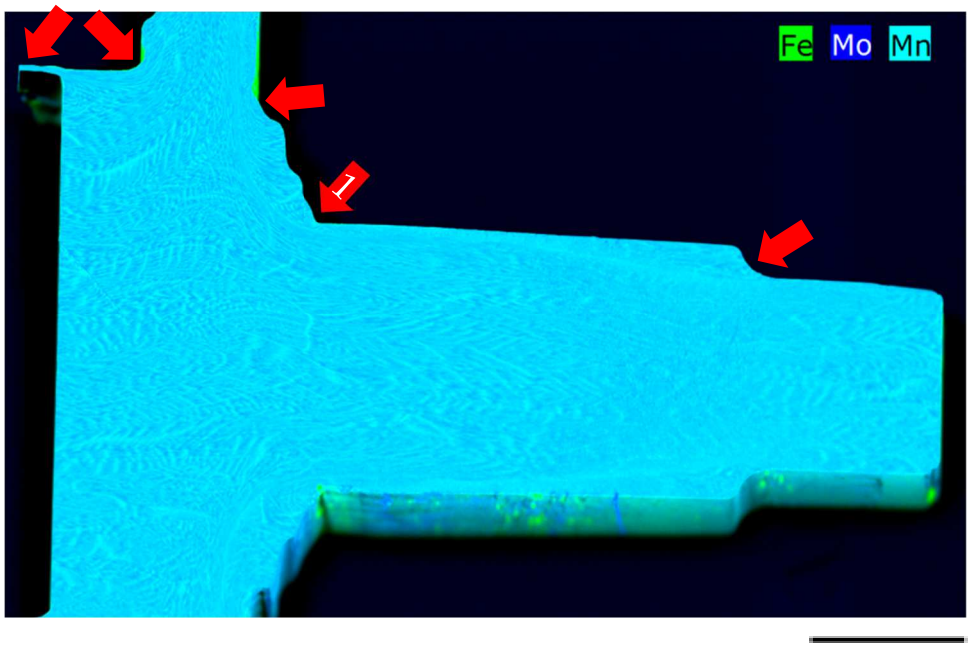

Figure 5.11 – Micro-XRF map of a half slice of the component showing the dendritic composition. Hatched zones are strained areas. Scale bar: 20mm.

The marked zones in the figure mean the areas where the highest deformation has happened as the composition is quite orientated into what seem to be some flowing bands. The locations coincide with the corners where an extrusion-type deformation has been developed.

Looking closer to the first extrusion corner (the arrow marked with a "1" in Figure 5.11) one can appreciate even more clearly the generated composition distribution change (Figure 5.12). While the area close to the surface seems to be almost no deformed, a couple of millimetres inside a heavy and clearly orientated deformed region is found.

Looking at those images, all suggest that in this zone something has happened as the microstructure has evolved differently. Therefore, in the following steps, the analysis will be focused on this specific corner in order to clarify why the observed difference has been generated.

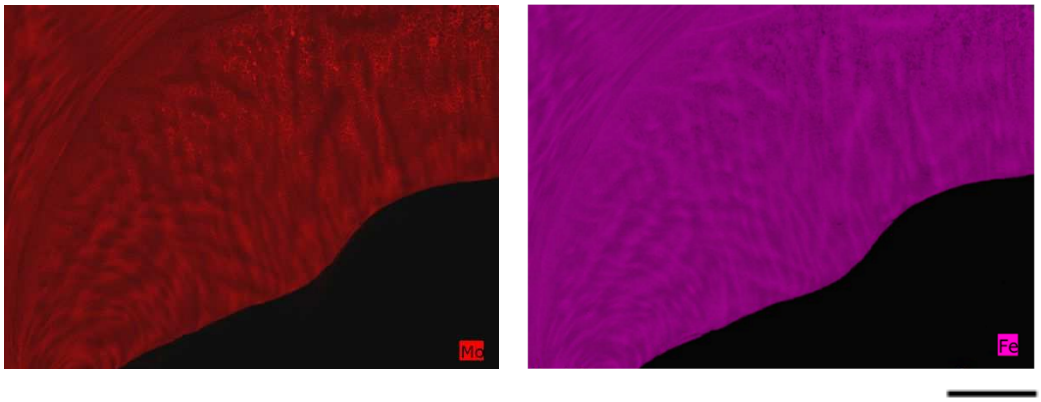

(a) **(b)**

Figure 5.12 – Compositional micro-XRF map of the first extrusion corner (marked with a "1" in Figure 5.11). (a) Interdendritic region rich in Mo and (b) dendritic region rich in Fe. These images have been rotated 90° to the right from Figure 5.11. In this case, the axle should go in the bottom of the picture. Scale bar: 2mm.

5.4.2. Optical microscopy

The first step to analyse the area of interest is to see the microstructure with an optical microscope. For that, this zone has been cut, mounted, grinded and polished. Then, the sample has been etched with the Kallings Nº2 etchant for several seconds to reveal the austenitic grain boundaries. In the following figure, its microstructure can be observed (Figure 5.13).

In the microstructure, it is clearly visible the grain size difference between the surface and the guessed flow line. This suggests that the grains have been recrystallised presumably due to the deformation they have been suppressed to and, therefore, they have reduced their size. In contrasts, in the area of the surface, it seems that the material has been placed there under almost no forces and, therefore, the microstructure is quite similar to the as supplied (Figure 5.14).

Figure 5.13 – Optical microstructure montage of the corner. Same direction as Figure 5.12. Scale bar: 2mm.

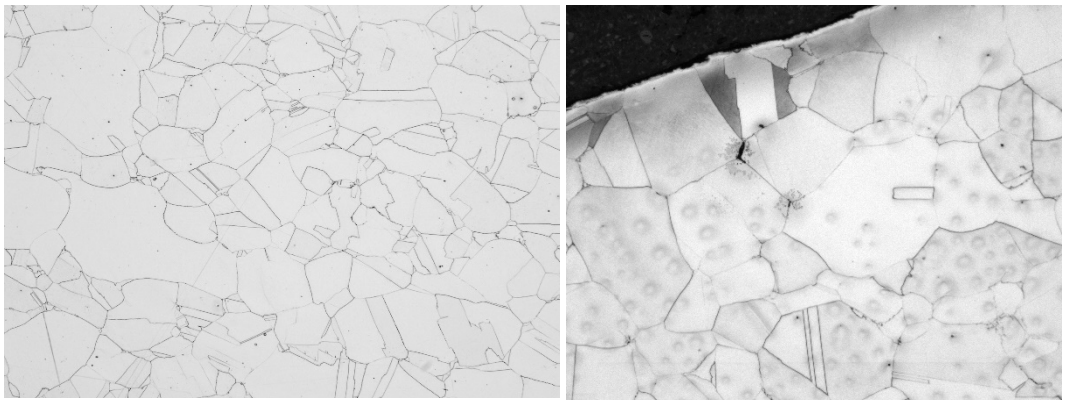

(a) **(b)**

Figure 5.14 – (a) As-supplied microstructure of the Alloy 28 and (b) microstructure of the surface of the analysed corner. Scale bar: (a) 400μm and (b) 330μm.

In areas closer to the heavily strained region it can be observed how little grains surround the big ones (Figure 5.15 (a)). Some of those big grains seem to be

stretched. In the case of areas closer to the flow line, it seems that a full recrystallization has been developed (Figure 5.15 (b)).

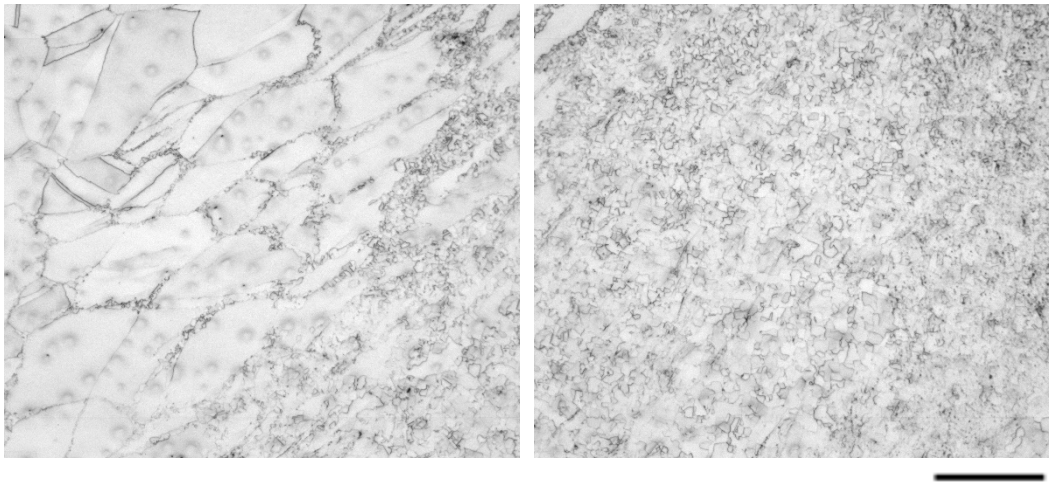

(a) **(b)**

Figure 5.15 – Image of the microstructure (a) in between the surface and the flow line and (b) close to the flow line. Scaler bar: 400μm

Looking at this, the recrystallization phenomena seem to have happened at different levels and, therefore, the effect of strain is clearly visible. It is also clear that some liquid was present in the material as some pores are detected in areas close to the surface of the axle (Figure 5.16).

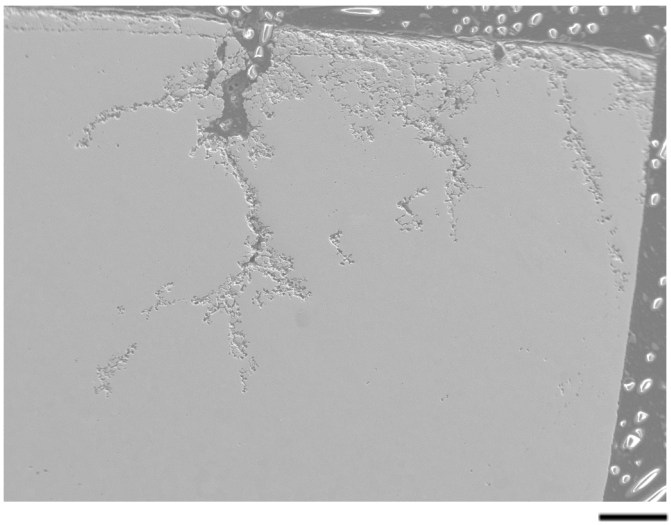

Figure 5.16 – Microstructure image showing cracks and pores in the surface of the axle. Scaler bar: 100μm.

However, this information is not enough to confirm any driving phenomena that explain the material behaviour. Therefore, in order to attain more information about the state of the material, a micro-hardness map will be carried out through the sample.

5.4.3. Microhardness

This microhardness test is intended to relate the hardness to the microstructure. To do so, the Buehler Wilson® VH3100 Vickers hardness tester of the University of Warwick has been used. It enables the performance of a range of indentations through the selected area after recognising the sample boundaries. In the following figure (Figure 5.17) the acquired hardness map using a 300g indenter and 250µm spacing between indents is shown.

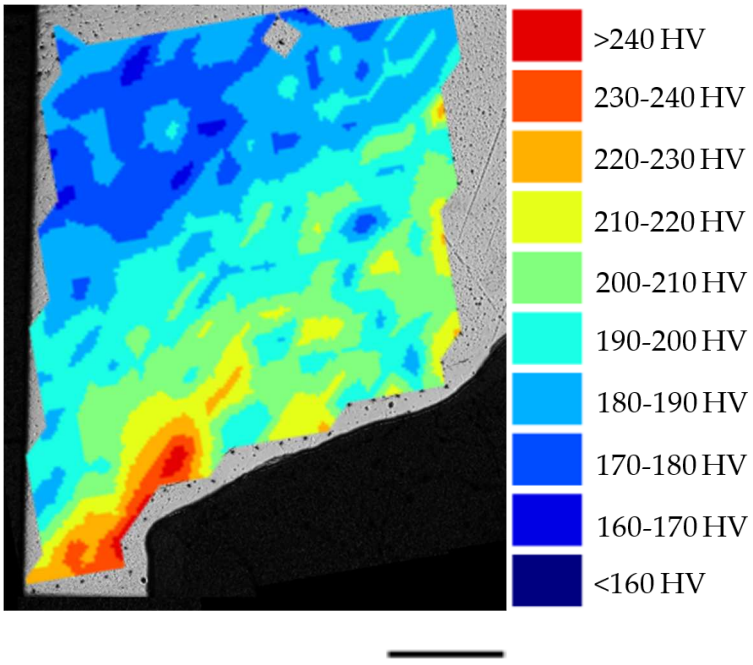

Figure 5.17 – Micro-hardness map of the corner. The sample direction is the same as in Figure 5.13. Scaler bar: 2,5mm.

As it can be observed in the lower corner, where the extrusion happens, the material is very hard due to the guessed strain hardening. It is higher close to the surface as the friction seem to play an important role. In the rest of the areas, it seems like the hardness decreases going far from the surface. Nevertheless, as the indents spacing is quite high, it is hard to relate this hardness map to any specific reason and accept it as reliable. Consequently, in order to try to obtain values at a

lower spacing to attain a more precise hardness map, a little area from surface until the flow line has been tested with a 100g indenter and 150μm spacing (Figure 5.18).

The obtained map shows quite interesting information. It can be seen how the hardness in the areas close to the surface is between 190-220 HV, lower than in the surface itself as due to friction the hardness increases to values between 210-230 HV. Going deeper through the sample the hardness starts to increase until the mid-length between the flow line and surface. There, hardness values between 220-250 HV are achieved. In the areas closer to the flow line, a hardness drop is noticed (<200 HV). Moreover, some very soft locations of hardness values around 150 HV are noticed.

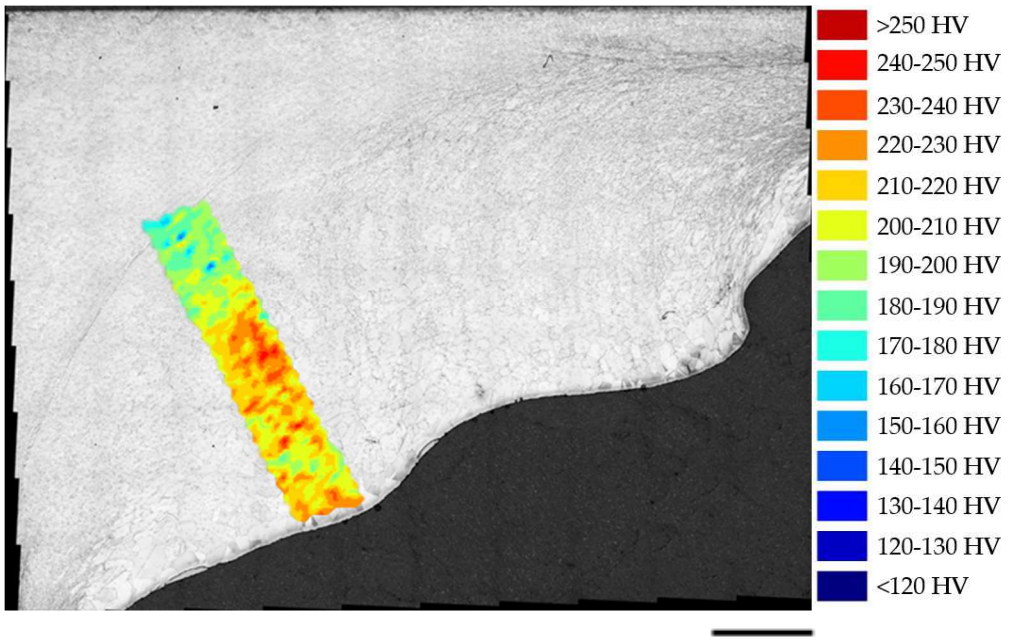

Figure 5.18 – Image of the micro-hardness map from the surface until the flow line over the etched microstructure. Scale bar: 2mm.

The increase of the hardness on the very surface could be due to the influence of friction. In the areas closer to it the hardness could be lower as it seems this zone does not have almost any deformation on it. At deeper sections, the hardness could have increased due to strain hardening in those grains that were not able to recrystallise. Lastly, from this last zone on, the deformation is guessed to have been great enough enabling the recrystallisation to happen and, therefore, to decrease the hardness of the indented grains.

These results seem to strengthen the influence of strain on the observed material. However, even if it can be observed its obvious influence, it is still hard to conclude exactly what went on. In order to acquire more information, a deeper

compositional analysis will be carried out to see whether there is any sign of segregation.

5.4.4. SEM analysis

A compositional analysis of the areas of interest has been carried out in a FEI NovaNanoSEM 450 Scanning Electron Microscope (SEM) equipped with an Oxford X-max 50 X-Ray detector. The zones that will be analysed are shown in Figure 5.19.

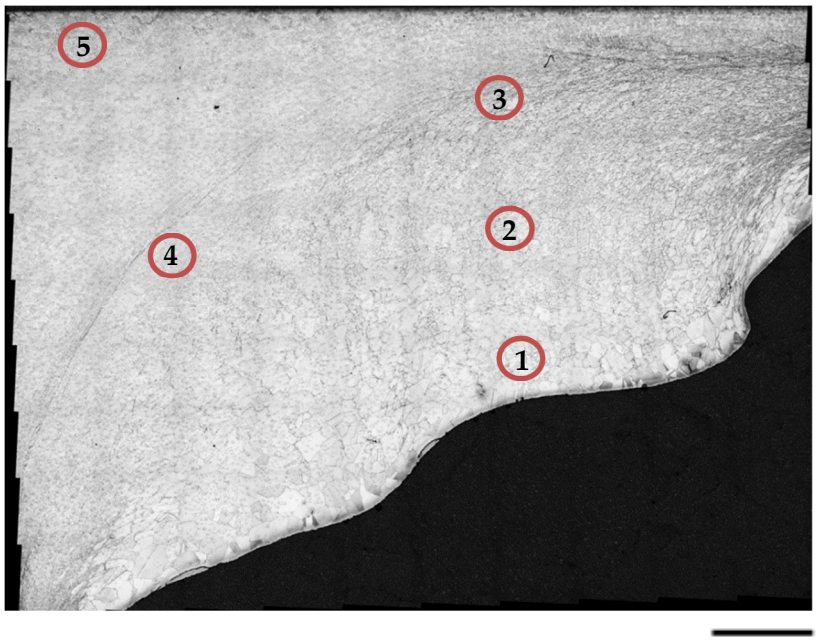

Figure 5.19 – Location of the analysed microstructures on the SEM. Scale bar: 2mm.

The first location is the area close to the surface where the material seems to be almost not strained and quite similar to the as-supplied. The second location is an area between the highly strained zone and the surface. The third is a severely strained area of the sample. The fourth location is the observed flow line. Lastly, the fifth is an area over the most strained zone that does not seem to be excessively strained. In Figures 5.20-5.24, the compositional analysis results are shown.

After analysing those areas, it is confirmed the segregation of Molybdenum which is related with the existence of liquid. This segregation is generated in locations 2, 3 and 4 while in locations 1 and 5 a homogeneous element distribution is noticed.

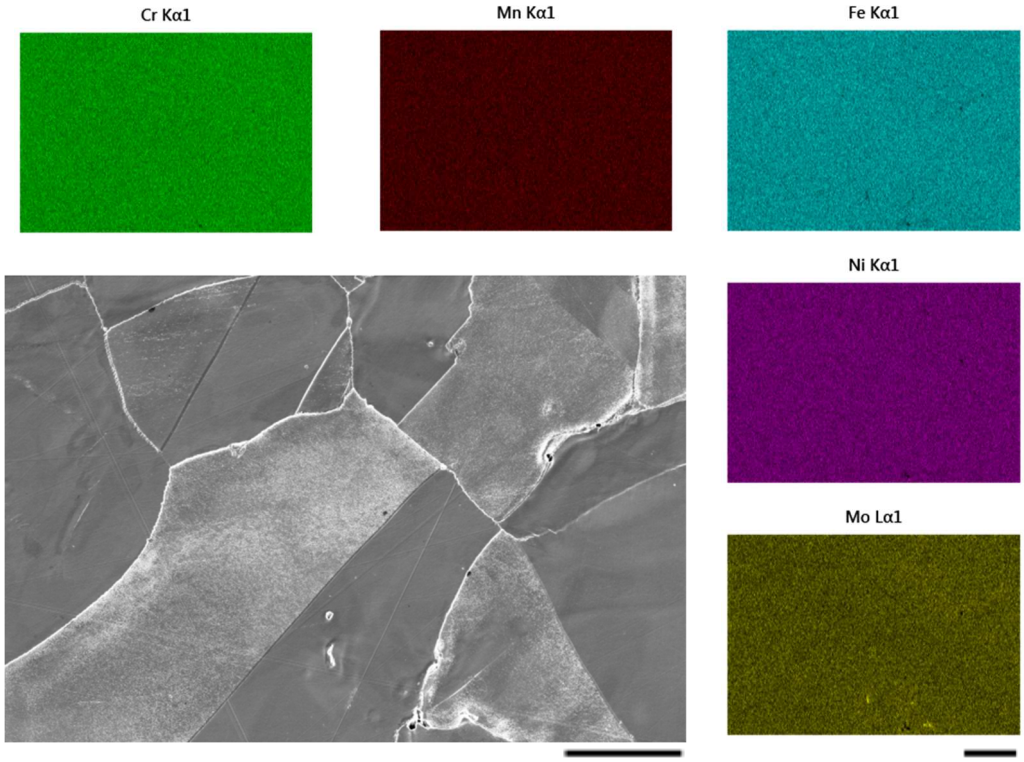

Figure 5.20 – Microstructure and composition of location 1 in Figure 5.19. Scale bars: 100μm.

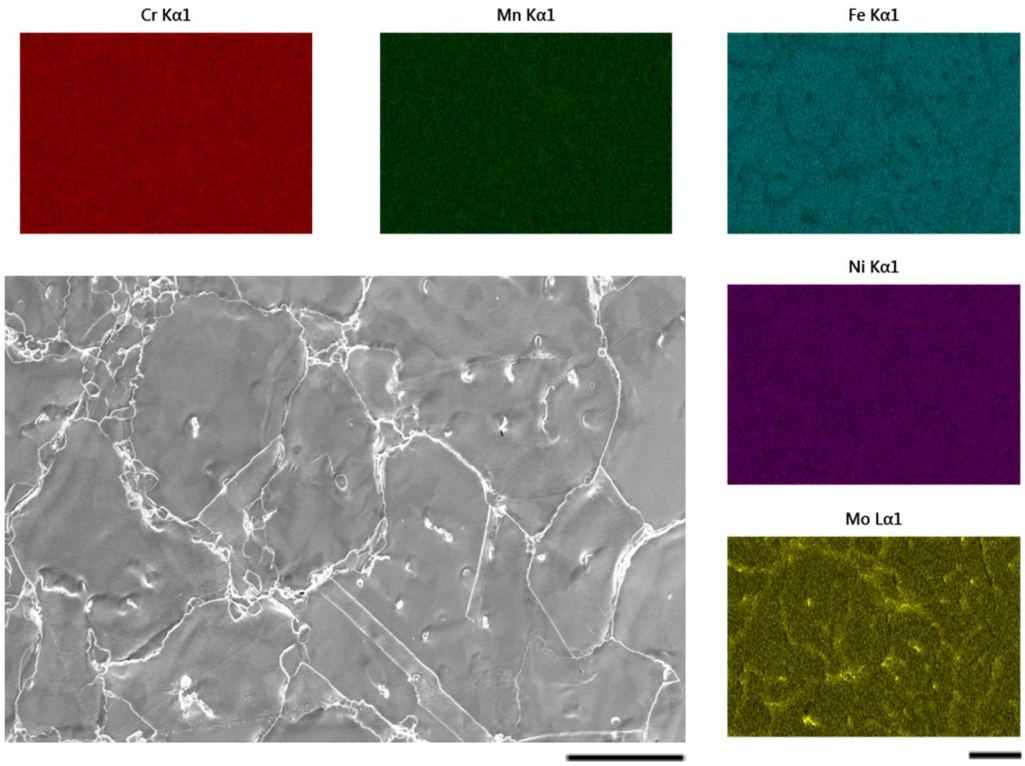

Figure 5.21 – Microstructure and composition of location 2 in Figure 5.19. Scale bars: 100μm.

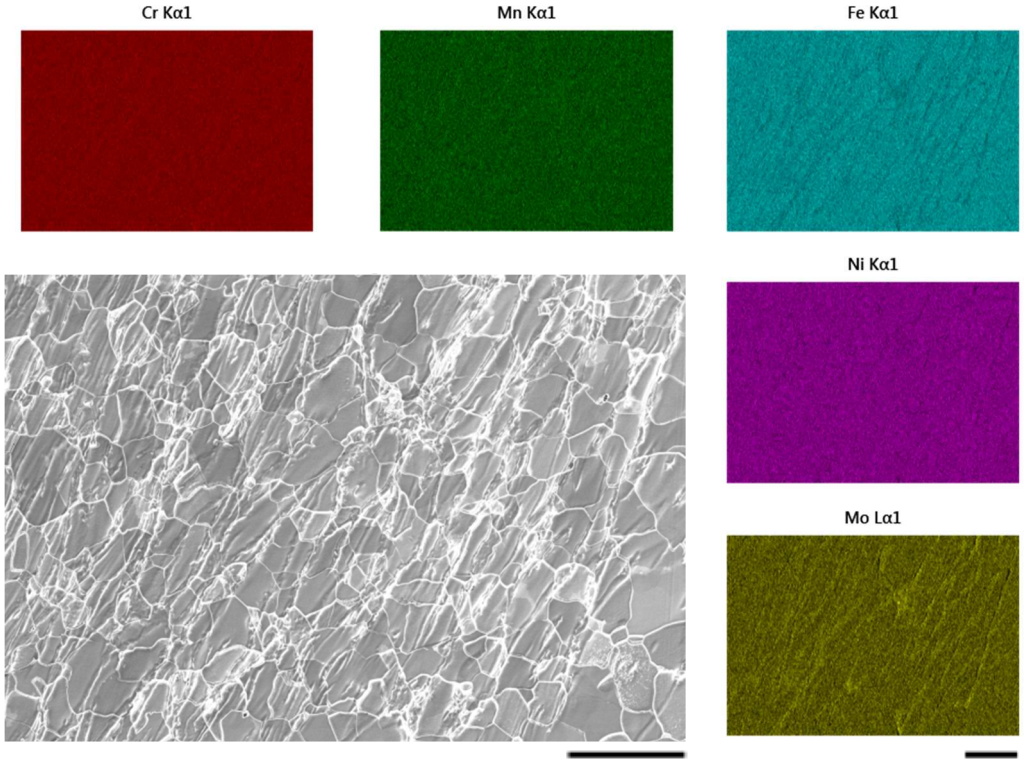

Figure 5.22 – Microstructure and composition of location 3 in Figure 5.19. Scale bars: 100μm.

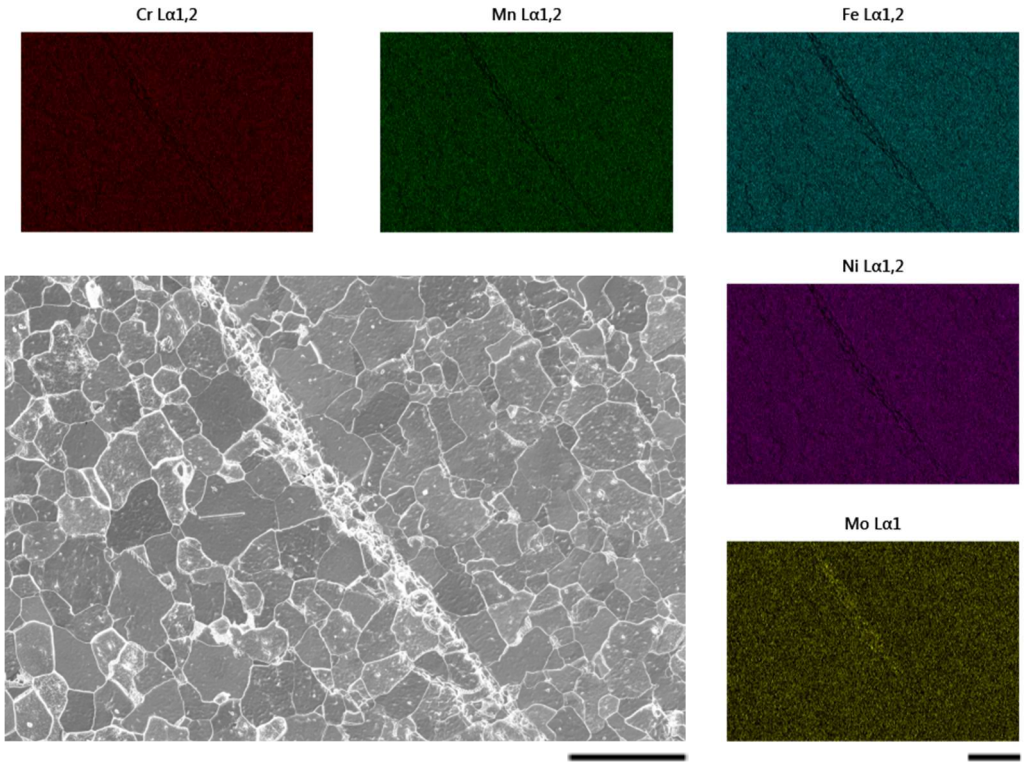

Figure 5.23 – Microstructure and composition of location 4 in Figure 5.19. Scale bars: 100μm.

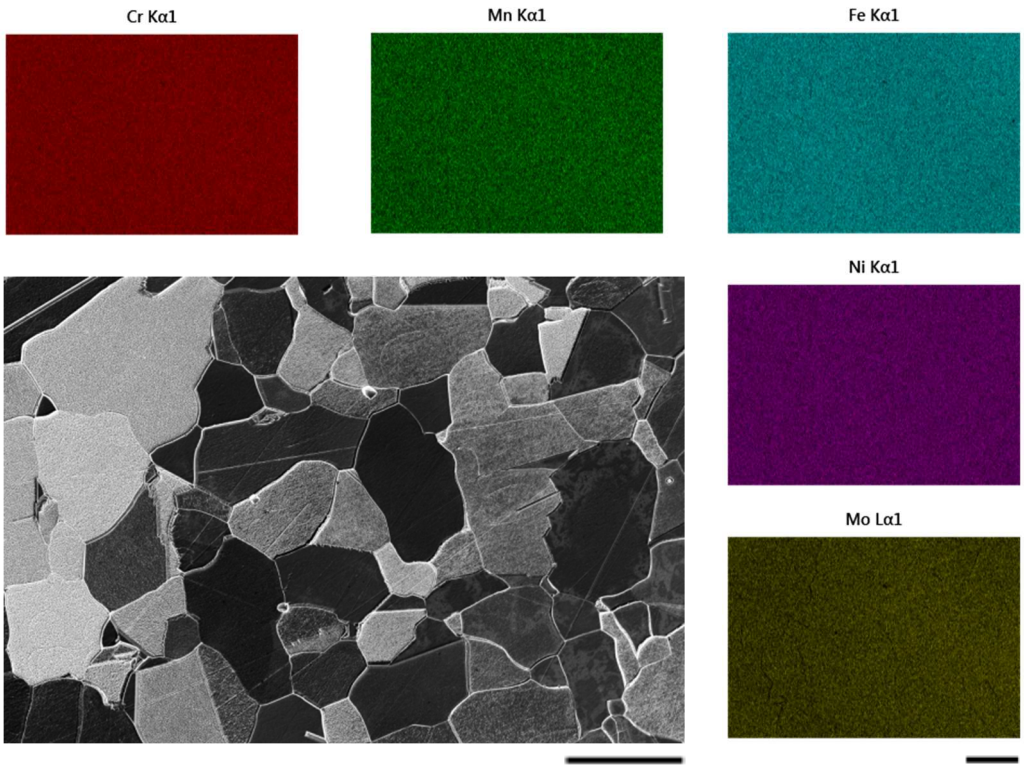

Figure 5.24 – Microstructure and composition of location 5 in Figure 5.19. Scale bars: 100μm.

The deformation degree on the material is guessed to influence how it develops. In the case of location 2 (Figure 5.21), the Mo segregation seems to agree with the grain boundary of the microstructure. This could suggest the existence of liquid along the grain boundary that enables the microstructure deformation driven by grain sliding. This way, even if the grain has been elongated, the sliding could have prevented the dynamic recrystallisation of the grain from happening. That could explain the greater hardness values obtained in this area.

In location 3 (Figure 5.22), as higher deformations have been generated, the microstructure is completely different. In this case, the Mo segregation does not agree with the observed grain boundaries. However, the Mo distribution shape looks like the grain boundary of a severely elongated grain (Figure 5.25). This could have happened similarly to the guessed for location 2 but, in this case, the severe strain the material has been subjected to made the grains to recrystallise even if they were hypothetically sliding and elongating. This could explain why the composition and microstructure do not agree as it does in location 2 as well as the recorded drop in micro-hardness.

In location 4 (Figure 5.23) there is a strong and localised segregation of Mo. There is also appreciable a similar grain refinement like in location 3. The observed segregation line could indicate the existence of liquid that acted as a shear band where most of the deformation is concentrated. This hypothetic phenomenon could have meant that both zones have been sliding between each other enabling a material softening.

In locations 1 and 5 (Figure 5.20 and Figure 5.24 respectively) no Mo segregation is observed. However, the microstructure in location 5 looks like grain refined probably due to dynamic recrystallisation. In any case, these grains are still bigger than those observed in locations 3 and 4. In location 1, as observed optically, the microstructure is very similar to the as-supplied.

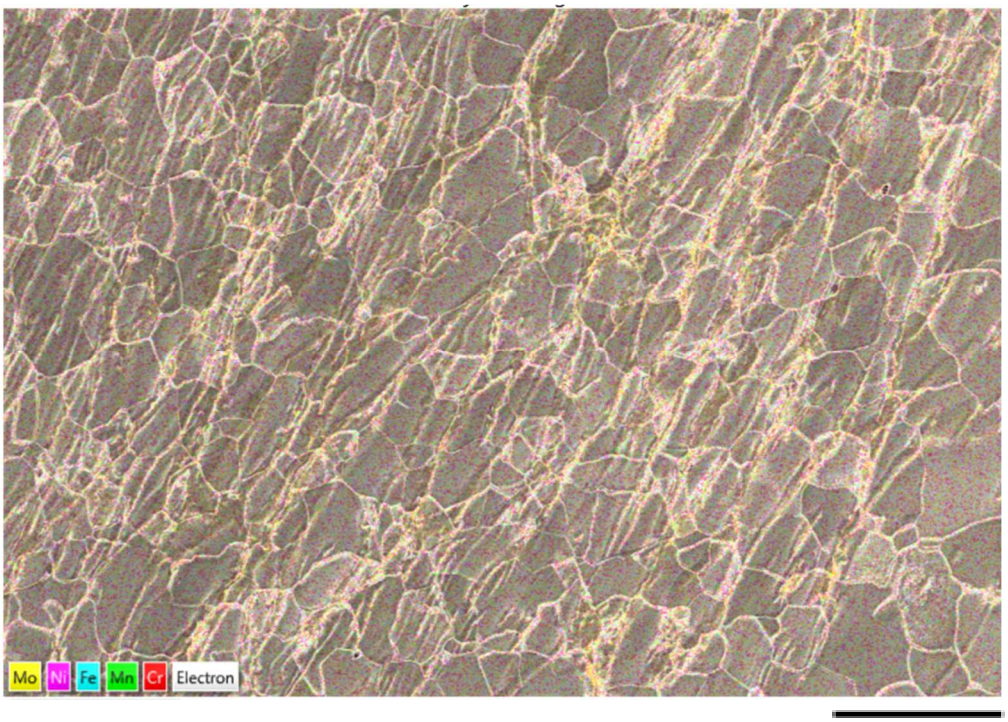

Figure 5.25 – Layered image showing the chemical elements distribution maps over the location 3 microstructure. Scale bar: 100μm.

5.4.5. Conclusions

The main conclusion after the microstructural analysis is the existence of liquid. However, how it has been generated is not completely clear yet and, therefore, it requires further analysis. The effect of strain is also noticed as great grain refinement is observed in different zones. Nevertheless, in the same fashion as before, it is difficult to say the role of the strain on the observed Mo segregation. Hence, at this point, it is hard to relate the gathered information with the driving

phenomena of the material's flow. Moreover, care must be taken when analysing this information as the microstructure is a picture of the last step of the deformation. What it has been observed might not be directly related to what could have been going on during deformation.

With regard to the methodology used to analyse the microstructure, the utilisation of the Micro-XRF equipment saved a lot of time as it enabled the observation of the whole component to detect areas of interest. In the same fashion, the hardness mapping capability helped to understand better the evolution of the microstructure along the sample. This information together with the etched microstructure also facilitated the selection of the most interesting areas to observe in the SEM that enabled the detection of Mo segregation.

To sum up, in this section the material has been analysed using micro-XRF, optical microscopy, hardness mapping and compositional analysis in the SEM. It has been confirmed the effect of the strain on the microstructure and the presence of liquid. However, where could this liquid come from? Based on the previous chapter analysis on the possible softening phenomena, some possible reasons would be suggested in the following lines.

5.5. Suitability of previous hypotheses

In Chapter 4 different phenomena were analysed to observe if its effect looked like the driving phenomenon of the observed material flowing capabilities. However, it was confirmed that for the case of 42CrMo4E steel neither the incipient melting nor the sulphur content was the responsible for the material behaviour. In addition, the confirmation of the effect of adiabatic heating, even if potential, still needs further investigation. However, with the information gathered in this chapter and, more precisely, during the microstructure evaluation, another scenario is presented. In the following lines, the suitability of the incipient melting and adiabatic heating on the observed phenomena will be discussed.

5.5.1. The possible effect of incipient melting

The incipient melting happens when the material is not homogeneously distributed through the sample. As it was noticed in the micro-XRF (Figure 5.11) there is a compositional difference between the dendrites and interdendrites. In this case, a higher amount of Mo is found in the interdendritic region as this element tends to be present in the last liquid entrapped between dendrites. This happens due to the low diffusivity of Mo that makes it impossible to dissolve again into the dendrites. This increment of Mo means the lowering of the solidus

temperature and, therefore, liquid at lower temperatures may be found (Figure 5.26).

Taking this fact into account, the temperatures recorded in the billet (around 1325°C in the lower area of the billet) seem to be high enough to partially melt this interdendritic phase. This downer part of the billet is indeed the one that contacts with the studied corner. Therefore, if it was liquid rich in Mo already present in the material before the deformation, it could be clear the source of the observed phenomena. However, it is difficult to guess how the material has deformed as the observed microstructure only gives information of the final stage of the process. In any case, the incipient melting phenomenon could explain the ease of deforming the material and the observed segregation in this specific case.

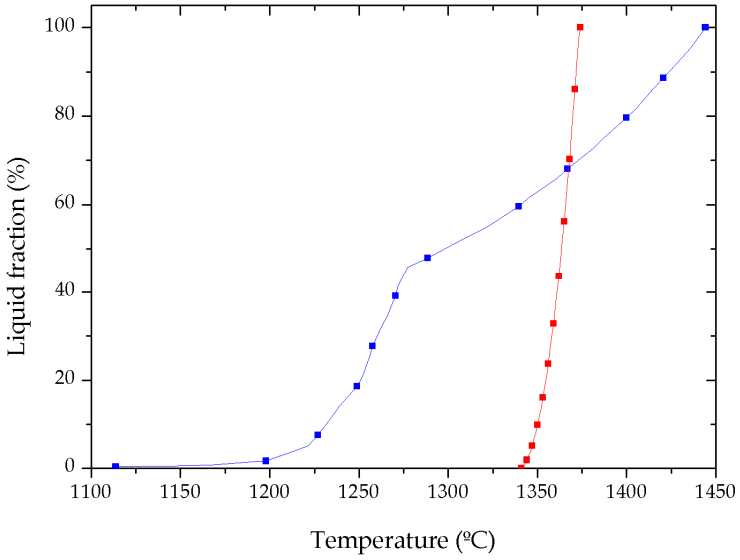

Figure 5.26 – Solidification curves according to calculations using FactSage© for the interdendritic region (blue) and equilibrium (red).

5.5.2. The possible effect of adiabatic heating

In this hypothesis, if it is considered that the interdendritic region is not already melted after the heating, the generated strains could imply the heating up of the deformed regions due to adiabatic heating enabling this phase to melt. This hypothesis could fit with the observed flow line in location 4. There, the strain seems to be even more localised than in the other zones suggesting that this hypothetical liquid could have been created due to the influence of strain in this very specific zone. A rough simulation has been carried out using the DEFORM®

software assuming a friction value of 0.35 and the alloy 28 material flow curve. The result agrees to point out this area as the one with the highest localised strain. Moreover, the registered values of strains seem to be great enough to increase reasonably the temperature in those localised regions (Figure 5.27).

However, it is hard to expect the generation of such a great amount of liquid in the material due to only the adiabatic heating to generate the observed pores. Consequently, its influence is more likely to be related in this case with increasing slightly the amount of liquid or even stabilising the already present one.

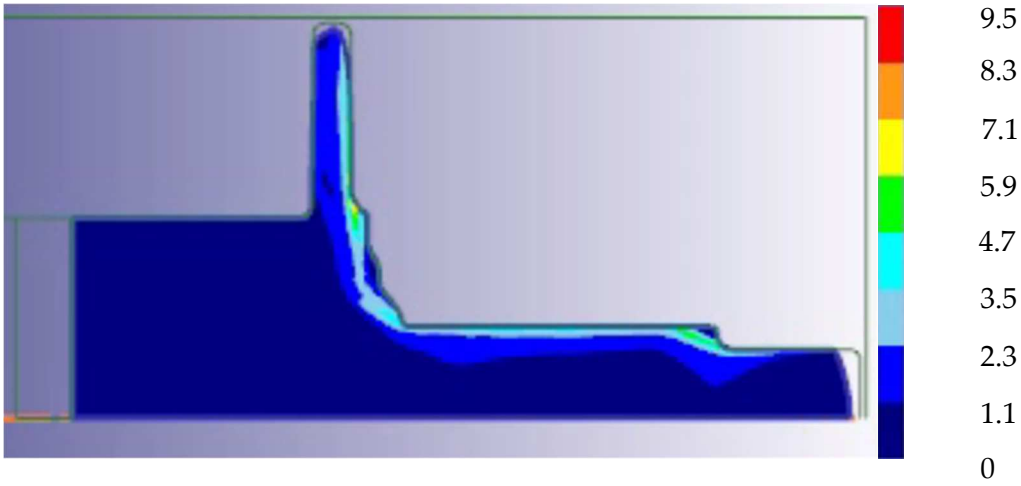

Figure 5.27 – Picture of the simulated strains during the final stage of the material filling.

5.5.3. Discussion

Material behaviour

Looking at all the above, it seems sensible to expect the existence of liquid due to the incipient melting of the Mo-rich regions. The strain distribution during the filling could have had an impact on moving this melted phase through the grains or group of grains making easier its deformation. However, it is just a hypothesis considering the observed microstructure and segregation locations. How the material has evolved during the complete filling is still unknown as the gathered information comes from the last filling stage.

Regarding the adiabatic heating hypothesis, it is still valid. It is true that in this specific case, the adiabatic heating might not be the main phenomenon enhancing

the material softening. Nonetheless, looking at the gathered information, the heavily strained areas seem to be great enough to consider its effect. Therefore, even if the incipient melting is more likely to happen in the observed alloy and conditions, the obtained results do not deny the adiabatic heating influence as it still might have had a partial influence on the observed deformation.

Therefore, it is clear that the incipient melting has had in this case an effect enhancing the fluidity of the material. In any case, as analysed in Chapter 4, the incipient melting has been proved not to be the responsible for the generated softening during sound components manufacturing. Moreover, the pores and all signs of liquid appearance are visible only in areas close to the surface while nothing is appreciated in the bulk. This means that, in this case, even if the incipient melting has helped on deforming easier the material, another kind of phenomena may still be happening at the same time.

Alloy 28 components

The main drawback of having this incipient melting with this alloy is that it is related to the generation of defects. Having in mind the component, at the studied conditions severe grain decohesion as well as pores in areas close to the surface of the axle has been noticed. Consequently, the ideal manufacturing conditions might be located at lower temperatures, maybe at even lowers than the starting temperature of the incipient melting.

However, all the defects have been detected in the very surface of the component. All of them are situated as far as 0.5 mm from the surface. In the rest of the component, no crack or pore is appreciated. This could suggest that even with the requirement of a surface machining and of further investigations to confirm it, the component could still be sound.

It has to be remembered that the alloy 28 is an actual problem for the forging industry. The existence of this lower melting temperature phase asks for lower working temperatures during forging. This, as shown during the compression tests, means a considerable increase in the stress required to deform the material. Moreover, the compositional difference is also a problem in terms of the mechanical behaviour of the component.

Consequently, this preliminary test of manufacturing a component via SSF using the alloy 28 could suggest the suitability of this technology to overcome those problems. The fabrication with the compositional inhomogeneity seems to enhance the fluidity of the material without compromising the component health. Then, the compositional difference can be removed subjecting the component to a postprocessing heat treatment.

5.6. Concluding remarks

In this chapter, a component has been manufactured by SSF using an austenitic steel to enable the microstructural evaluation. This has been made aiming to define the phenomena that explains why the material is capable of filling such a complex shape. In the following lines, the most important conclusions are stated.

Component fabrication

With regard to the component fabrication, the main outcome is the ability to deform an austenitic alloy rich in Ni during the SSF. This could lead to widening the applications this process can work for, even more considering that the forging industry is actually having problems with it.

It has also been shown the independence of the process regarding the heating of the billet. The temperature inhomogeneity through the billet does not seem to be a handicap for the SSF process. However, a bad condition of the copper ring enabled the generation of a huge flash that prevented the material from filling completely the cavity. In addition to this, the used temperature meant the generation of grain decohesion which is related to defects. Even though, all the observed defects are accumulated in a 0.5 mm gap from the surface. Therefore, even if lower temperatures should be tried, the observed conditions seem to be capable of obtaining sound components.

Microstructural evaluation

The microstructure evaluation has been successfully carried out using a micro-XRF equipment, a micro-hardness tester and optical and SEM microscopes. Apart from pores, Mo segregation through the grain boundaries and areas where the strain seems to have been concentrated are identified. This segregation is in turn related with the existence of liquid.

Suitability of previous hypothesis

Looking at previous conclusions, it looks like the incipient melting has enhanced the material fluidity enabling a softer filling. The observed strained areas also seem to be great enough to consider the adiabatic heating phenomena. However, the gathered information is not enough to define its influence level. Moreover, no signs of liquid have been detected in the bulk of the material which still suggests that other phenomena are happening enabling the observed material softening.

Summary of the chapter

This chapter has been focused on the fabrication of a component by SSF and its microstructural evaluation to try to identify the reason for the material flowing capabilities. The observation of Mo segregation and pores suggests the existence of the incipient melting of a Mo rich phase that enabled an easier material deformation. The heavily deformed areas also confirm the possible effect of the adiabatic heating although its real influence is still unknown. However, the very localised areas where this has been detected still suggests that other phenomena are happening.

Even if there were defects in the component, those are situated on the very surface. The inner part of the component is defect-free and, therefore, this process may be an option to manufacture components with such complex alloys. In any case, lower temperatures should be tried to definitely avoid the defects generation.

Chapter 6

COMPONENT MASS PRODUCTION

"The science of today is the technology of tomorrow"

Edward Teller

Summary

The information gathered until this point is not excessively practical at an industrial level. There, processing times, costs and repeatability are the most important aspects. This kind of analysis is a step that must be done to catch the attention of companies. Taking this fact into account, a pre-series of a batch of 250 components will be manufactured.

All the components are successfully manufactured without any appreciable severe damage in the moulds. Moreover, the components are sound apart from some lubricant entrapment on the very surface. This is confirmed by testing some samples taken from the axle of the component. The results confirm the equality of properties between the forged and SSF components during tensile and fatigue testing. In addition, the cost reduction in the component price is assessed.

6.1. Introduction

At this point, the SSF has shown the capacity to successfully manufacture sound automotive spindles using different steel grades. Even if it is still not clear the reason of the flowing capabilities of the material to attain such sound parts, this research work has made a first step on showing how to investigate the components to success on the discovery of what is going on.

Nevertheless, from an industrial point of view, this information is not enough to take that step into the industrialisation of SSF. In this framework, the most important questions go aligned with the fabrication cadence, the cycles the tooling will withstand and, of course, to ensure that the components have the required resistance. In order to do so, the manufacturing of 250 components will be tried. This way, not only how many cycles the tooling can resist will be analysed, but also there would be a great number of components to perform different mechanical tests to ensure their validity. Hence, this chapter will be devoted to the fabrication and analysis of those components.

6.2. Manufacturing set up

In this section, the way the components are manufactured is explained. The equipment is the same as described in Chapter 3. The procedure is similar but with some modifications to improve the cadence as the goal lies in manufacturing the first pre-series of 250 components. In the following lines, all the procedure and modifications are explained.

6.2.1. Geometry and material

The selected component for the manufacturing of this batch is the H spindle (see section 3.4.1). Its selection comes from its higher complexity in comparison with the R part. This will mean a higher damage to the mould as it will imply a higher degree of abrasion. Therefore, considering that the forged components are made using this alloy, the selected steel is the S48C (Figure 6.1). The information about the material is stated in section 3.4.3.2.

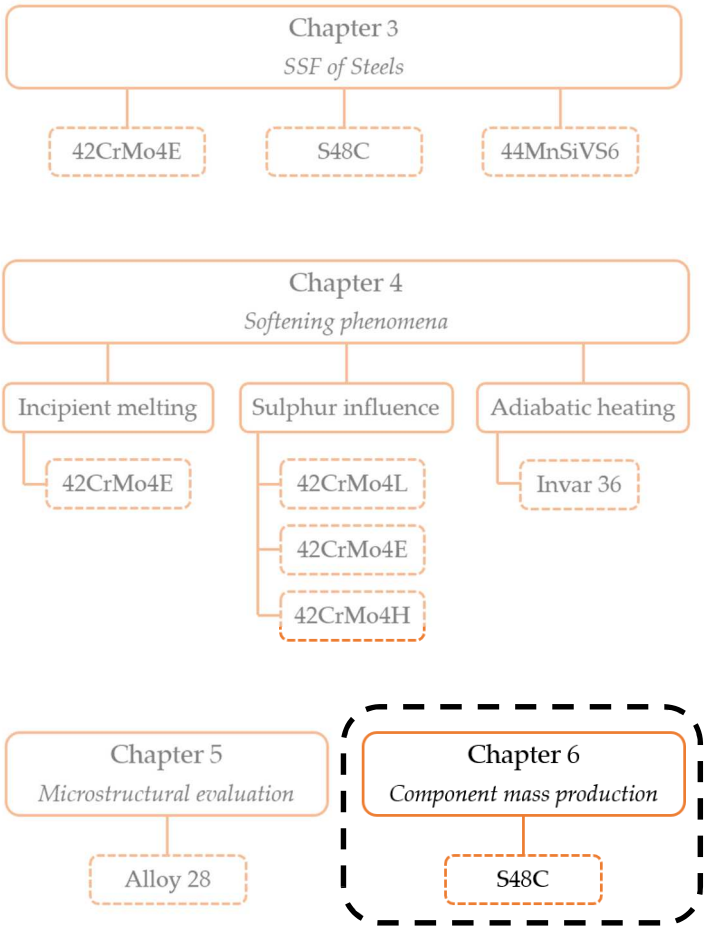

Figure 6.1 – Selected steel for the 250 components manufacturing of the Chapter 6.

6.2.2. Heating cycle

The heating cycle shown in Figure 3.3 (see section 3.3.2) is only valid when the oven is cold. It means that after the first component manufacturing if the same cycle is again utilised, the material will start to melt. Consequently, this cycle must be modified so as to ensure a proper heating of the billet once the oven is hot. This is mainly a cadence issue as the reduction of the process' time is required to show its potential.

In order to do that, five dummy heating cycles have been performed before start trying the cycle for the process. This way, all the trials will be made with a more or less constant initial temperature in the oven. The first trial was made modifying the times of the last heating step of the cycle described in section 3.3.2. There, the billet starts melting before the end of the heating. Thus, the cycle was continued being modified until the proper sample temperature was achieved. In this case, the following table shows the final heating cycle (Table 6.1).

Table 6.1 – Heating cycle steps for the continuous heating of billets to manufacture the 250 components.

Step 1		Step 2		Step 3	
Time	Power	Time	Power	Time	Power
160 s	24 kW	18 s	0 kW	17 s	24 kW

6.2.3. Fabrication procedure

As mentioned before, when preparing everything for this batch manufacturing, attaining the best cadence was the main goal. This timing was optimised by designing this continuous heating cycle that avoided the necessary cooling the previous one required. In addition, the tooling modifications explained in section 3.2.4 also enabled a faster and safer tooling opening, closing and clamping.

However, the installation is in a laboratory environment which implies that the automation of the cell still needs further improvements to reach the industrial cadence. As an example, the induction equipment is only capable of heating one billet at the same time. All in all, the time guessed to obtain one component is 8-10 minutes. The following table shows the expected time for each procedure (Table 6.2).

Table 6.2 – Expected times for the different stages of the process

Process stage	Time (s)
Heating	207
Transfer	12-14
Deformation	10-12
Component ejection	60-90
Cleaning and preparations	190-280
Total	**480-600**

The component ejection, cleaning and preparations for the following component manufacturing are made manually. That is why a wide time interval is guessed. This timing does not consider any deviation due to the failure of the

component of the cell. In the following section, the most important aspects of the fabrication of the 250 components are explained.

6.3. Fabrication of 250 components

Observed defects in the components

The fabrication of the 250 components using the SSF process has been successfully carried out (Figure 6.2 (a)). The geometry has been properly filled apart from some imperfections in the edges due to CeraSpray® entrapment (Figure 6.2 (b)). This can be easily overcome by machining some escape holes in the dies. Even so, those imperfections do not represent any problem for the mechanical performance of the component. In contrast with the observed grain decohesion during the SSF of the alloy 28 (Figure 5.10 , see section 5.3.4), this component shows a really smooth filling front and does not exhibit any grain decohesion (Figure 6.3). In addition to this, neither cracks nor pores are observed.

(a) **(b)**

Figure 6.2 – (a) Picture of the fabricated batch and (b) small imperfections due to Ceraspray® entrapment (a).

Figure 6.3 – Picture of a component fabricated stopping the process before the cavity was completely filled.

Observed damage in the dies

The dies do not exhibit excessive damage after the pre-series batch. Only sharp and thin edges around the two circular pins show wear (Figure 6.4). In any case, this minor problem can be solved with a simple geometry redesign. Apart from some oxide adhesions and flowing scratches on the surface of the dies, they withstand the requirements of the process without any problem.

(a) **(b)**

Figure 6.4 – Pictures showing the areas of the component where local wear of dies is appreciated.

Process improvements

During the manufacturing of the components, several improvements have been noticed. It is clear that this cell needs a higher automation level to reach the industrial cadence. However, this last requirement is more focused on investing in new equipment to reach these levels. Consequently, only those upgrades that could affect the health of the component and that could put in risk the benefits this process gives will be explained.

First of all, and as it has been mentioned in Chapter 3, the clamping force is extremely important to ensure a proper closing of the dies. It has been shown that if the clamping system does not close and fix properly the moulds, the material tends to flow between them generating the undesirable flash and preventing the material from completely filling the component (Figure 6.5). Therefore, care must be taken when performing the clamping or designing and installing the clamping system.

(a) **(b)**

Figure 6.5 – Pictures of (a) a sound component and (b) a component manufactured with a lower clamping pressure.

In addition to this, the shape of the guide to ensure a proper position of the moulds when closing must be properly designed. In this case, its height was not enough and it was not properly working in all the attempts. In order to prevent this from happening, some "L" shaped components have been installed in both upper and lower dies and die holders to ensure a proper closing guidance (Figure 6.6).

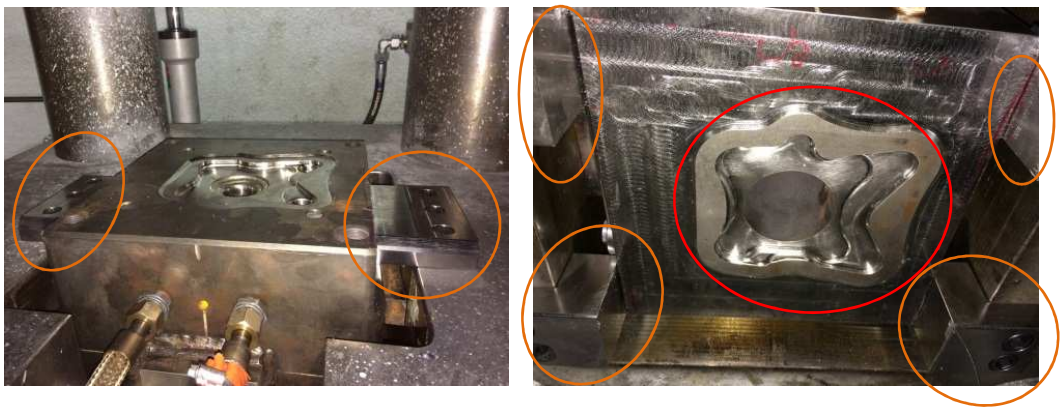

(a) **(b)**

Figure 6.6 – Pictures of (a) lower and (b) upper moulds with the "L" shaped parts to ensure a proper mould closing. Highlighted red zone: manufactured guide on the mould. Highlighted orange zones: "L" shaped parts.

6.4. Mechanical properties

The industry requires reliable results to start considering the implementation of a new manufacturing route. This implies the necessity of showing same or better results in terms of resistance than conventional manufacturing processes. In this case, the HF is the most directly related process. Therefore, the mechanical properties of both SSF and HF components will be tested and compared. However, the HF components are subjected to a quenching and tempering treatment so as to meet the required hardness and mechanical resistance. Therefore, the SSF components have been as well subjected to the same heat treatment. Moreover, in order to enhance the performance of the SSF components, the following optimised heat treatment has also been applied to several components (Figure 6.7):

The attained hardness is shown in Table 6.3. Then, to make the mechanical tests, 15mm diameter cylinders are taken from the axle of the component to machine the tensile and fatigue specimens for the subsequent testing. In the following lines, the performed mechanical tests on the samples taken from the SSF and HF components are explained.

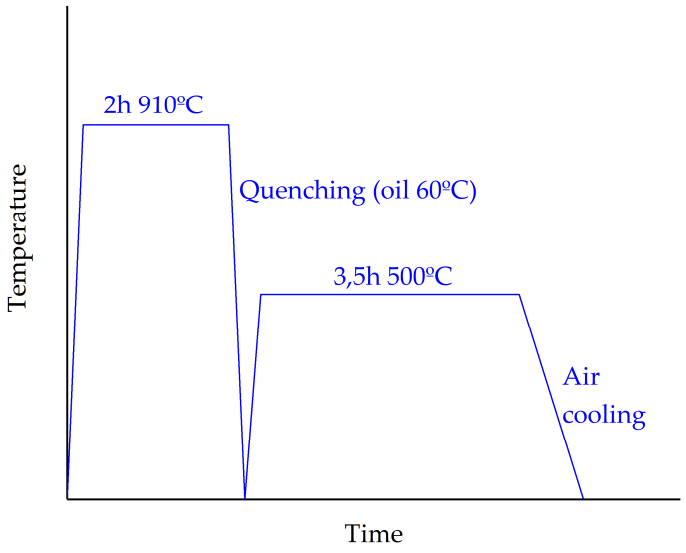

Figure 6.7 – Schematic illustration of the optimised heat treatment cycle the S48C components have been subjected to.

Table 6.3 – Measured hardness in HF and SSF components.

Sample	Hardness Brinell (HB)
HF	248
SSF	241
SSF_treat	235

6.4.1. Tensile tests

The uniaxial tensile test is the most widely used mechanical experiment to acquire information about the strength and ductility of materials. This standardised method enables a direct comparison between differently fabricated samples or even samples of different materials. In this case, as mentioned before, the samples are machined from a cylinder taken from the axle of the spindle (Figure 6.8). Both the utilised sample's geometry and the experimental procedure are according to the ASTM E8M-09 standard.

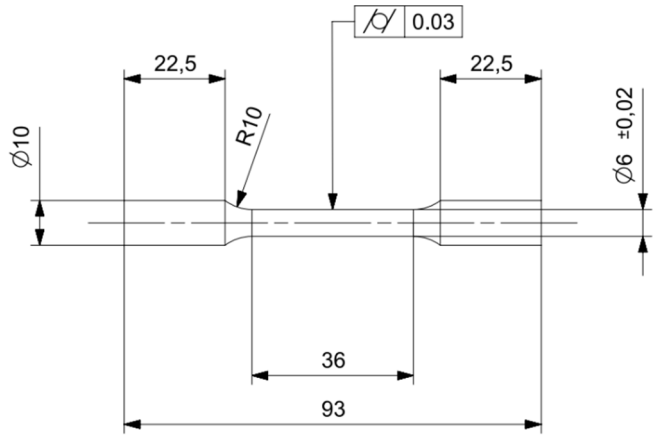

Figure 6.8 – Schematic illustration of the geometry of the tensile specimen according to the ASTM E8M-09 standard.

In order to have a direct comparison and overview of the resistance difference between HF and SSF components, some samples are also machined from forged components and subjected to the uniaxial tensile test. In the following tables (Tables 6.4-6.6), the obtained results are exhibited.

Table 6.4 – Obtained tensile properties results for the HF component.

Sample	Re (MPa)	Rm (MPa)	Elongation (%)
HF1	518	832.6	19.8
HF2	476	796.8	16.7
HF3	486	794.3	13.2

Table 6.5 – Obtained tensile properties results for the SSF component.

Sample	Re (MPa)	Rm (MPa)	Elongation (%)
SSF1	521	794.7	19.8
SSF2	496	764.6	21.7
SSF3	486	749.3	19.9
SSF4	515	793.1	21.9
SSF5	492	762.7	21.7
SSF6	489	751.4	21.9
SSF7	511	781.8	20.6

Table 6.6 – Obtained tensile properties results for the SSF component with the optimised heat treatment.

Sample	Re (MPa)	Rm (MPa)	Elongation (%)
SSF_treat1	553	823	19,6
SSF_treat2	579	826	19,3
SSF_treat3	564	810	20

Looking at these values, it can be seen how the yield and ultimate strengths of the HF and SSF components are pretty similar. However, the SSF components exhibit a higher ductility prior to breakage, which could help on the detection of potential breakage zones in the component prior to its failure. In the case of the SSF components subjected to the optimised treatment, both Re and Rm are increased overcoming the HF results while maintaining the great elongation.

6.4.2. Fatigue tests

According to the ASTM E466-96 standard, the axial force fatigue test is helpful to establish the effects of variations in geometry, surface condition, material and stress, among others, on the fatigue resistance of the alloy for large numbers of cycles. In an attempt to analyse the fatigue behaviour of the SSF components in comparison with the HF ones, some preliminary tests have been carried out using the following sample geometry (Figure 6.9) taken from the axle of the spindles (according to ASTM E466-96):

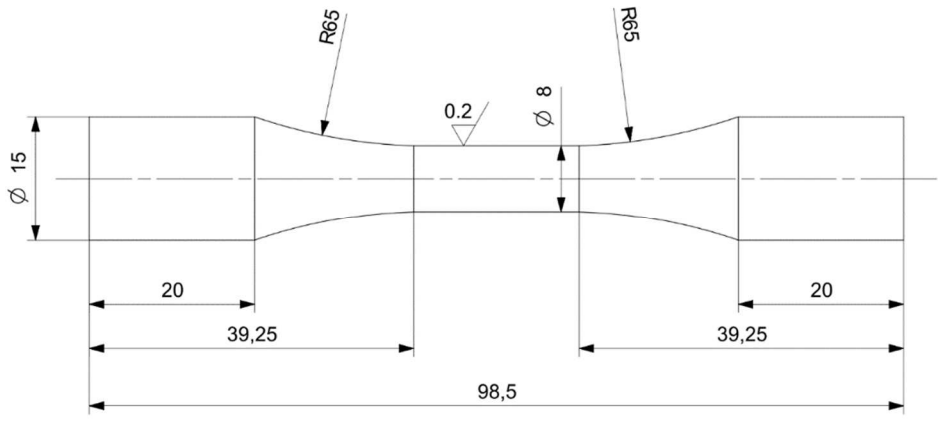

Figure 6.9 – Schematic illustration of the geometry of the fatigue specimen according to the ASTM E466-96 standard.

Due to availability, only a few tests have been carried out. This could be a big issue if the S/N curve was going to be obtained based on conventional fatigue models like the one of Basquin [114]. However, those models require a great number of tests to have an acceptable approximation to the reality and, even so, they exhibit a considerable dispersion as no probabilistic approaches are considered.

Nowadays there are some alternatives like the probabilistic fatigue model developed by Castillo and Fernandez-Canteli [115]. This model fulfils the physic principles, the weakest link principle and the statistic conditions related to the extreme values theory. This last consideration is in turn of particular relevance in fatigue phenomena as high dispersions are usually present. This makes possible the attaining of an acceptable S/N curve even if a few tests are carried out. Consequently, the ProFatigue software [116], which is based on this last model, will be utilised. In the following figures the results are shown (Figures 6.10-6.12). Note that "Pf" means the probability of fracture happening below the curve.

Looking at those results, it can be seen how both SSF and HF have almost the same fatigue resistance. They also exhibit the enhanced fatigue resistance of the SSF components subjected to the optimised treatment. These conclusions can be easily observed when comparing the 50% failure probability curve of the three cases (Figure 6.13).

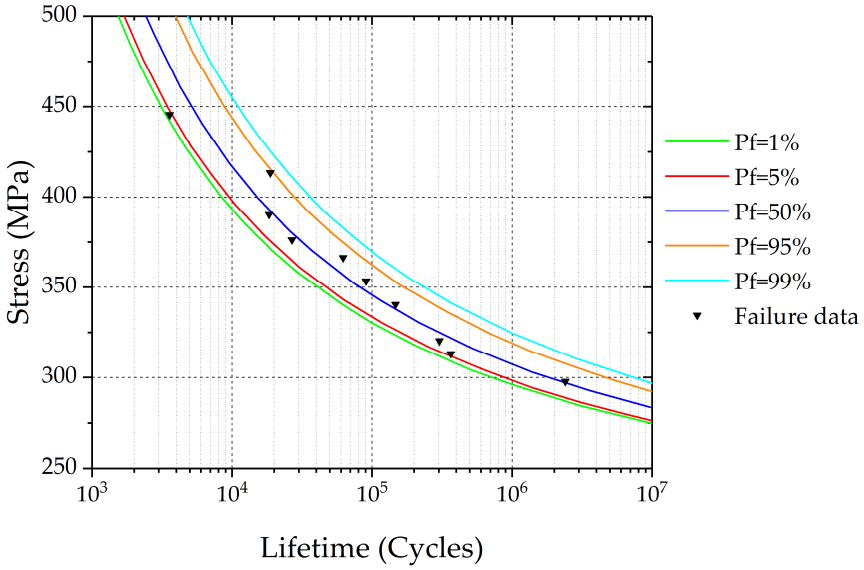

Figure 6.10 – Preliminary fatigue tests results for HF components.

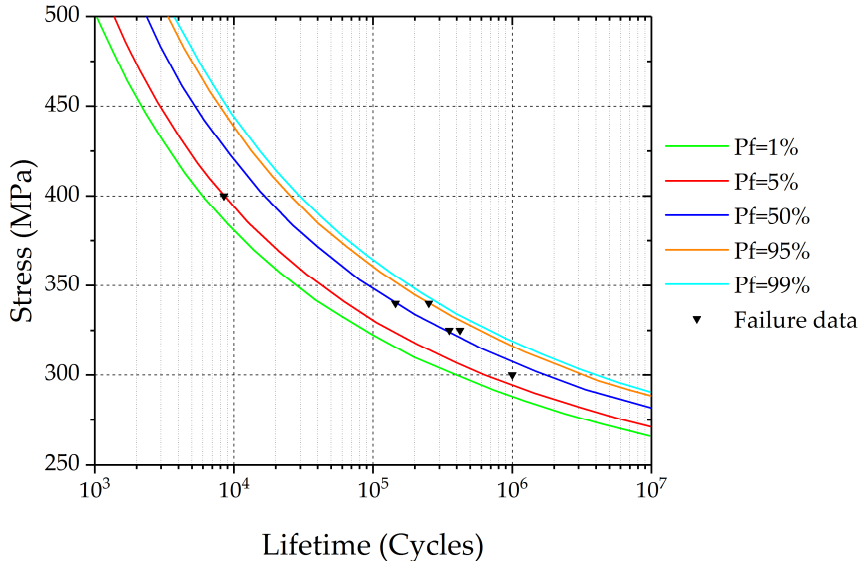

Figure 6.11 – Preliminary fatigue tests results for SSF components.

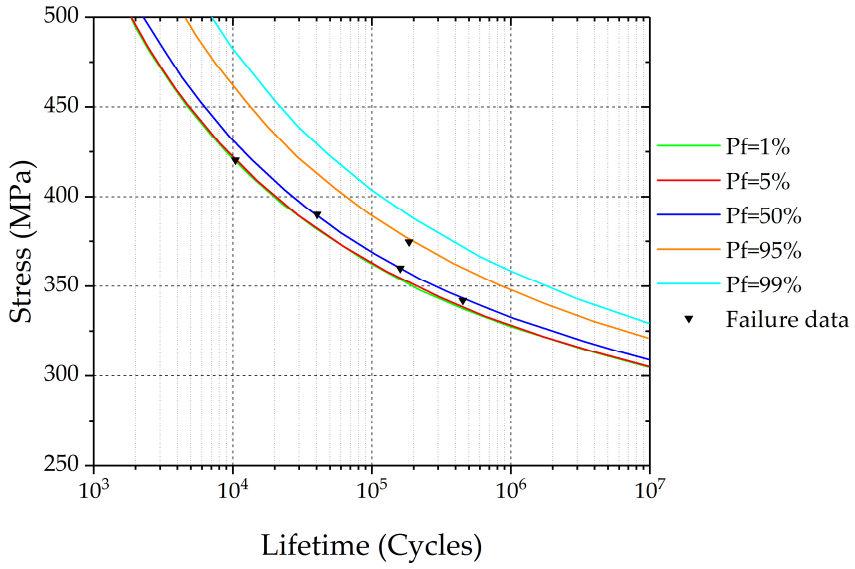

Figure 6.12 – Preliminary fatigue tests results for SSF components subjected to the optimised heat treatment.

In any case, it worth highlighting the preliminary nature of these tests. The shape of the curves can vary if more samples are tested. However, these initial results are intended to be a preliminary indicator of the fatigue behaviour of the material.

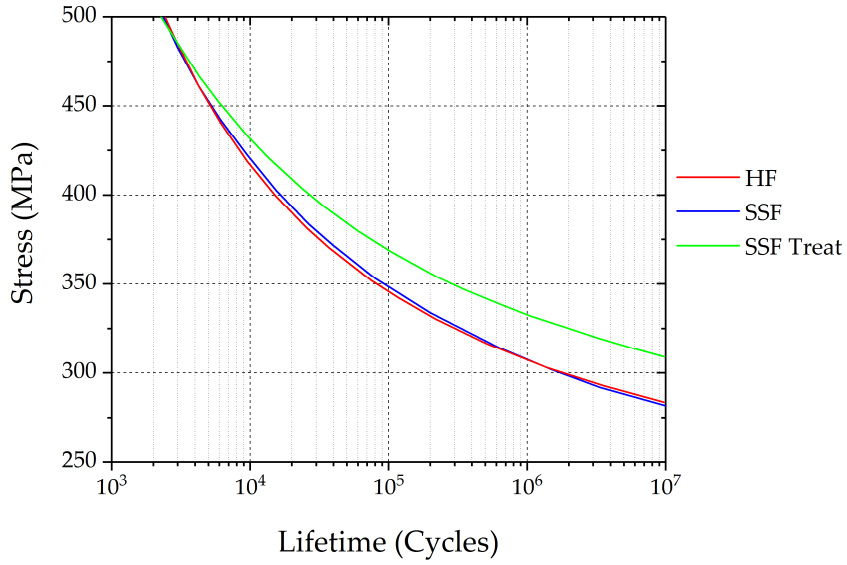

Figure 6.13 – Comparison of the Pf=50% curves of each case.

6.5. Economic aspects

The fabrication of those 250 components via SSF attaining great mechanical properties and showing that the moulds withstand such a high number of cycles without any problem opens the discussion about its economic feasibility. In the following lines, a brief analysis of the impact of this process on reducing the cost of the components is stated.

To begin with, the observed first and direct cost saving comes from removing the flash appearance. In this case, it has meant a save of around 300g of the raw material per component. This is around a 12% save in raw material which influences directly the final cost of the component as the price of the steel usually implies close to the 25-50% of the final cost. Therefore, this would mean a direct save of close to the 3-6% of the component's price.

In addition to this, the process has shown the capacity for filling smaller sections which means that the machining allowances can be successfully reduced. This would not only impact on the raw material (a saving of around 280g) but also on the subsequent machining process, saving almost another 3-6% of the final cost of the component.

Apart from this material reduction, there is the possibility of removing the postprocessing heat treatment using the 44MnSiV6 microalloyed steel. This alloy, as stated in Chapter 3, enables the obtaining of the required microstructure and properties if its cooling is controlled. Therefore, if the components are manufactured with this special steel under the right conditions, the price reduction would be even higher than saving 600g of raw material (around 10% of the final cost).

Going even further, this process has been successfully carried out recording forces below the 300t. This implies that presses of lower capacity and, therefore, cheaper, could be utilised. But if the direct relation is considered, the presses the forging industry are currently using to forge these components withstand between 2500-3000t. They are actually making the component in three steps plus a flash removal operation (Figure 6.14). In contrasts, this process only requires a unique deformation operation. Hence, if a proper tooling is developed, those presses would be capable of manufacturing at least 4-6 components in each cycle. If the installation is properly automated and assuming a continuous induction heating equipment, the actual production rates could be increased in around a 20-30%.

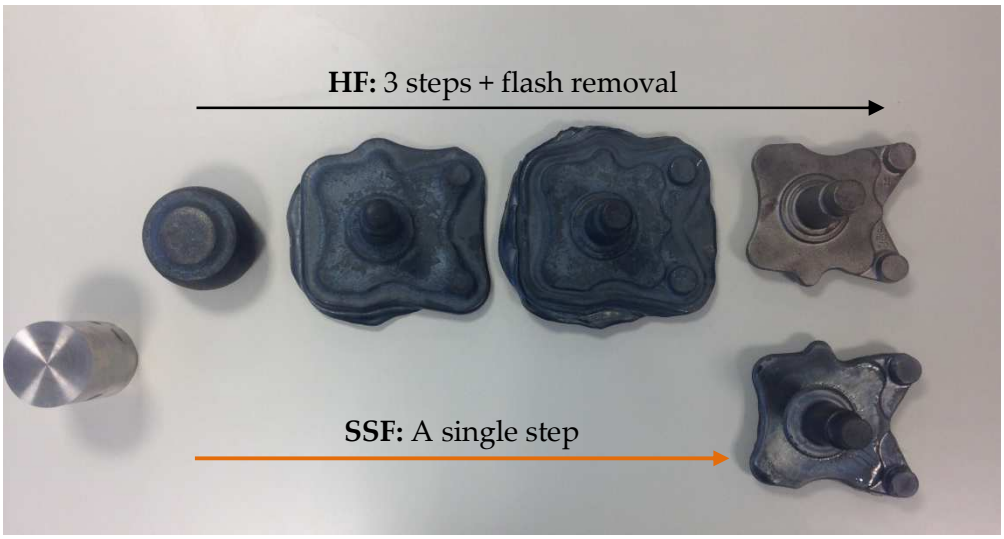

Figure 6.14 – Comparison between the conventional HF and SSF processes.

6.6. Concluding remarks

The fabrication of 250 components via the SSF is a turning point that exhibits the potential of this process. The obtained outcomes from the manufacturing of this batch are actually very interesting not only to show the capabilities of the process but also to realise and learn about its flowing capabilities and equipment requirements. In the following lines, the main conclusions of this chapter are stated.

SSF process

The manufacturing has been carried out in a laboratory environment and equipment. This implies that the required time to produce a component is not even similar to the industry. However, it is a matter of investing in industrial equipment (continuous induction equipment, cleaning and lubricating robot…).

Regarding the process itself, the clamping force has been observed to be critical to prevent the flash from generating. Moreover, a proper guiding of the dies must be ensured to secure a proper closing.

SSF components

250 sound components have been manufactured by taking advantage of the SSF using the S48C steel grade. The observed defects are related to the CeraSpray®

ceramic lubricant entrapment in the very surface of some edges. This could be easily solved by manufacturing some escape holes in the dies.

Dies degradation

First of all, note that the temperature controller of the dies is switched off between each working day. This means that the dies have been cooled to ambient and heated up to working temperatures several times during the batch manufacturing (30-40 components have been manufactured per day). This means that the material of the dies has been submitted to several thermal shocks that could lead to a loose of properties.

Even though, the dies have managed to withstand the manufacturing of the 250 components without any visible severe damage. The unique area where a discernible abrasion has been identified is related to the extrusion-type flow of the material that can be overcome with a simple component redesign that does not affect the spindle's functioning.

Mechanical properties

Tensile and fatigue tests have been carried out to specimens taken from the axle of the spindle according to the ASTM E8M-09 standard for tensile and ASTM E466-96 standard for fatigue experiments. The results show the great similarity in terms of yield and ultimate strengths between the HF and SSF components and the higher elongation capacity of the latter. The optimised treatment enhanced the yield and ultimate strengths of the SSF component while maintaining the elongation. Same conclusions are attained in the preliminary fatigue tests. HF and SSF components have the same fatigue behaviour whilst the SSF parts subjected to the optimised treatment exhibit a higher fatigue resistance.

Economic aspects

The fact of removing the flash appearance means a 300g material saving (12% of the initial raw material). If the forging allowances are as well reduced, an additional 280g saving is possible (11% of the initial raw material) at the same time that less machining will be needed. As assessed in Chapter 3, using a microalloyed steel implies the possibility of removing the postprocessing heat treatment, which could mean the saving of around the 10% of the final cost of the spindle. Moreover, considering the low forces required to manufacture a component, this process exhibits the possibility of increasing the productivity. This can be attained by manufacturing several components in each cycle because the actual presses in the HF industry are 6 to 10 times bigger than the 400t one used in this research.

Summary

This chapter has been devoted to the manufacturing of a batch of 250 spindles. The process set up has been defined and the attained results exhibited and explained. Moreover, the observed manufacturing influencing factors as well as the improvement opportunities or requirements for the industry are assessed.

All in all, the components are defect-free, with as forged mechanical properties and fabricated in a 400t press using less raw material than in the conventional HF in a 3000t press. In addition, the dies withstand the cycles as no discernible severe damage has been noticed. These results situate this process closer to be an industrial reality.

Chapter 7

RESEARCH CONCLUSIONS AND FUTURE WORK

"The more I learn, the more I realise how much I don't know"

Albert Einstein

Summary

This chapter gathers the principal outcomes of the present dissertation. It shows the readiness of the process to make an industrial production trial. Here, the influence of the analysed phenomena on the material softening is also mentioned, even if the main softening phenomena is still waiting for its discovery. Other aspects of the research like the importance of the utilised equipment and the most important results attained with each utilised steel grade are assessed. Lastly, future investigation proposals are stated.

7.1. Introduction

This PhD work has been focused on trying to give new insights into the SSF process. As stated in Chapter 1, two objectives have been the cornerstone of the present dissertation:

- **O1:** investigate and try to shed light on why the steel is behaving as it does during the SSF process enabling such great flow capabilities.
- **O2:** continue progressing on the components' manufacturing in order to bring the process closer to the industry.

To achieve those goals, the research procedure stated in Chapter 1 has been followed (Figure 7.1). After analysing the concepts stated in this flowchart, several are the remarkable conclusions that helped on the better understanding of the process. This chapter is therefore devoted to summarise the main outcomes of this research work and to propose future research goals.

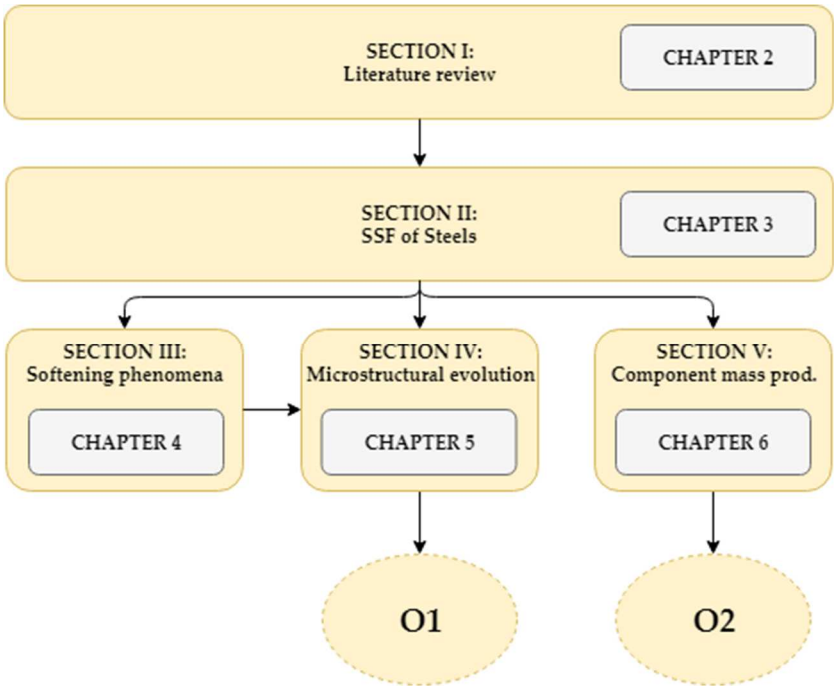

Figure 7.1 – Summarised structure of the present PhD dissertation.

7.2. Conclusions

The principal conclusions of this dissertation will be summarised according to each specific objective. Therefore, the main results regarding the material behaviour will be explained in the first place. Subsequently, the main outcomes regarding the component manufacturing via SSF will be stated.

7.2.1. Material behaviour during SSF

The analysed phenomena regarding the material softening are the incipient melting, the influence of sulphur and the adiabatic heating. While it is confirmed that the first two are not the explanation of the observed softening, the latter is still a candidate. Therefore, it can be said that the main driving phenomena responsible for the observed softening is still open.

In this aspect, a great state of the art equipment has been utilised to analyse the material. The analysis of the steel at the studied conditions is indeed a tough issue. However, great information has been attained which has definitely helped on further understanding the material deformation tendency, bringing closer the discovery of the driving phenomena behind the softening the material is exhibiting.

With this regard, this section will be divided into two. First, it is important to make clear where and why the utilised equipment has been helpful in analysing the material. Then, the obtained main outcomes regarding the main softening phenomena are explained.

7.2.1.1. Experimental equipment

It has to be noted the great combination of the DSC and the HT-CLSM. While the first one is really exact in defining the temperatures of the phase transitions, the latter contributes to defining the exact phase transitions there are happening. This has been really helpful on analysing the influence of the incipient melting.

With regard to the dynamic experiments to attain information about the material strength, the hot tensile and compression tests have been really helpful to detect the temperatures at which a severe grain decohesion happens. In addition, the flow curve information has also been attained from compression results.

The compression tests also enabled the confirmation of the effect of adiabatic heating in raising the temperature. However, as this compressive set up is not capable of reaching large strains, a Hat-Type shear sample has been designed and analysed. Even

if it has not been utilised yet, the performed theoretical calculations suggest its suitability to analyse the material behaviour at larger strains.

Lastly, the microstructure of the component manufactured with an austenitic alloy has been analysed by using different tools. The Micro-XRF equipment has been very important in observing not only the compositional distribution through the whole component but also in detecting the most interesting zones of the geometry. Then, a more focused analysis of those areas has been carried out by taking advantage of the optical and SEM microscopes and a micro-hardness tester. These latter techniques have been enabled the detection of Mo segregation and the influence of the strain in the component.

7.2.1.2. Softening phenomena

As mentioned before, three are the analysed phenomena: the incipient melting, the influence of sulphur and the effect of adiabatic heating. After analysing the incipient melting on the 42CrMo4E steel grade, it has not been observed any liquid below the solidus temperature. This suggests the inexistence of incipient melting and, therefore, it can be said that this is not the phenomenon responsible for the material flowing capabilities.

In any case, when using the alloy 28 stainless steel during SSF, the incipient melting has been used to enhance the material flowing capabilities. Consequently, this phenomenon is not the one that explains the material behaviour but it definitely can help on softening certain alloys.

Regarding the influence of sulphur, after analysing the 42CrMo4 steel grade at low, medium and high sulphur contents, no distinction has been detected. The three grades have been manufactured via SSF with no discernible load difference. Moreover, after analysing the microstructures of quenched samples, the sulphur remained in the MnS form. Those particles can act as crack generators or propagators. Nevertheless, their effect is not enough to generate the high softening it is happening during SSF.

The adiabatic heating analysis has demonstrated a temperature rise during compressing the material at the working temperatures. It has been therefore shown the capability of increasing the material temperature due to the deformation. However, the influence of the adiabatic heating at large strains has not been proved yet. Consequently, further investigations are needed to definitely confirm or deny it as the driving phenomena. Moreover, the heavily strained zones observed in the component analysed in Chapter 5 seem to be high enough to consider this phenomenon as a possible candidate.

7.2.2. Component's manufacturing via SSF

During this PhD work, different alloys have been successfully manufactured via SSF. Those have been utilised to confirm the wide processing window in terms of temperature, geometry and alloy variety. 250 components have been manufactured ensuring the repeatability, the as forged mechanical properties, the cost saving and a minimum die damage. In addition, a stainless steel that is actually very difficult to forge has been successfully deformed using the SSF process.

The utilised alloys for SSF during this dissertation are two medium carbon alloys (42CrMo4E and S48C), one microalloyed steel (44MnSiV6) and a stainless steel (Alloy 28). The main conclusions after using each alloy are stated in the following lines.

7.2.2.1. 42CrMo4E

This alloy was already utilised in MGEP to manufacture sound components in a unique step in a 400t press via SSF in comparison to the 4 steps in a 2500t press of the HF. Moreover, a 20% raw material saving and as forged mechanical properties were attained.

In this case, this alloy has been utilised to check the sensitivity of the process to the material temperature. Being 1408°C the solidus temperature and having manufactured the previous components at 1360°C, sound parts have been attained at temperatures close to 1300°C. Consequently, the temperature does not seem to be so sensitive as guessed initially, at least to this alloy. In addition, it could mean the possibility of lowering the manufacturing temperatures without compromising excessively the flowing capabilities. This could also have a great impact on the overall cost saving of the process.

7.2.2.2. S48C

With this alloy, it has been manufactured the H spindle for the first time using the SSF. It has exhibited the capacity of the SSF to properly fill more complex geometries. Moreover, a batch of 250 components using the H geometry has been manufactured. Apart from confirming the material saving (6-12% of the final cost of the component), the as forged tensile resistance, the repeatability and the minimum die damage, as forged fatigue strengths have been obtained.

7.2.2.3. 44MnSiV6

The microalloyed steels are designed to attain great mechanical properties after the manufacturing process avoiding the requirement of the postprocessing heat treatment.

To obtain such properties, some cooling conditions must be ensured to have a ferrite-pearlite structure through the material. This last structure is indeed the obtained one after submitting this material to SSF. Hence, this could mean an additional saving of around 10% of the final cost of the component.

7.2.2.4. Alloy 28

The alloy 28 is a quite difficult material to HF due to its high strength even at high temperatures. Therefore, very high temperatures are required to deform it. However, due to the compositional inhomogeneity, it starts to melt prematurely (incipient melting). While it means a problem for the HF, it is an advantage for the SSF. The generated incipient melting enhanced the fluidity of the material enabling a better cavity filling.

There, the defects generated due to this liquid solidification are detected only as deep as 0.5 mm from the surface. This means that a simple machining of 0.5 mm could be enough to have a sound component. The harmful compositional difference could be removed afterwards by submitting the component to a homogenisation heat treatment. Further analysis should be performed to confirm the mechanical properties.

7.2.3. Closure

All in all, this dissertation gives new insights regarding the SSF process both from the material and fabrication points of view. It is true that further research is still required to completely define what is happening in the material to explain and fully understand the observed behaviour. However, this investigation gathers great information to help in carrying that out.

This is one of the firsts attempts performed to analyse in depth the steels at these conditions. Therefore, at this point, any information that could lead to being closer to what is going on is helpful. In this aspect, this PhD work has shown the secondary role of the incipient melting and the sulphur influence. It has also exhibited the influence the strain has in the material, a fact that makes the adiabatic heating phenomenon a real possibility.

However, after analysing all the information of this dissertation, the material seems to be far from behaving thixotropically. Therefore, one can hardly see a great similarity between the conventional SSF and the process this PhD deals with. Hence, and still maintaining its relationship with the SSP, I propose to call to this process as “Near Solidus Forging” (NSF) as it resembles more closely the manufacturing conditions.

With regard to the components manufacturing, I want to enhance the attained outcomes that definitely brings this process closer to the industry. The process shows the ability to withstand the manufacturing of 250 components with a minimum die damage, a fact that resolves one of the main issues when facing this process. It has also shown the repeatability as all the studied components exhibit as forged mechanical properties. Moreover, as forged fatigue resistance has been assessed for the first time using this process. All those conclusions have been attained while reducing the raw material use (around 580g), maintaining the unique forging step in a 400t (4 steps in a 3500t in HF) and being capable of removing the heat treatment if a microalloyed is utilised (around a 10% saving on the final cost). Therefore, it can be said that these spindles can be manufactured cheaper and more efficiently than in HF with the same mechanical properties.

7.3. Future Work

This dissertation has shown that the previously called Semi-Solid Forging (SSF) but now proposed Near Solidus Forging (NSF) process is ready to take the leap to the industry. Nevertheless, even if closer, the material behaviour is still not properly understood. Consequently, a lot of work is still required to properly control and define the phenomena that are happening during the process.

To begin with, it is necessary to gain the knowledge about the material behaviour during NSF. To do so, further analysis on the influence of the adiabatic heating should be performed. Continuing this analysis with the shear sample could be an option. Moreover, the observation of the influence of the strain degree in the material also seems to be important to observe if there is any relation between this and the material behaviour.

With regard to the process itself, it is still unknown the filling limits of the process. Which are the maximum lengths or minimum thicknesses the NSF could fill are still unknown. Hence, more complex shapes should be tried in an attempt to define the filling capabilities. Similarly, this dissertation has assessed the manufacturing of an Alloy 28 stainless steel, that is very close to the Ni-based alloys family. Therefore, other high melting point alloys like Inconel or Titanium should be as well tried.

As mentioned before, this process is now ready to take the leap to the industry. Therefore, a real industrial trial should be performed to ensure the validity of the process while the components are submitted to a full quality control under industrial parameters. This will permit to certify the real potential of the NSF process.

Lastly, I wanted to enhance the importance of discovering what is happening to the material during the NSF process. This knowledge is essential to accurately design the

process in order to set up the best working conditions. Moreover, this information is crucial to properly redesign the components according to the material behaviour. This will enable to take the highest benefit from the NSF process.

List of Figures

List of Tables

References

[1] H.J. Büchner, J. Gloßner, Foundry Industry 2020: Trends and Challenges, IKB Dtsch. Ind. AG. (2015). http://www.globalcastingmagazine.com/wp-content/uploads/2015/05/Foundry_Industry_2020.pdf.

[2] Worldsteel, Steel in Automotive, (2018). https://www.worldsteel.org/steel-by-topic/steel-markets/automotive.html (accessed August 29, 2018).

[3] H.J. Büchner, Foundry Industry 2025 – Tomorrow ' s Challenges due to Changing Market Conditions, Beijing, 2018. https://www.foundry-planet.com/fileadmin/redakteur/pdf-dateien/China_Foundry_Association.pdf.

[4] FIERF, Forging Industry Technology Roadmap 2016 Revision, Cleveland, 2016. https://www.forging.org/uploaded/content/media/2016 Forging Roadmap Update (1).pdf.

[5] CAEF, World Foundry Industry 2016, (2016). https://www.caef.eu/en/statistics/ (accessed August 29, 2018).

[6] Euroforge, Euroforge: Total Production of Forgings in 2016, 2016.

[7] Z. Azpilgain, J. Gómez, I. Hurtado, I. Lete, R. Romera, R. Estevan, S. Sainz, P. Egizabal, J. Goñi, Fabricación y cornformado semisólido de aleaciones ligéras, IMHE Inf. Máquinas-Herramienta, Equipos y Accesorios. 293 (2003) 128–135.

[8] Z. Azpilgain, L. Hurtado, R. Romera, L.L.A. Armendáriz, Factores termodinámicos y microestructurales para el diseño de aleaciones tixotrópicas, Rev. Metal. (2005) 170–175. http://revistademetalurgia.revistas.csic.es/index.php/revistademetalurgia/article/view/1019/1032.

[9] Z. Azpilgain, I. Hurtado, R. Ortubay, J. Bilbao, I. Landa, J. Atxa, Propiedades mecánicas de aleaciones de aluminio conformadas en estado semisólido, Perspect. La Investig. Sobre Mater. En España En El Siglo XXI. 1 (2006) 79–82.

[10] Z. Azpilgain, I. Hurtado, R. Ortubay, I. Landa, J. Atxa, Semisolid Forging of 7000 Series Aluminum Alloys, Solid State Phenom. 116–117 (2006) 758–761. doi:10.4028/www.scientific.net/SSP.116-117.758.

[11] A. Blanco, Z. Azpilgain, J. Lozares, P. Kapranos, I. Hurtado, Rheological characterization of A201 aluminum alloy, Trans. Nonferrous Met. Soc. China (English Ed. 20 (2010) 1638–1642. doi:10.1016/S1003-6326(09)60351-4.

[12] E. Echaniz, Development of Hybrid Structures by Semi-Solid Forming of Aluminum of Steel, Mondragon Unibertsitatea, 2016.

[13] J. Lozares, Semisolid forging of steel components for automotive industry, Mondragon Unbertsitatea, 2014.

[14] D.B. Spencer, R. Mehrabian, M.C. Flemings, Rheological behavior of Sn-15 pct Pb in the crystallization range, Metall. Trans. 3 (1972) 1925–1932. doi:10.1007/BF02642580.

[15] D.H. Kirkwood, Semi-solid Metal Processing, Int. Mater. Rev. 39 (1994) 173–189.

[16] K.P. Young, R.G. Riek, M.C. Flemings, Structure and properties of Thixocast steels, Met. Technol. 6 (1979) 130–137. doi:http://dx.doi.org/10.1179/030716979803276552.

[17] P. Kapranos, Semi-Solid Metal Processing— Thixoforming, Explorer (Hayward). (2001) 1–6.

[18] M. Blad, B. Johannesson, P. Nordberg, J. Winklhofer, Manufacturing and Fatigue Verification of Two Different Components Made by Semi-Solid Processing of Aluminium TX630 Alloy, in: A. Rassili (Ed.), Semi-Solid Process. Alloy. Compos. XIV, TRANS TECH PUBLICATIONS, Salt Lake City, 2016: pp. 328–333.

[19] P. Kapranos, D.H. Kirkwood, C.M. Sellars, Semi-solid processing of tool steel, J. Phys. 4 (1993) 835–840. doi:10.1051/jp4:19937131.

[20] G. Hirt, W. Bleck, A. Bührig-Polaczek, H. Shimahara, W. Püttgen, C. Afrath, Semi Solid Casting and Forging of Steel, Solid State Phenom. 116–117 (2006) 34–43. doi:10.4028/www.scientific.net/SSP.116-117.34.

[21] P. Cezard, T. Sourmail, Thixoforming of Steel: A State of the Art from an Industrial Point of View, Solid State Phenom. 141–143 (2008) 25–35. doi:10.4028/www.scientific.net/SSP.141-143.25.

[22] C.J. Quaak, Rheology of partially solidified aluminium alloys and composites, Technische Universiteit Delft, 1996.

[23] M.C. Flemings, Behavior of Metal Alloys in the Semisolid State, Metall. Mater. Trans. (1991) 957–981.

[24] M.N. Mohammed, M.Z. Omar, M.S. Salleh, K.S. Alhawari, P. Kapranos, Semisolid metal processing techniques for nondendritic feedstock production, Sci. World J. 2013 (2013). doi:10.1155/2013/752175.

[25] A. de Figueredo, D. Apelian, Science and technology of semi-solid metal processing, North American Die Casting Assoc., 2001.

[26] G. Hirt, R. Kopp, Thixoforming, Semi - solid Metal Processing, WILEY-VCH Verlag GmbH & Co. KGaA, 2009.

[27] W. Bleck, G. Hirt, W. Püttgen, H. Shimahara, Thixoforming of Steels - A Status Report, Mater. Sci. Forum. 539–543 (2007) 4297–4302. doi:10.4028/www.scientific.net/MSF.539-543.4297.

[28] E. Becker, V. Favier, R. Bigot, P. Cezard, L. Langlois, Impact of experimental conditions on material response during forming of steel in semi-solid state, J. Mater. Process. Technol. 210 (2010) 1482–1492. doi:10.1016/j.jmatprotec.2010.04.006.

[29] C. Fraipont, W. Püttgen, W. Bleck, J. Lecomte-Beckers, Influence of Experimental Parameters on Properties and Microstructure of the Steel X210CrW12 in the Semi-Solid State, Solid State Phenom. 116–117 (2006) 209–212. doi:10.4028/www.scientific.net/SSP.116-117.209.

[30] M. Kiuchi, R. Kopp, Mushy/Semi-Solid Metal Forming Technology – Present and Future, CIRP Ann. - Manuf. Technol. 51 (2002) 653–670. doi:10.1016/S0007-8506(07)61705-3.

[31] H.V. Atkinson, Modelling the semisolid processing of metallic alloys, Prog. Mater. Sci. 50 (2005) 341–412. doi:10.1016/j.pmatsci.2004.04.003.

[32] C.M. Gourlay, a K. Dahle, Dilatant shear bands in solidifying metals., Nature. 445 (2007) 70–73. doi:10.1038/nature05426.

[33] O. Reynolds, On the dilatancy of media composed of rigid particles, Philos. Mag. J. Sci. 20 (1885) 469–482. doi:10.1080/14786448508627791.

[34] C.M. Gourlay, T. Nagira, K. Uesugi, H. Yasuda, In Situ Study of the Altering Globule Packing-Density during Semisolid Alloy Deformation, Solid State Phenom. 192–193 (2012) 185–190. doi:10.4028/www.scientific.net/SSP.192-193.185.

[35] T. Nagira, C.M. Gourlay, A. Sugiyama, M. Uesugi, Y. Kanzawa, M. Yoshiya, K. Uesugi, K. Umetani, H. Yasuda, Direct observation of deformation in semi-solid carbon steel, Scr. Mater. 64 (2011) 1129–1132. doi:10.1016/j.scriptamat.2011.03.009.

[36] B. Cai, S. Karagadde, L. Yuan, T.J. Marrow, T. Connolley, P.D. Lee, In situ synchrotron tomographic quantification of granular and intragranular deformation during semi-solid compression of an equiaxed dendritic Al-Cu alloy, Acta Mater. 76 (2014) 371–380. doi:10.1016/j.actamat.2014.05.035.

[37] K.M. Kareh, P.D. Lee, R.C. Atwood, T. Connolley, C.M. Gourlay, Revealing the micromechanisms behind semi-solid metal deformation with time-resolved X-ray tomography, Nat Commun. 5 (2014) 4464. doi:10.1038/ncomms5464.

[38] T. Nagira, S. Morita, H. Yokota, H. Yasuda, C.M. Gourlay, M. Yoshiya, A. Sugiyama, K. Uesugi, A. Takeuchi, Y. Suzuki, In Situ Observation of

Deformation in Semi-solid Fe-C Alloys at High Shear Rate, Metall. Mater. Trans. A Phys. Metall. Mater. Sci. 45 (2014) 5613–5623. doi:10.1007/s11661-014-2489-5.

[39] B. Cai, S. Karagadde, D. Rowley, T.J. Marrow, T. Connolley, P.D. Lee, Time-resolved synchrotron tomographic quantification of deformation-induced flow in a semi-solid equiaxed dendritic Al-Cu alloy, Scr. Mater. 103 (2015) 69–72. doi:10.1016/j.scriptamat.2015.03.011.

[40] K.M. Kareh, P.D. Lee, C.M. Gourlay, Globule-Globule Interactions during Deformation in Semi-Solid Al-Cu Using Time-Resolved X-Ray Tomography, Solid State Phenom. 192 (2013) 179–184. doi:10.4028/www.scientific.net/SSP.192-193.179.

[41] K.M. Kareh, P.D. Lee, R.C. Atwood, T. Connolley, C.M. Gourlay, Pore behaviour during semi-solid alloy compression: Insights into defect creation under pressure, Scr. Mater. 89 (2014) 73–76. doi:10.1016/j.scriptamat.2014.06.033.

[42] L. Yuan, P.D. Lee, A new mechanism for freckle initiation based on microstructural level simulation, Acta Mater. 60 (2012) 4917–4926. doi:10.1016/j.actamat.2012.04.043.

[43] S. Karagadde, L. Yuan, N. Shevchenko, S. Eckert, P.D. Lee, 3-D microstructural model of freckle formation validated using in situ experiments, Acta Mater. 79 (2014) 168–180. doi:10.1016/j.actamat.2014.07.002.

[44] S. Karagadde, P.D. Lee, B. Cai, J.L. Fife, M.A. Azeem, K.M. Kareh, C. Puncreobutr, D. Tsivoulas, T. Connolley, R.C. Atwood, Transgranular liquation cracking of grains in the semi-solid state., Nat. Commun. 6 (2015) 8300. doi:10.1038/ncomms9300.

[45] D.H. Kirkwood, Semi-solid processing of high melting point alloys, in: Proceeding 4th Internatioanl Conf. Semi-Solid Process. Alloy. Compos., 1996: pp. 320–325.

[46] J. Lozares, Z. Azpilgain, I. Hurtado, I. Loizaga, Analysis of a Thixo-Lateral Forged Spindle from LTT C45, LTT C38 and LTT 100Cr6 Steel Grades, Solid State Phenom. 217–218 (2014) 347–354. doi:10.4028/www.scientific.net/SSP.217-218.347.

[47] J. Lozares, G. Plata, Z. Azpilgain, G. Álvarez, Semisolid forming of 42CrMo4E steel grade, in: 19th ESAFORM Conf., Nantes, 2016. doi:10.1063/1.4963422.

[48] G. Plata, J. Lozares, Z. Azpilgain, I. Hurtado, I. Loizaga, Z. Idoyaga, Semisolid forming of S48C steel grade, in: 20th ESAFORM Conf., Dublin, Ireland, 2017. doi:10.1063/1.5008154.

[49] R. Bigot, E. Becker, L. Langlois, Some Approaches on Industrial Installation of Steel Thixoforged Processes, Solid State Phenom. 192–193 (2012) 521–526. doi:10.4028/www.scientific.net/SSP.192-193.521.

[50] E. Becker, R. Bigot, F. Baratto, J. Croué, O. Gyss, Experimental Investigation Of Thixoforging Tubes, in: 20th ESAFORM Conf., Dublin, Ireland, 2017. doi:10.1063/1.5008151.

[51] Z. Gronostajski, M. Hawryluk, The main aspects of precision forging, Arch. Civ. Mech. Eng. 8 (2008) 39–55. doi:10.1016/S1644-9665(12)60192-7.

[52] Z. Azpilgain, R. Ortubay, A. Blanco, I. Hurtado, Servomechanical Press: A New Press Concept for Semisolid Forging, Solid State Phenom. 141–143 (2008) 261–266. doi:10.4028/www.scientific.net/SSP.141-143.261.

[53] J.C. Pierret, A. Rassili, G. Vaneetveld, R. Bigot, J. Lecomte-Beckers, Friction coefficients evaluation for steel thixoforging, Int. J. Mater. Form. 3 (2010) 763–766. doi:10.1007/s12289-010-0882-1.

[54] E.G. Nisbett, Steel Forgings: Design, Production, Selection, Testing and Application, ASTM International, 2005. doi:10.1520/MNL53-EB.

[55] W.T. Lankford, Some considerations of strength and ductility in the continuous-casting process, Metall. Trans. 3 (1972) 1331–1357. doi:10.1007/BF02643017.

[56] F. Weinberg, The ductility of continuously-cast steel near the melting point-hot tearing, Metall. Trans. B. 10 (1979) 219–227. doi:10.1007/BF02652466.

[57] G.E. Hale, J. Nutting, Overheating and burning of steel, Int. Met. Rev. 29 (1984) 273–298.

[58] S. Pogatscher, D. Leutenegger, J.E.K. Schawe, P.J. Uggowitzer, J.F. Löffler, Solid-solid phase transitions via melting in metals, Nat. Commun. 7 (2016) 11113. doi:10.1038/ncomms11113.

[59] J.W. Cahn, Y. Mishin, A. Suzuki, Coupling grain boundary motion to shear deformation, Acta Mater. 54 (2006) 4953–4975. doi:10.1016/j.actamat.2006.08.004.

[60] A. Adland, A. Karma, R. Spatschek, D. Buta, M. Asta, Phase-field-crystal study of grain boundary premelting and shearing in bcc iron, Phys. Rev. B - Condens. Matter Mater. Phys. 87 (2013). doi:10.1103/PhysRevB.87.024110.

[61] Z. Jonsta, A. Hernas, K. Mazanec, Contribution to mechanical metallurgy behaviour of steel during continuous casting, J. Mater. Process. Technol. 78 (1998) 90–94. doi:10.1016/S0924-0136(97)00468-8.

[62] T. Watanabe, I. Okane, A Study on the Formation of Partially Melted

Regions in Weld Heat-Affected Zone of High Strength Steel, Trans. Japan Melting Soc. 13 (1982) 19–29.

[63] J.P. Bailon, F. Weinberg, Segregation at Melted Grain Boundaries in Steel, Can. Metall. Q. 19 (1980) 251–257. doi:10.1179/cmq.1980.19.2.251.

[64] V. V. Zabil'skii, R.M. Nikonova, Ductile-brittle transition in steels at near-solidus temperatures, Met. Sci. Heat Treat. 48 (2006) 150–161. doi:10.1007/s11041-006-0061-7.

[65] F. Hassani, T.M. Maccagno, J.J. Jonas, S. Yue, Behavior of steels near the incipient melting temperature, Metall. Mater. Trans. A. 25 (1994) 125–133. doi:10.1007/BF02646681.

[66] M. Hojny, M. Glowacki, The methodology of Strain-Stress Curves Determination for Steel in Semi-Solid State, Arch. Metall. Mater. 54 (2009) 475–483.

[67] E. Tzimas, A. Zavaliangos, Evaluation of volume fraction of solid in alloys formed by semisolid processing, J. Mater. Sci. 5 (2000) 5319–5329.

[68] J. Lecomte-Beckers, A. Rassili, M. Carton, M. Robelet, R. Koeune, Study of the Liquid Fraction and Thermophysical Properties of Semi-Solid Steels and Application to the Simulation of Inductive Heating for Thixoforming, in: Adv. Methods Mater. Form., Springer-Verlag, Cluj-Napoca (Romania), 2007: pp. 321–347. doi:10.1007/3-540-69845-0_20.

[69] A. Rassili, M. Robelet, J. Lecomte-Beckers, Identification of Suitable Steels, in: H.V. Atkinson, A. Rassili (Eds.), Thixoforming Steel, Shaker Verlag, 2010: pp. 37–65.

[70] C.J. Adams, Hot ductility and strength of strand cast steels up to their melting points, in: Proc. Open Hear. Conf., Pittsburgh, 1971.

[71] E. Tzimas, a. Zavaliangos, Mechanical behavior of alloys with equiaxed microstructure in the semisolid state at high solid content, Acta Mater. 47 (1999) 517–528. doi:10.1016/S1359-6454(98)00356-5.

[72] P. Kapranos, T.Y. Liu, H.V. Atkinson, D.H. Kirkwood, Investigation into the rapid compression of semi-solid alloy slugs, J. Mater. Process. Technol. 111 (2001) 31–36. doi:10.1016/S0924-0136(01)00534-9.

[73] H. Shimahara, R. Baadjou, R. Kopp, G. Hirt, Investigation of Flow Behaviour and Microstructure on X210CrW12 Steel in Semi-Solid State, Solid State Phenom. 116–117 (2006) 189–192. doi:10.4028/www.scientific.net/SSP.116-117.189.

[74] H. Chikama, H. Shibata, T. Emi, M. Suzuki, In-situ real time observation of planar to cellular and cellular to dendritic transition of crystals growing in

Fe-C alloy metls.pdf, Mater. Trans. 37 (1996) 620–626. doi:10.2320/matertrans1989.37.620.

[75] S. Niknafs, D. Phelan, R. Dippenaar, High-temperature laser-scanning confocal microscopy as a tool to study the interface instability during unsteady-state solidification of low-carbon steel, J. Microsc. 249 (2013) 53–61. doi:10.1111/j.1365-2818.2012.03679.x.

[76] D. Zhang, H. Terasaki, Y.I. Komizo, In situ observation of the formation of intragranular acicular ferrite at non-metallic inclusions in C-Mn steel, Acta Mater. 58 (2010) 1369–1378. doi:10.1016/j.actamat.2009.10.043.

[77] H. Terasaki, Y. Komizo, Time-resolved in-situ analysis of phase evolution for the directional solidification of carbon steel weld metal, Metall. Mater. …. 37 (2006) 1261–1266. doi:10.1007/s11661-006-1077-8.

[78] C. Slater, K. Hechu, S. Sridhar, Characterisation of solidification using combined confocal scanning laser microscopy with infrared thermography, Mater. Charact. 126 (2017) 144–148. doi:10.1016/j.matchar.2017.02.025.

[79] G. Gu, R. Pesci, L. Langlois, E. Becker, R. Bigot, M.X. Guo, Microstructure observation and quantification of the liquid fraction of M2 steel grade in the semi-solid state, combining confocal laser scanning microscopy and X-ray microtomography, Acta Mater. 66 (2014) 118–131. doi:10.1016/j.actamat.2013.11.075.

[80] G.C. Gu, R. Pesci, E. Becker, L. Langlois, R. Bigot, In situ Microstructure Observation Of Steel Grades In The Semi-Solid State For Thixoforging Process By Using Confocal Laser Scanning Microscopy, Solid State Phenom. 217–218 (2014) 15–22. doi:10.4028/www.scientific.net/SSP.217-218.15.

[81] K. Hechu, C. Slater, B. Santillana, S. Clark, S. Sridhar, A novel approach for interpreting the solidification behaviour of peritectic steels by combining CSLM and DSC, Mater. Charact. 133 (2017) 25–32. doi:10.1016/j.matchar.2017.09.013.

[82] WMG, Steel Processing Group Facilities and Equipment, (2018).

[83] K. Yasumoto, Y. Maehara, S. Ura, Effects of sulphur on hot ductility of low-carbon steel austenite, Mater. Sci. Technol. 1 (1985) 111–116.

[84] C.A. Hippsley, Sulphur segregation and high-temperature brittle intergranular fracture in alloy steels, Acta Metall. 35 (1987) 2399–2416. doi:10.1016/0001-6160(87)90138-6.

[85] J.R. Rice, J.S. Wang, Embrittlement of interfaces by solute segregation, Mater. Sci. Eng. A. 107 (1989) 23–40. doi:10.1016/0921-5093(89)90372-9.

[86] M. Robelet, Acier pur construction mécaniqui, procédé de mise en forme à chaud d´une pièce de cet acier, et pièce ainsi obtenue, EP 1 426 460 A1, 2004.

[87] C. Hee Yu, M. Suzuki, H. Shibata, T. Emi, Anomaly in Melting Behaviour and Mechanical Properties of Carbon Steels Near Their Solidus Temperature, Mater. Trans. 37 (1996) 1251–1257.

[88] H.G. Suzuki, S. Nishimura, S. Yamaguchi, Characteristics of Hot Ductility in Steels Subjected to the Melting and Solidification, Trans. Iron Steel Inst. Japan. 22 (1982) 48–56. doi:10.2355/isijinternational1966.22.48.

[89] S. Mahajan, D.F. Williams, Deformation Twinning in Metals and Alloys, Int. Metall. Rev. 18 (1973) 43–61. doi:10.1179/imtlr.1973.18.2.43.

[90] L. Chen, H.-S. Kim, S.-K. Kim, B.C. De Cooman, Localized Deformation due to Portevin–LeChatelier Effect in 18Mn–0.6C TWIP Austenitic Steel, ISIJ Int. 47 (2007) 1804–1812. doi:10.2355/isijinternational.47.1804.

[91] W.W. Jian, G.M. Cheng, W.Z. Xu, H. Yuan, M.H. Tsai, Q.D. Wang, C.C. Koch, Y.T. Zhu, S.N. Mathaudhu, Ultrastrong Mg alloy via nano-spaced stacking faults, Mater. Res. Lett. 1 (2013) 61–66. doi:10.1080/21663831.2013.765927.

[92] A. Eisenlohr, I. Gutierrez-Urrutia, D. Raabe, Adiabatic temperature increase associated with deformation twinning and dislocation plasticity, Acta Mater. 60 (2012) 3994–4004. doi:10.1016/j.actamat.2012.03.008.

[93] A. Hor, F. Morel, J. Lou Lebrun, G. Germain, An experimental investigation of the behaviour of steels over large temperature and strain rate ranges, Int. J. Mech. Sci. 67 (2013) 108–122. doi:10.1016/j.ijmecsci.2013.01.003.

[94] A. Andrade-Campos, F. Teixeira-Dias, U. Krupp, F. Barlat, E.F. Rauch, J.J. Grácio, Effect of strain rate, adiabatic heating and phase transformation phenomena on the mechanical behaviour of stainless steel, Strain. 46 (2010) 283–297. doi:10.1111/j.1475-1305.2008.00572.x.

[95] M. Naderi, L. Durrenberger, A. Molinari, W. Bleck, Constitutive relationships for 22MnB5 boron steel deformed isothermally at high temperatures, Mater. Sci. Eng. A. 478 (2008) 130–139. doi:10.1016/j.msea.2007.05.094.

[96] G.I. Taylor, H. Quinney, The Latent Energy Remaining in a Metal after Cold Working, Proc. R. Soc. A Math. Phys. Eng. Sci. 143 (1934) 307–326. doi:10.1098/rspa.1934.0004.

[97] J.J. Mason, A.J. Rosakis, G. Ravichandran, On the strain and strain rate dependence of the fraction of plastic work converted to heat: an

experimental study using high speed infrared detectors and the Kolsky bar, Mech. Mater. 17 (1994) 135–145. doi:10.1016/0167-6636(94)90054-X.

[98] A.T. Zehnder, A model for the heating due to plastic work, Mech. Res. Commun. 18 (1991) 23–28. doi:10.1016/0093-6413(91)90023-P.

[99] P. Rosakis, A.J. Rosakis, G. Ravichandran, J. Hodowany, Thermodynamic internal variable model for the partition of plastic work into heat and stored energy in metals, J. Mech. Phys. Solids. 48 (2000) 581–607. doi:10.1016/S0022-5096(99)00048-4.

[100] P. Knysh, Y.P. Korkolis, Determination of the fraction of plastic work converted into heat in metals, Mech. Mater. 86 (2015) 71–80. doi:10.1016/j.mechmat.2015.03.006.

[101] C. Mayr, G. Eggeler, G.A. Webster, G. Peter, Double shear creep testing of superalloy single crystals at temperatures above 1000 °C, Mater. Sci. Eng. A. 199 (1995) 121–130. doi:10.1016/0921-5093(94)09721-6.

[102] Y. Beygelzimer, R. Valiev, V. Varyukhin, Simple Shear: Double-Stage Deformation, Mater. Sci. Forum. 667–669 (2010) 97–102. doi:10.4028/www.scientific.net/MSF.667-669.97.

[103] G.T. Gray, K.S. Vecchio, V. Livescu, Compact forced simple-shear sample for studying shear localization in materials, Acta Mater. 103 (2016) 12–22. doi:10.1016/j.actamat.2015.09.051.

[104] A. Dorogoy, D. Rittel, A. Godinger, Modification of the Shear-Compression Specimen for Large Strain Testing, Exp. Mech. 55 (2015) 1627–1639. doi:10.1007/s11340-015-0057-6.

[105] K.H. Hartmann, H.D. Kunze, L.W. Meyer, Metallurgical effects on impact loaded materials, in: Shock Waves High-Strain-Rate Phenom. Met., Plenum Press, 1981: pp. 325–337. doi:10.1007/978-1-4613-3219-0_21.

[106] M.A. Meyers, Y.B. Xu, Q. Xue, M.T. Pérez-Prado, T.R. McNelley, Microstructural evolution in adiabatic shear localization in stainless steel, Acta Mater. 51 (2003) 1307–1325. doi:10.1016/S1359-6454(02)00526-8.

[107] Q. Xue, G.T. Gray, III, Development of adiabatic shear bands in annealed 316L stainless steel: part 1. correlation between evolving microstructure and mechanical behavior, Metall. Mater. Trans. A. 37 (2006) 2435–2446. doi:10.1007/BF02586217.

[108] H.P. Stüwe, Equivalent strains in severe plastic deformation, Adv. Eng. Mater. 5 (2003) 291–295. doi:10.1002/adem.200310085.

[109] N. Pardis, R. Ebrahimi, H.S. Kim, Equivalent strain at large shear deformation: Theoretical, numerical and finite element analysis, J. Appl.

Res. Technol. 15 (2017) 442–448. doi:10.1016/j.jart.2017.05.002.

[110] Yonekura, SVF15FTC - High temperature tension & compression observation test equipment, (2018).

[111] J. Fonseca, C. O'Sullivan, T. Nagira, H. Yasuda, C.M. Gourlay, In situ study of granular micromechanics in semi-solid carbon steels, Acta Mater. 61 (2013) 4169–4179. doi:10.1016/j.actamat.2013.03.043.

[112] C.M. Gourlay, C. O'Sullivan, J. Fonseca, L. Yuan, K.M. Kareh, T. Nagira, H. Yasuda, Synchrotron radiography studies of shear-induced dilation in semisolid Al alloys and steels, Jom. 66 (2014) 1415–1424. doi:10.1007/s11837-014-1029-5.

[113] P. Honnerov, J. Martan, 840-M Temperature Study Results, 2015.

[114] O. Basquin, The exponential law of endurance tests., Proc Am Soc Test Mater. 10 (1910) 625–630.

[115] E. Castillo, A. Fernandez-Canteli, A Unified Statistical Methodology for Modelling Fatigue Damage, Springer Netherlands, 2009. doi:10.1007/978-1-4020-9182-7.

[116] A. Fernández-Canteli, C. Przybilla, M. Nogal, M.L. Aenlle, E. Castillo, Profatigue: A software program for probabilistic assessment of experimental fatigue data sets, Procedia Eng. 74 (2014) 236–241. doi:10.1016/j.proeng.2014.06.255.